Numerical simulations of static liquefaction in submerged slopes

Miguel Angel Chavez Abril

Delft University of Technology

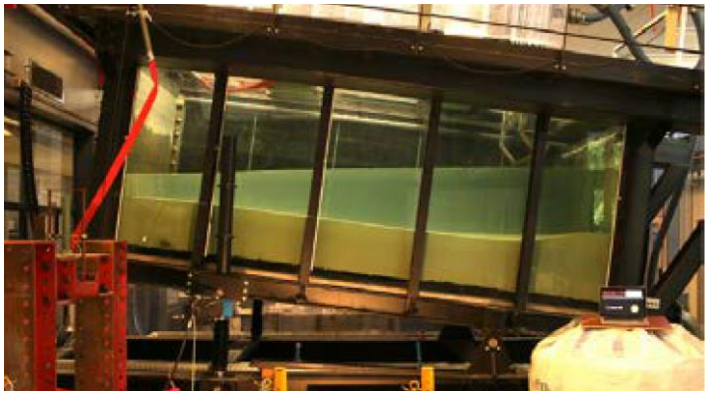

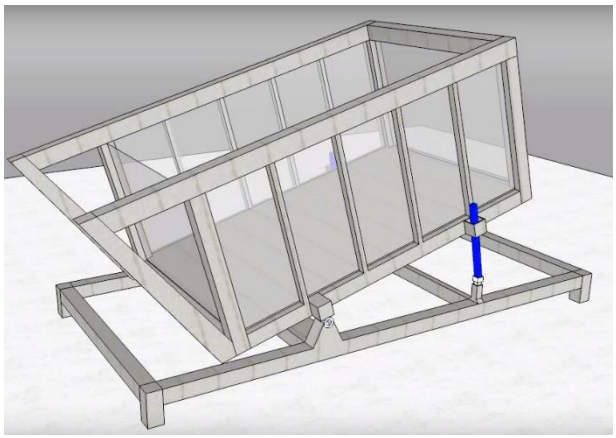

TU Delft Delft University of Technology

Challenge the future

Numerical simulations of static liquefaction in submerged slopes

By

Miguel Angel Chavez Abril

in partial fulfilment of the requirements for the degree of

Master of Science
in Civil Engineering

at the Delft University of Technology,
to be defended privately on Monday August 14th, 2017 at 15:00.

Thesis committee:

Asst. Prof. dr. Amin Askarinejad	TU Delft
Prof. dr. Michael Hicks	TU Delft
Arash Maghshoudloo	TU Delft
Dr. Vahid Galavi	Deltares
Kristina Reinders	TU Delft

TU Delft

Preface

The presented MSc. research project was developed at the Geo-engineering section from the Faculty of Civil Engineering at Delft University of Technology.

I would like to express my gratitude to the Chair of my MSc. thesis committee, Dr. Amin Askarinejad, for offering me the possibility to work on such an interesting and advanced topic of Soil Mechanics. This project offered me the chance to re-visit Soil Mechanics from its most fundamental aspects, up to advanced subjects, from which I am very grateful. I would like to specially thank my daily supervisor Arash Maghshoudloo for his very useful guidance and assistance during this entire process. I also would like to thank Dr. Vahid Galavi for his indispensable help regarding this project, as well as Dr. Michael Hicks and Kristina Reinders.

I express my thanks to Arno Mulder for his assistance in my performed works within the TU Delft laboratory with all the required experimental equipment.

I would like to thank the staff members, friends and classmates of Geo-Engineering for all the great moments that we shared within these two years that I stayed in The Netherlands.

I would like to express my gratitude to The Secretariat of Higher Education, Science, Technology and Innovation of the Republic of Ecuador for awarding me an scholarship to obtain this academic degree.

Finally, I want to express my deepest thanks to my parents, Miguel and Carmen, as well as my brothers and sisters for always supporting me, and their unconditional love. They were my main motivation over these two long years to overcome all possible challenges and achieving this so desired goal.

M.A. Chavez Abril

Delft, July 2017

Table of Contents

Abstract

The static liquefaction tank (SL-tank) is a unique large-scale facility that provides a means to simulate the conditions of a submerged soil slope under failure conditions. Static liquefaction (SL) may be defined as a significant loss of soil's shear strength due to a substantial development of excess pore water pressure under monotonic loads. This complex soil behavior is commonly related to case studies such as submarine flow slides.

The main objective of this project is to use a finite element method (FEM) based on a Hypoplasticity (HP) framework to numerically simulate the experimental data obtained from the Static liquefaction tank facility of Delft University of Technology. A set of Elasto-Plastic (EP) constitutive models were chosen as an initial reference to simulate the SL-tank and afterwards compare their results to the HP framework. The numerical results were analyzed mainly in terms of excess pore water pressure and relating them to experimental data. Additionally, effective stresses, strains and stress paths were examined from the given model outputs.

A fine-cohesion less soil called Geba sand was used in the experimental procedure of the SL-tank, as well as in elements tests performed within this study. The model parameter determination and calibrations were performed by means of element tests, empirical correlations, theoretical formulations, and best-fits from experimental data. Soil behavior at low stresses is of fundamental importance for the performed experiments and numerical simulations in this work.

A potential instability behavior from the given numerical simulations was studied by means of an adopted instability line (IL). The IL criteria is a framework which is commonly illustrated in stress paths as a boundary that delimits a potential susceptibility to soil collapse. Element test data from fine-loose sands, as well as the numerical outputs from this work were used for estimating a potential IL applicable for the scope of this Master's thesis project.

Results of this investigation showed clear limitations of the hypoplasticity constitutive laws in generating sufficient excess pore water pressures and deformations to trigger static liquefaction. Additionally, boundary effects in the assumed fixity conditions were a main potential issue regarding inaccurate results. Nevertheless, an enhanced model response (HP) was observed in comparison to Elasto-Plastic models.

Chapter 1: Research introduction

1.1 General introduction

Liquefaction has been so far one of the major concerns in the area of geotechnical engineering. A basic definition for this phenomenon could be stated as: a reduction of soil effective stresses to values closer or nearly equal to zero, and thus the material exhibiting a liquid-like behavior (null shear strength).

Liquefaction is usually related to strain softening of granular soil (diminishing shear strength with increased deformations) but it is not a sufficient condition for it to occur. For a flow slide to develop, an additional force or triggering factor is needed. Seismic activities, rain water, seepage or other factors may act as this triggering factor. (Charles, 2009)

Regardless of which factor is acting on the affected soil matrix, the result would be a loss of its strength which may lead to a potential failure. Liquefaction is mainly divided as dynamic or static depending if the triggering factor is whether a cyclic or monotonic type.

Static liquefaction (SL) is commonly related to offshore conditions, such as submarine slopes. SL may also be associated to cases for onshore locations in which usually a water body is affecting the stability of tailing dams or any other earth retaining structure in its proximity. (Davies, McRoberts & Martin, 2002)

SL in submarine slopes may be attributed to a local steepening of the existing slope. This Steepening is a scouring process, which is defined as an erosive action that has removed soil by external agents such as tidal forces. Scouring generates a progressive weakening effect as the soil resettles but looser soil state is obtained. (Silvis & Groot, 1995)

An undergoing study is currently taking place regarding a well-known structure in the Netherlands, the Oosterscheldekering (Figure 1.1). This project is the largest of all the dam and storm surge barriers that were developed in the coastal region of the Netherlands in order to protect a large portion of the country against floods. (Watson & Jr., 1990)

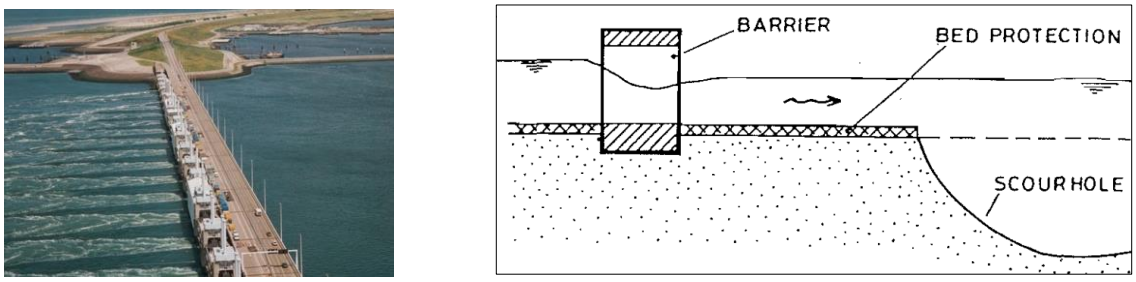

(a) *(b)*

Figure 1.1 – ***(a)*** *Aerial picture of Oosterscheldekering* (Jacobs, 1998). ***(b)*** *Cross-section scheme of the hydraulic structure at the foundation level* (Silvis & Groot, 1995).

Figure 1.1b depicts a scour hole in close proximity of the foundation level from the Oosterscheldekering . The observed scouring process could escalate to such extents as to compromise the stability of the Oosterscheldekering. In order to study such mechanism, the use of physical modeling is a viable possibility. The Static liquefaction tank (SL-tank) is a unique large-scale facility that provides a means to simulate the conditions of a submerged loose-soil slope under a flow slide condition (failure).

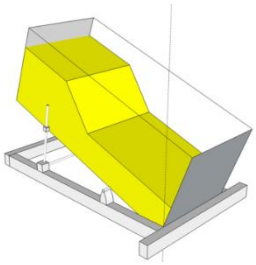

Static liquefaction (failure) is reached in the SL-tank by means of a tilting mechanism. Such a mechanism simulates the steepening action (scouring) occurring in a loose submerged slope and provides a way to analyze how the failure is happening in terms of pore pressure evolution (using sensors) and how this affects the stability of the material.

Figure 1.2 - Scheme of the Static liquefaction tank imposing a tilting mechanism (van de Oever, 2013).

A Proper use of soil constitutive frameworks have provided a way to obtain reasonable results compared to experimental data such as tri-axial and Oedometer tests. There is no available constitutive model that can predict accurately the behavior of all types of soil, as well as the fact that all existing models have their own shortcomings and advantages.

Elasto-plastic (EP) models such as the Mohr Coulomb (MC) or the double Hardening soil (HS) model are well-known first and second degree approaches respectively for soil behavior study. In some study cases such as static liquefaction, these two models fail to reproduce an appropriate soil behavior. Therefore, such EP models are not able to accurately predict the contractive nature of granular soils during progressively softening behavior (liquefaction).

Enhanced EP formulations such as the UBCSAND (UBCS) model are able to simulate enhanced soil responses in regards with liquefaction phenomenon. Nevertheless, even such formulations present shortcomings that question their applicability for reasonably describing the SL behavior.

Advanced models which work under different constitutive laws compared to the classical Elasto-Plastic postulates, may provide a more suitable framework to study the SL behavior. The hypoplasticity (HP) model has shown potential promising results for modelling loose non-cohesive soils.

1.2 Problem definition

Static liquefaction is a complex behavior, given its fast and abrupt nature of occurring. An approach of understanding such a soil phenomenon could be taken by relying on physical and numerical models that aim to simulate the real conditions, by applying assumptions and simplifications of reality in such models.

The study of physical models such as the SL-tank has a main advantage over real-scale tests in terms of having a better control over the given experiment. These benefits translate usually into reduced costs and reproducible experiments but at the expense of compromising the accuracy of the results, which may be significantly affected by ''scaling issues''. Scaling problems may be attributed for some factors, one being the difference in the applied normal stresses. A soil slope of 10m height would exhibit significantly higher stress levels in contrast to a 1m slope. The study of soil behavior at low stress levels (i.e. stresses<100 kPa) is of key importance and a main governing problem in analyzing the experimental results of the SL-tank.

Numerical modelling offers more significant benefits in terms of costs, but at the expense of further inaccuracy in its results as they rely on assumptions that tend to significantly deviate from reality. The main scope of this study is to use numerical modelling to analyze the static liquefaction phenomenon occurring at the SL-tank facility, which implies to numerically simulate a large-scale physical model. It must be noted that no post-failure effects are part of the scope from this research, but merely until reaching failure conditions (SL). The adopted constitutive model for simulating the SL-tank should be able to reasonably predict the stress-strain behavior that leads to SL. The behavior of loose non-cohesive soils under monotonic loads describes static liquefaction, which numerical frameworks such as the Elastic-plastic ones fail to reproduce accurately.

The Hypoplasticity (HP) framework is an alternative approach to Elasto-plastic formulations. The HP model relies on significantly different constitutive laws that describe soil behavior. Certain features of the HP model make it a promising approach for analyzing loose-collapsible soil behavior under monotonic loads. Additionally to the HP model, a complementary framework named the Instability line criteria may aid in assessing the susceptibility for a potential SL event to develop within the numerical and experimental results.

1.3 Research goal

This research project has one main goal and 3 secondary objectives that are the following:

1. The main objective is to simulate the Static liquefaction tank by means of a finite element approach. Prior to numerical simulations, model parameters will be properly determined and calibrated. Fundamental models (MC, HS, UBCS) will be employed at first to analyze preliminary results and then a more advanced constitutive framework (HP) will serve as the final framework for this goal.

2. The second goal is to present the overall advantage of the Hypoplasticity framework in comparison to the fundamental elasto-plastic frameworks that are more commonly used in engineering practice. From past studies, the clear limitation of simple constitutive models have been shown, but it is a main motivation to further promote the use of a different framework such as hypoplasticity.

3. The third goal is to study the potential of instability that may be observed from the numerical results of this work and relate such conditions to the Static liquefaction tank. The instability line criteria will serve as the framework to study the susceptibility of soil collapse (SL) within the scope of this research.

4. The fourth objective is related to studying via experimental element tests the significant effects that very low stresses have upon a tested granular soil. Analyzing this topic is of fundamental importance for the scope of this research project.

Chapter 2: Literature review

2.1 Static liquefaction and soil mechanics fundamentals

2.1.1 General liquefaction definition and contractive soil aspects

Liquefaction may generally be defined as: the mechanism in which a relatively loose soil mass transforms to a liquefied state due to an increase in the existent pore water pressure, and followed by a significant loss of its shear resistance when being subjected to monotonic or cyclic loading. This behavior is a mechanism occurring mainly in non-cohesive soils, which is the case usually for describing clean or silty sands. (Castro, 1969) (Sladen, Hollander & Krahn, 1985).

A contractive behavior is usually expected from a loaded loose soil under drained conditions. This contraction would then be followed by a denser configuration or packing of the soil mass, thus increasing the soil's strength after significant soil deformation occurred.

In undrained conditions, the soil's stability could be compromised at any early or late stage, as the effective stress of the soil would progressively decrease as the pore water increases. The strength loss occurs as a consequence of the contractive nature from the loaded loose soil. Contraction is not allowed due to the incompressibility of the pore water and thus exerting outward stresses that decrease the soil effective stresses. Undrained loose soils are described mainly by strain softening behavior in which the shear resistance is reduced by a continuous development of plastic shear strains. (de Jager, 2006).

Liquefaction develops at a highly fast and sudden rate, which could occur from either drained or undrained conditions. As long as the necessary triggering factor occurs, a sudden undrained behavior could develop and generate failure under significant emerging excess pore pressures. (Kramer, 1988)

2.1.2 Relevant factors attributing to liquefaction potential

There are a two main factors that could affect the incidence of SL in the scope of this research, namely the grain size distribution and the soil's fabric.

The grain size distribution is a fundamental soil characteristic in which the nominal sizes of grain particles are described, as well as the type of gradation that the soil mass has. Regarding liquefaction, a particular range of grain size distribution has been found. Historical flow slides have occurred mainly in loose fine sands of uniform gradation (Kramer, 1988). If a poorly graded distribution is given for a soil, this implies less effective grain-contact forces involved and thus a lower soil strength. Figure 2.1 shows an average particle size of 0.2mm for such silty/clean sands.

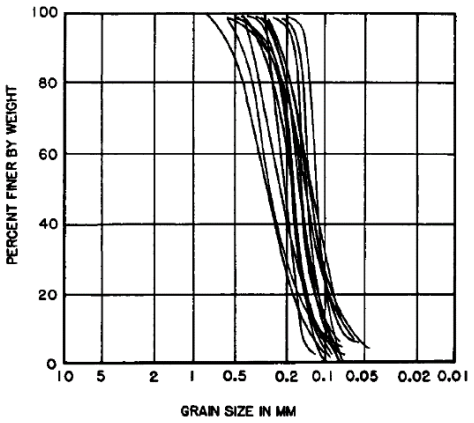

Figure 2.1 – Grain size distribution of historic soil flow slides. (Kramer, 1988)

The soil's structure or fabric, is the total soil skeleton composed of its solid part and voids. A significant soil saturation degree could mean higher pore water pressures and thus higher susceptibility for liquefaction. The soil fabric may be subjected to modifications depending on the current state of the void ratio. A granular soil usually has two boundaries of density state, which are the minimum void ratio e_{min} (upper boundary of densification) and the e_{max} (loosest possible configuration). If the current void ratio is known, a parameter known as relative density (D_r) may be obtained, from which roughly estimated correlations could be employed for assessing the soil's strength and stiffness as well (Brinkgreve, Engin & Engin, 2010). The relative density serves as a main reference to assess the degree of densification in which a granular soil is behaving in a qualitative way.

2.1.3 Fundamental case scenarios regarding liquefaction potential

A non-cohesive soil slope may fall into four main categories of liquefaction susceptibility when it is subjected to shear loading (Davies, McRoberts & Martin, 2002).

1.- If the soil is exhibiting a rather brittle and strain softening behavior, this may imply reaching liquefaction with the possibility of limitless deformations. In other words this is a contractive behavior while shearing until the critical state (see section 2.1.4) is reached.

2.- A limited strain softening which would translate into a relatively low liquefaction susceptibility with restricted deformations. The soil usually contracts at the early stage and dilates afterwards.

3. - A ductile behavior while the soil is sheared but no significant amount of strain softening is inducing liquefaction. This case may be attributed to a material in which liquefaction potential may or may not be relevant.

4.- Strain hardening of the soil which means dilation, is not exhibiting any liquefaction potential or deformations that could trigger such mechanism.

2.1.4 The critical state

The critical state (CS) may be seen as a unique state in which a soil continuously deforms at constant stresses and no further volumetric changes occur. This state describes the soil's behavior at the ultimate (failure) condition (Roscoe, Scho eld & Wroth, 1958) . The critical state of a particular granular soil may act as a boundary line that separates loose (contractive) from dense (dilative) behavior and is also considered an equilibrium at the long stage of stress development. As the CS revolves around volumetric dependency, the void ratio ***e*** and mean effective stresses of the soil are two main parameters that are mainly related to this state. Figure 2.2 illustrates the critical state as a line that separates the two main granular soil behaviors in terms of void ratio and a best-fit logarithmic expression of the mean effective stress (confining pressure for isotropic conditions).

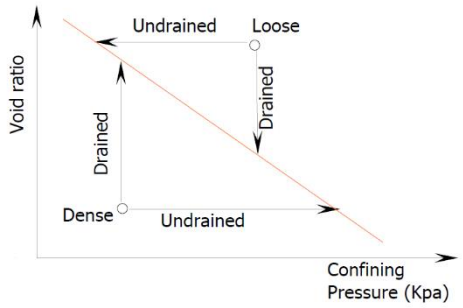

*Figure 2.2 – Critical state line represented in a **e**-log p' plot.*

Depending on the soil drainage conditions, the material could approach the critical state line (CSL) in different ways as seen in log p'-***e*** of Figure 2.2. This difference in paths for approaching the CSL is related to if whether the incompressible behavior of pore water is acting or not in the soil matrix.

From the log p'-***e*** plot (Figure 2.2) it may be inferred that at higher void ratios a dense sand would reach the CSL , as well as if the confining pressure p' is increased. For a contractive soil, lower void ratios would lead to the CSL, as well as the decrease of the mean effective stress p'.

The critical state generates a pseudo linear relationship between the 2 main stress definitions, the isotropic effective stress p' and the deviator stress q. This linear relationship is in terms of a friction angle at the equilibrium state in which large deformations may occur (critical state) and is defined as the constant volume angle φ_{cv}. (Been, Jefferies, Hachey, *et al.*, 1992)

One of the most practical approaches to study a soil's stress evolution is by means of the p'-q space, in which the stress paths may be observed as well as the critical state of the given soil. Figure 2.3 depicts common stress paths in p'-q space for loose, medium dense and dense configurations of a same soil type.

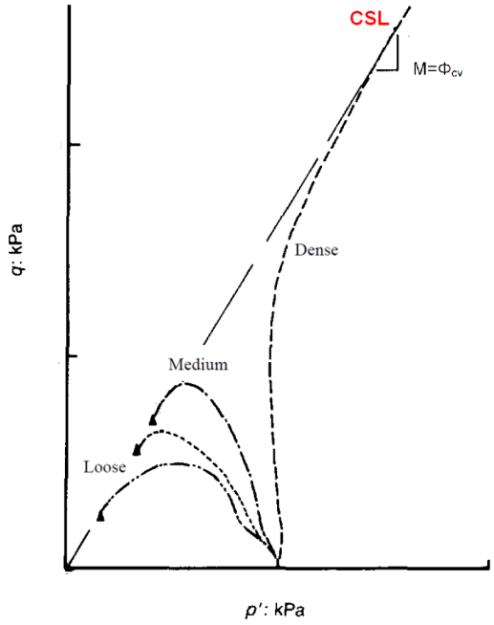

Figure 2.3 – p'-q space of a soil at different initial conditions until CSL is reached. (Eckersley, 1990)

The most prominent trait from the 4 observed stress paths (Figure 2.3), is that they reach the same critical state line (CSL), regardless of their initial stress or void ratio conditions. The parameter $M=\varphi_{cv}$ (slope of CSL) may be seen as an invariant value of a particular soil. The stress path behavior may be described as dilatant if it tends to shift towards the right, which implies that a strain hardening behavior is taking place. As strains develop, the stiffness of the stressed soil tend to increase by a mobilization of its strength until the critical state is reached. Loose samples would be subjected to a strain softening that would thus shift the stress path towards the left (decreasing mean effective stress p') in which stiffness would be gradually decreasing due to the contractive behavior and would thus reach the CSL.

The knowledge of the initial state of the soil (***e***) and the critical state void ratio e_{cv} (at CSL) is of fundamental relevance regarding liquefaction susceptibility. The comparison between ***e*** and e_{cv} related directly to the possibility of liquefaction. Since the parameters e_{cv} and ϕ_{cv} at the critical state will be invariant, knowledge of this state is of important use for this particular study. (Been, Jefferies, Hachey, *et al.*, 1992)

2.1.5 State parameter Ψ

The state parameter $\underline{\Psi}$ is a framework to predict the liquefaction sensitivity of granular soils by being based on the concept of void ratio with respect to two references (initial and critical) (Been & Jefferies, 1985). This approach allows to express the soils stresses and confining state (void ratio) with respect to the critical state line. The state parameter $\underline{\Psi}$ may be defined as:

$\underline{\Psi} = e - e_{cv}$

A similar plot to Figure 2.2 is shown at Figure 2.4 but now the state parameter is the one describing the state at which the soil is with respect to the constant volume state (critical state). A negative $\underline{\Psi}$ would mean a dilatant soil, while a positive one would relate to a contractive granular material. The value $\underline{\Psi}$=0 defines the CSL position. Knowledge of how close $\underline{\Psi}$ is to a negative value or how high it is, it will definitely influence the potential of liquefaction.

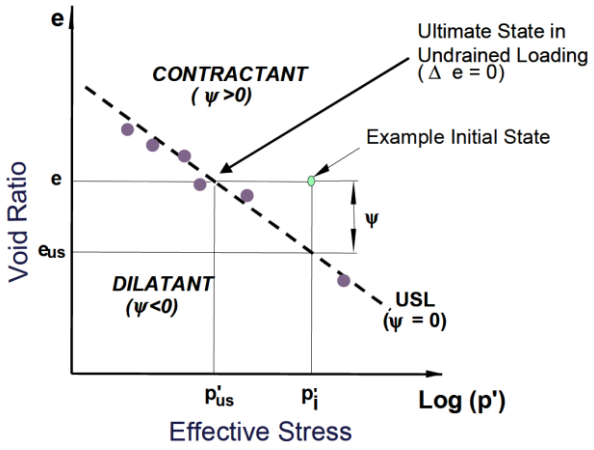

Figure 2.4 – State parameter in e-log p' space. (Davies, McRoberts & Martin, 2002)

In engineering practice, a generally acceptable value for assessing possible liquefaction behavior is to use a $\underline{\Psi}$ = -0.10 as a reference boundary. Obtained state parameter values should be at least lower (more negative) than -0.1 to ensure a lesser susceptibility for instability during undrained loading is occurring, but provided that the drained strength is sufficient at all loading conditions. (Davies, McRoberts & Martin, 2002)

The main challenge in using this framework for predicting liquefaction susceptibility comes from the estimation of the term e_{cv}. Contrary to φ_{cv}, the critical state void ratio is not a stress-independent parameter. Some theoretical formulations have been proposed to compute this parameter but they rely on other parameters that are complex and not straight-forward to obtain by conventional means (Sfriso, 2009). An important remark regarding e_{cv}, is its peculiar behavior at low mean effective stresses (Sfriso, 2009). Toyoura sand, a very fine cohesion-less soil, is used as reference to compare the stress dependency of e_{cv} over a wide range (Figure 2.5).

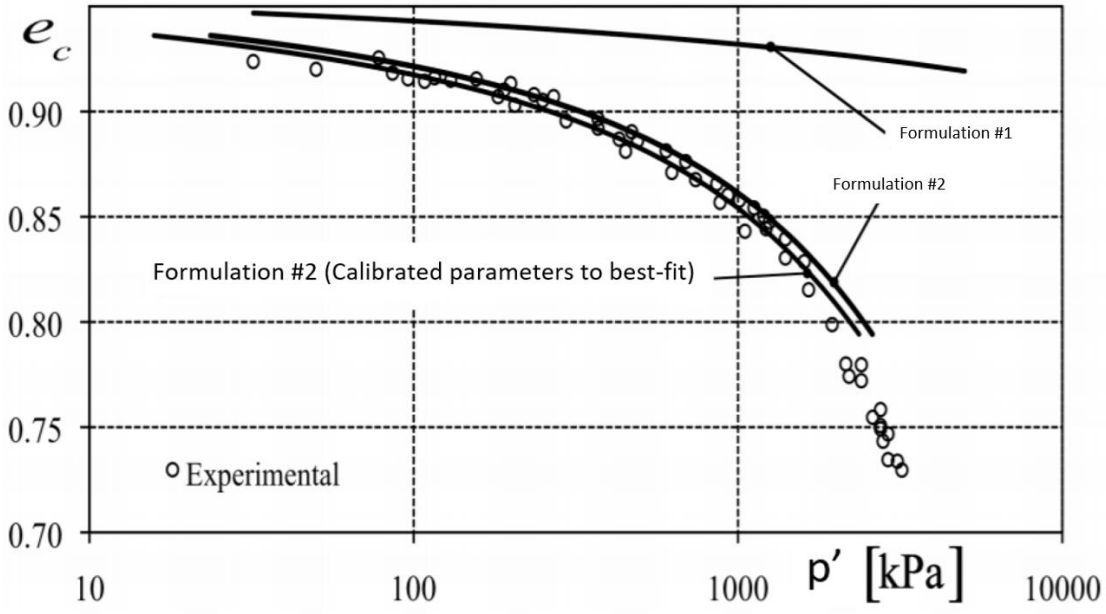

Figure 2.5- Stress dependency of e_{cv} for Toyoura sand. (Sfriso, 2009)

The results from Figure 2.5 have a relevant characteristic for the low stress levels (i.e. mean effective stresses of p'<100 kPa). For Toyoura sand, a measured maximum void ratio is e_{max}=0.98 (Herle & Gudehus, 1999). From the observed experimental results, e_{cv}=0.96 is given confining stresses of p'= 50 kPa. By extrapolating these results, at very low mean stresses it may be adopted an approximation such as $e_{max} \approx e_{cv}$.

2.1.6 Instability in liquefaction phenomenon

A general framework for assessing soil failure by means of the critical state provided reasonable results for common geotechnical applications. However, this does not necessarily mean that the stressed soil cannot be susceptible to liquefaction if it has not reached the CSL. Liquefaction has mainly developed in undrained loose sands. A concept named the instability criteria is reached when the soil may or may not be able to sustain the current stress state (Lade, 1993). In terms of yield surfaces (mobilized shear strength), the instability condition would be reached at the top of such a yield surface. After reaching this point, soil may perceive large plastic deformation, leading to liquefaction. (Lade & Pradel, 1990)

A nearly straight line in stress spaces p'-q has been observed to cross at the peak deviator stress that define instability points within the stress path. This line was named the instability line (IL) and may be constructed if undrained experimental data is available. Data involving effective stress paths of a tested soil with constant initial void ratio e_0 but at different confining pressures is necessary (Figure 2.7). The IL is located below the CSL.

While the CSL may be seen as an upper boundary, the IL is acting as the lower boundary of a region named the instability zone in which a loose soil will become unstable when undrained loading is taking place (Lade & Pradel, 1990) .One of the most prominent features of the IL is that instead of being unique as the CSL, it will change due to a void ratio dependency (Figure 2.6). Figure 2.6 depicts a tested soil under different initial e_0 but at the same confining stress of 150 kPa. If the initial void ratio $\boldsymbol{e_0}$ is smaller than some reference $\boldsymbol{e}$, then the IL will be located at a higher location in the q-p' space. If the IL gets at a higher location, this implies that the instability zone is smaller and thus susceptibility for liquefaction is diminished as well. Figure 2.7 shows the instability line and zone for a tested contractive soil.

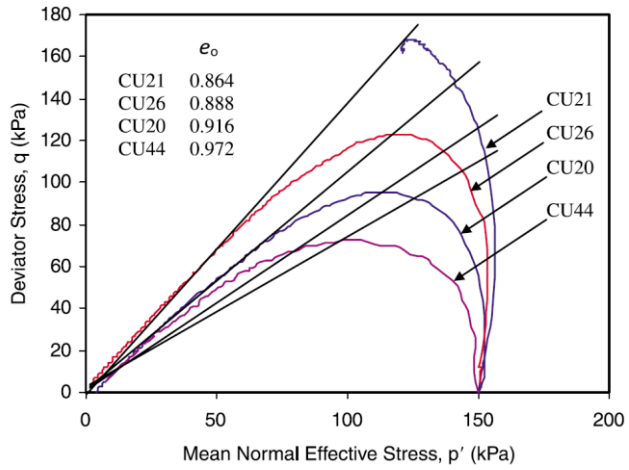

Figure 2.6- Non-uniqueness of the instability line IL under different e_0 (Chu, Leroueil & Leong, 2003).

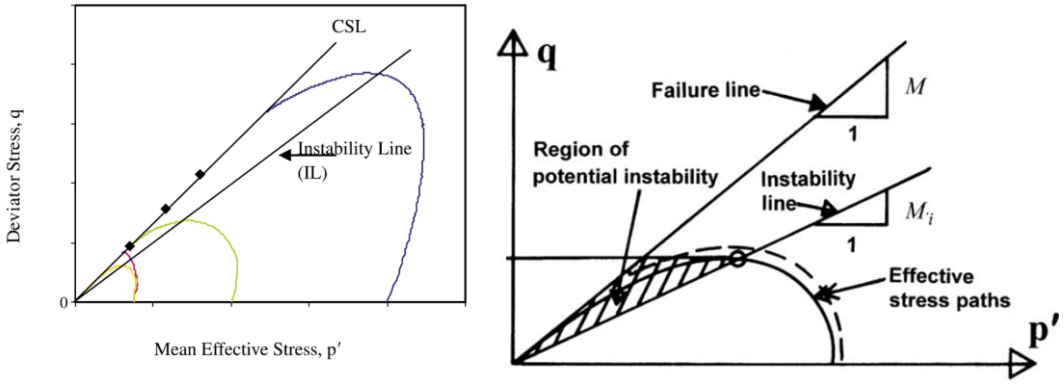

(a) *(b)*

*Figure 2.7– **(a)** IL schematized for a contractive soil tested at a constant **e** but varying confining stresses.* (Chu, Leroueil & Leong, 2003). ***(b)** Instability zone at a particular **e** and confining stress* (Lade & Yamamuro, 2011).

Dense sands will less likely be affected by liquefaction. In an undrained case, the soil's dilatant behavior will increase the existing effective stresses. Only in a drained case instability may occur,

provided that large plastic strains are developed. Regarding static liquefaction potential (instability), such large plastic strains are more related to dynamic behaviors or post-failure liquefaction events. As a consequence, dense sands are less likely related to static liquefaction.

For loose sands, a drained instability is not so likely to happen due to the contractive nature unless the imposed stresses in the soil change. The slope of the IL could be as high as nearly matching the CSL when referring to loose sand. (Chu, Leroueil & Leong, 2003)

The phenomenon of instability may be described by two possible mechanisms that generate it, either a progressive strain until failure or a sudden acceleration in the soil matrix. The instability region does not depend on the imposed drainage conditions, so either way the selected stress path will reach such zone. (Chu, Leroueil & Leong, 2003)

The two instability mechanisms described before are defined as a runaway type and a conditional type. The runaway type is a fast unstable response, generally associated with undrained conditions. The conditional type is much slower (drained condition) and may only occur along the stress path by means of a reduction of the effective stress p'. When the void ratio changes in loose soils, the slope M_L of the instability line exhibits a high sensitivity of its slope angle. In the other hand, dilative soils show gradual changes in the slope angle M_L by variations of the void ratio. (Eckersley, 1990)

For instability to occur, plastic yielding of the granular soil is a necessary condition but not sufficient. While yielding generates a development of large strains for small changes in applied stress, it does not imply instability. An unstable condition for this case would relate to a sudden increase in the strain increment rate (axial strain over time).

A comprehensive summarized data of 7 loose fine sands was performed by, from which an average φ_{cv}=30° and a friction angle related to the instability line φ_{il}=17° were reported (Sladen, Hollander & Krahn, 1985). From these results, it may be inferred that the ratio of (φ_{cv}/ φ_{il}) for loose fine sands is approximately 1.77. This ratio will be used in this study as an additional reference for analyzing the instability zone. The observed ratio (φ_{cv}/ φ_{il}) of these experimental tests were done at medium-high stress levels (i.e. p'>100 kPa).

2.1.7 Loose soil behavior at very low confining stresses

The study of soil's shear strength commonly involves a soil mass that is subjected to stress levels(i.e. static and/or dynamic loads) that are approximately at 100kPa or higher. Limited data is available regarding the behavior of soil mechanics at stress levels lower than 100kPa. A definition for medium-low stress ranges could be used within (50÷100)kPa and very low stress ranges being of (0÷50)kPa.

The main cause for a different shear strength behavior at low stress levels, may be due to the soil dilatancy (Ponce & Bell, 1971) . Dilatancy is the volumetric change that occurs while having shear strains of materials such as cohesion-less soils. This behavior is usually characterized by the dilatancy angle ψ, which may be defined as a ratio of plastic volume change to plastic shear

strain (Bolton, 1986). ψ controls the development of plastic volumetric strains during plastic shearing and assumed to be constant at critical state conditions. The dilatancy angle is usually only taken into account for sands, since cohesive soils tend to have negligible ψ values. The degree of dilation may be related to the density state of sands, loose sands having usually ψ=(0÷10) ° and dense sands values around ψ=15° (Vermeer & de Borst, 1984). The commented values of dilatancy angle are within medium-high stress ranges of soil mechanics, but not for very low stress levels around (0÷50)kPa.

The dilatant behavior occurring at the low stress domain may be mainly attributed for significant changes in the existing deformation mechanisms or the soil fabric. These mechanisms may show additional behaviors such as rotational deformations combined with sliding. Such conditions may occur due to high energy-intensive modes of deformation at are required during the shearing process at such low stress levels.

From experimental results at stress levels around (0.2÷1) kPa, it was found that the dilatancy angle of a tested fine sand (Ottawa sand) was as high as ψ =30° (Sture, Costes, Batiste, *et al.*, 1998). Such a high dilatancy angle vastly surpasses the findings of other experimental studies at medium-high stress ranges.

A higher degree of dilatancy means that the shear strength mobilization is taken to a larger extent as. Figure 2.8a show a proportional increase of dilatancy angle with increased relative density for a confining stress of 1.5 kPa or 0.20 psi. Figure 2.8b illustrates a significant increase in dilatancy as a consequence of applying confining stresses as high as 30Kpa or 4 psi.

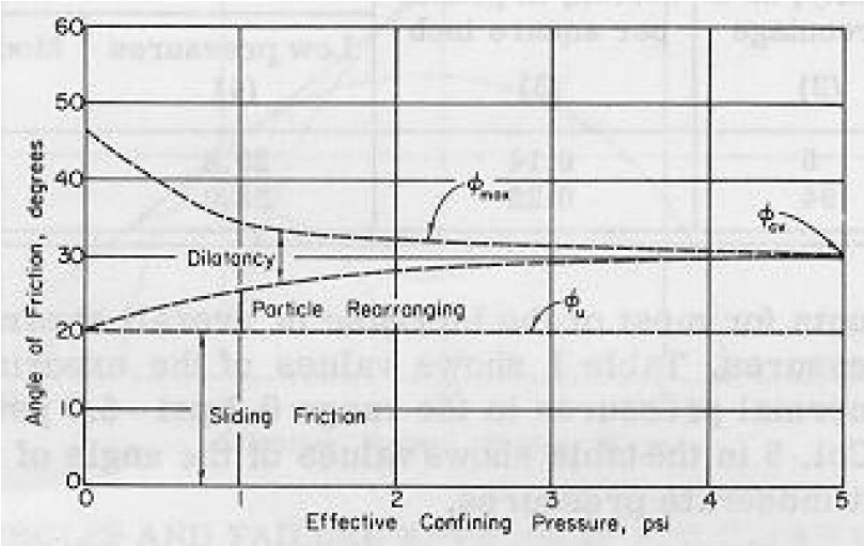

(a)

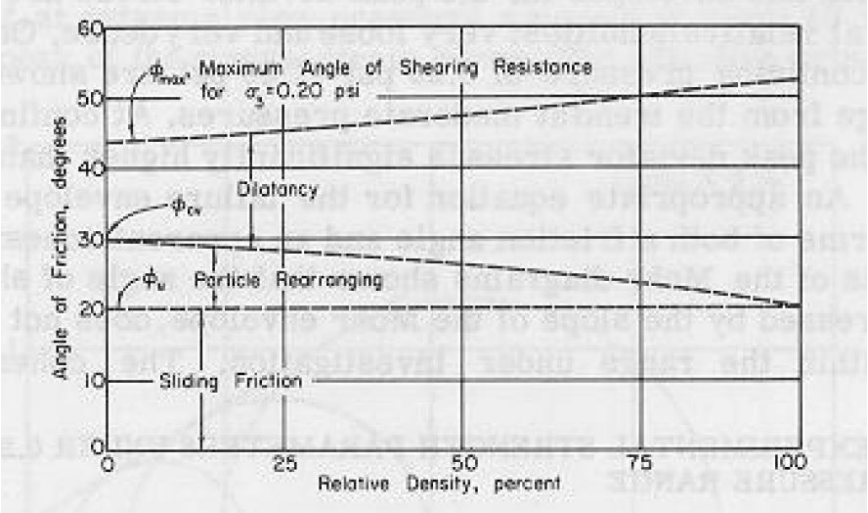

(b)

Figure 2.8 Low stresses effects over dilatancy with confining stress ***(a)****, and* D_r ***(b)*** (Ponce & Bell, 1971)

As φ_{cv} is state independent, the dilatancy component is the main factor that contributes to the high increase in the peak friction angle ϕ_p. In the low stress range, extreme quantities as high as φ_p=70° have been obtained (Sture, Costes, Batiste, *et al.*, 1998).

A comprehensive set of results presented in Figure 2.9 shows how ϕ_p changes with the applied confining pressure at a wide range of stresses. This serves as an additional evidence of how much dilatancy affects the overall shear strength at low stress levels.

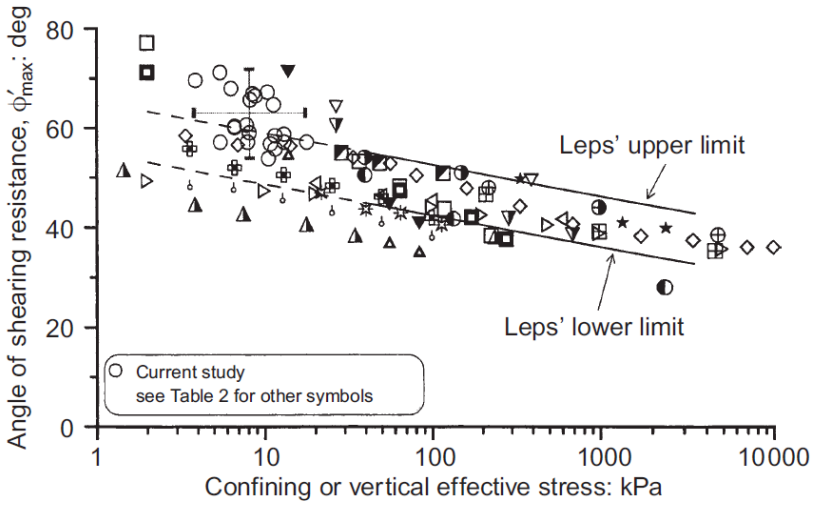

Figure 2.9 Effects over peak friction angle over a wide range of confining pressure (Fannin, Eliadorani & Wilkinson, 2005).

The elastic stiffness at low stresses may follow approximately the results of non-linear calculations based on a reference elastic modulus (E_{50ref} and a reference stress level P_{ref}) (Gay, Boutonnier, Flavigny, *et al.*, 2003).

2.1.8 Infinite slope equilibrium analysis

The infinite slope method is a simple mechanical approach based on equilibrium conditions and other fundamental assumptions such as the following:

- The slope extent (length and width) must be significantly larger than the depth of the potential slip surface.
- The slope angle must remain constant and not be too large(i.e. angles around [0÷30]°)
- The triggered failure mechanism is parallel to the slope's ground surface (planar failure).
- Linearly elastic perfectly plastic (Mohr-Coulomb) constitutive framework on the sliding surface
- Pseudo-static components serve as a means to mimic seismic conditions.
- The ground water flow is a direction parallel to the slope.

This basic slope stability method proceeds through an analytical solution for usually evaluating the failure potential in terms of a factor of safety. The model solution depends on several factors such as the slope angle, depth of potential failure surface, hydrostatic conditions, shear strength parameters, unit weight of the soil mass and pseudo-static components. (Urciuoli, 2001).

A simplified model regarding the Static liquefaction test was performed to analyze a similar case to the one presented at Chapter 6. This simple analytical model based on an infinite slope analysis may be found at Appendix E.

2.2 Constitutive soil frameworks for modelling sands

Numerical modelling is the main tool for the scope of this research in order to simulate the SL-tank. For this study, a total of 5 constitutive soil models were used. Three of them rely on the classical elasto-plastic (EP) framework, while two were based on an entirely different mechanical basis. Linear elastic perfectly plastic (Mohr Coulomb), Double hardening model (Shear hardening), and the UBCSAND model are the chosen EP models. The standard hypoplasticity (von Wolffersdorff's version) model and it's extended version named the hypoplasticity with intergranular strains model (Niemunis's version) are the two non-elasto-plastic frameworks used as the main scope of this research. All the aforementioned models are implemented in the available platform for this research, which is the finite element analysis software named PLAXIS.

2.2.1 Linearly elastic perfectly plastic model (MC)

The most simple yet widely used constitutive model for many geotechnical applications, is the Mohr-Coulomb model (MC). This model was the first recognized framework to serve as a first-degree approach in order to simulate a soil's behavior.

Linear elasticity, as described by the Hooke's constitutive law of isotropic elasticity is one of the two main components of the MC model. Pure elasticity, as it is known, does not consider any failure condition or non-recoverable deformations. Hooke's law revolves around a basic constitutive equation which is defined by an elastic material matrix **M**, as observed in the following Equation 1:

$$\sigma = \mathbf{M} \cdot \varepsilon \qquad \text{(Eq. 1)}$$

The **M** matrix is characterized by two parameters, the Poisson's ratio *v* and the elastic modulus **E**. Other auxiliary definitions emerge from the 2 main parameters such as the one-dimensional (Oedometer) Elastic stiffness E_{oed}.

The second main component of the MC model is the plastic behavior, which involves the generation of unrecoverable deformations. The total characterization of strains ε (deformations) is a sum of elastic strains ε^e and plastic strains ε^p.

A yield surface or function **f** is what determines whether plasticity is occurring or not. This function **f** is fully fixed in the MC model. Hence, the name of perfect plasticity, as the yield function is not able to expand by mobilizing the plastic strains until failure may be reached. As long as **f**<0 , elastic conditions are ensured, while if **f**=0 then perfect plasticity (failure) occurs. It is impossible to violate the limit of the yield function, which coincides with the failure surface for MC. (PLAXIS, 2016)

f acts as a condition to trigger failure and it is based on Coulomb's friction law but it may be applied to any plane within the analyzed material. The yield function depends on: stress conditions at two or more planes, the friction angle φ and cohesion **c** parameters.

An additional component named the plastic potential function **g** is used for this framework as a way to use a non-associated plasticity, in contrast to the classical associated plasticity. If an associated plasticity is given (i.e. **f**=**g**) then the model overestimates dilatancy. The **g** function depends on: stress conditions at two or more planes and in the dilatancy angle ψ.

The MC model needs a total of 5 input parameters which are:

Elastic modulus	E
Poisson's ratio	*v*
cohesion	c
Peak friction angle	φ_p
Dilatancy angle	ψ

This model has several flaws which hinder the possibility of it to accurately estimate a soil's behavior. The first main disadvantage, is that real soils exhibit non-linear stress-strain relations, while MC relies of purely linear behaviors.

The second fundamental issue is that real soil behavior is described by a stress dependency. The most notorious parameter to exhibit stress dependency is the elastic stiffness modulus **E**. The soil Stiffness changes through different stress levels, from which the MC could be underestimating or overestimating the soil's stiffness response. The friction and dilatancy angles are also affected by the applied stress levels. Additionally, there is no distinction between unloading and reloading stiffness, something of crucial importance for application such as excavations, dredging, etc.

The third main drawback of this model is that the shear strength of the material is never mobilized through expanded yield surfaces until failure is reached. This means that the yield function **f** is fixed and no accumulation of plastic strains is ever occurring, since failure is instantly reached as soon as plastic strains occur.

Under drained conditions, this model has shown reasonable results of soil behavior but when undrained conditions are considered, this model tends to overestimate the soil strength. This kind of undrained model response would be erroneous to assume for loose non-cohesive soils (Tjie, 2014).

2.2.2 Non-linear elastic double hardening model (HS)

The hardening soil model (HS) was proven to significantly outperform the MC through new features such as non-linear behavior, stress dependency, and shear strength mobilization (Hicks & Wong, 1988). The commented enhanced aspects in comparison to the classical elasto-plastic formulation of MC, allowed the HS to become a second degree constitutive model for simulating soil behavior.

A hyperbolic formulation is used to describe the axial strains and deviator stresses through a tri-axial loading. A parameter named the failure ratio R_f is used as a cut-off of the asymptotic behavior of the hyperbolic formulation. R_f is usually adopted as 0.9.

The following constitutive equation deals with the stiffness dependency for the unloading-reloading stress paths E_{ur} stiffness, as well as the primary loading stiffness E_{50}:

$$E_x = E_x^{ref}\left(\frac{c\cos(\varphi)-\sigma_3'\sin(\varphi)}{c\cos(\varphi)+P_{ref}\sin(\varphi)}\right)^m \quad \text{(Eq. 2)}$$

From which **x** may denote either a secant elastic modulus at 50% of the deviator stress (E_{50}), or the unloading-reloading stiffness (E_{ur}). This expression relies on a pressure reference P_{ref}, a referential stiffness E_{ref} and a power exponent **m** which is a rate of stress dependency. The reference stiffness E_{ref} is usually chosen as 100kPa and for sands **m** is usually taken as 0.5.

Two factors define the double hardening criteria, meaning how the model allows for a mobilization of its strength until failure is ultimately reached. The first factor is a shear hardening yield function **f** which is directly related to the plastic shear strains developed, which in a way ''pushes-outwards'' the current yield surface closer to the failure line. **f** may be mobilized, meaning increasing plastic strains until it is no longer able to expand more and the criteria of failure **f**=0 is reached. The parameter named plastic shear strain Υ_p is the main component that aids in defining the shear hardening yield function, and may be approximate defined as 2 times ε_1^p (axial plastic strain). The second factor is a plastic potential function **g** which deals with the plastic volumetric strains ε_v^p. **g** is related to a flow rule that defines relationships of plastic stain rates. The given flow rule for HS depends on the mobilized dilatancy angle ψ_m. The commented plastic potential function and flow rule of HS may be related to the known stress dilatancy theory by Rowe (1962).

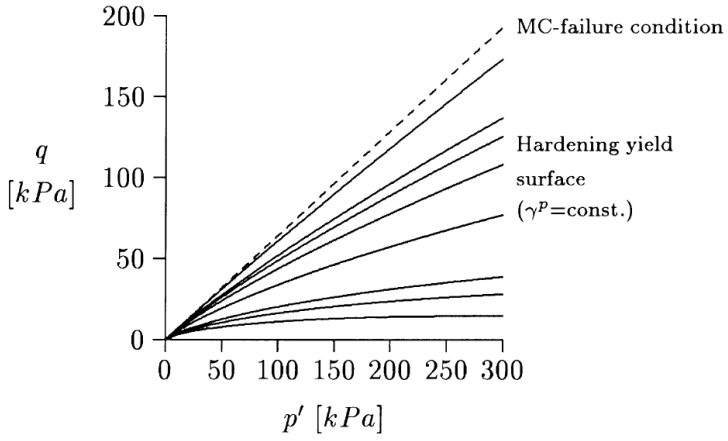

Figure 2.10 Yield surface mobilization in stress path p'-q (Schanz, Vermeer & Bonnier, 1999).

The stress-dilatancy theory essentially states that a material contracts when φ_m is lower than φ_{cv}. In the other hand, a material dilates if $\varphi_m > \varphi_{cv}$. This behavior depends on the mobilized strength in comparison to the critical state strength. (Schanz, Vermeer & Bonnier, 1999) (Ti, Gue See, Huat, *et al.*, 2009)

As stated before, the use of a double hardening criteria (shear and volumetric) serves for generating progressively increasing plastic strains. **f** focuses in mobilizing the shear plastic strains as well as shear strength until reaching failure, while **g** controls the generated volumetric plastic strains.

This constitutive model needs a total of 11 main input parameters which are:

Elastic modulus	E_{50}
Unloading-Reloading stiffness	E_{ur}
Oedometer stiffness	E_{oed}
cohesion	c
Peak friction angle	φ_p
Dilatancy angle	ψ
Power exponent	m
U-R Poisson's ratio	v_{ur}
Failure ratio factor	R_f
Lateral earth pressure at rest	K_o
Reference stress	P_{ref}

The main drawback of the HS model is its lack of softening behavior. This could be explained by means of the stress dilatancy theory commented before. If the mobilized strength is lower than the critical state conditions, the shear hardening flow rule of the HS model is not taken into account, hence no softening behavior is modelled at all. For contractive soils, this proofs to be a crucial drawback in order to predict an accurate behavior. (Schanz, Vermeer & Bonnier, 1999).

Figure 2.11 shows a lower boundary denoted for softening behavior, which the HS is unable to replicate. As the name of the model implies, only hardening mobilization of friction angle φ_m by increasing it until reaching the peak φ_p may be modelled.

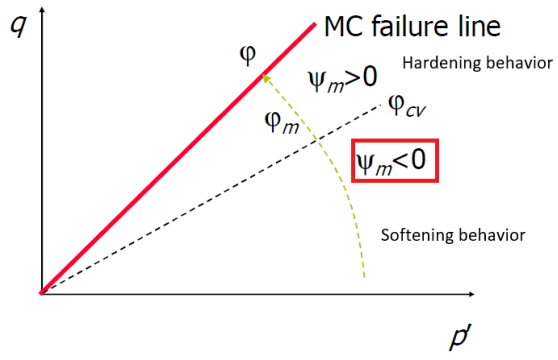

Figure 2.11 Limitation of HS model regarding softening behavior

2.2.3 UBCSAND model (UBCS)

The UBCSAND (UBCS) model forms part of the classical elasto-plastic framework such as the MC and HS but it may be seen as a third degree of constitutive modelling for the case of soil softening behavior, which MC and HS fail to model.

Regarding fundamental definitions of elasto-plasticity as the ones commented for MC and HS, most of the definitions explained for EP models are also applied for UBCS as well (Makra, 2013).

UBCS uses a hyperbolic strain hardening rule, similar to the HS. The yield criteria **f** is based on the Mohr-Coulomb principle yield surface, as well as possessing a non-associated plastic potential function **g**. The main difference regarding HS or MC and UBCS is the flow rule in which this model uses the stress-dilatancy theory to its full extent, meaning that strain softening is allowed as well. (Petalas & Galavi, 2013)

The elastic behavior of this model is related in terms of four model parameters and the applied reference stress levels. These 4 parameters are the elastic bulk modulus K_{B}^{e}, the elastic shear modulus K_{B}^{e} and two elastic exponents m_e and n_e.

The adopted hyperbolic hardening rule is related to other 3 parameters at a particular stress reference. These 3 parameters are the plastic shear modulus K_{G}^{p}, a plastic shear exponent n_p and the failure ratio R_f.

The plastic potential function **g** mainly depends on the dilatancy angle ψ, the lode angle θ, and friction angle φ. The flow rule of this framework is different to the ones of MC and HS, although it still based on the stress dilatancy theory. This flow rule allows for simulating a pronounced contractive response, which is the key for modelling static liquefaction.

Additionally to the commented features, UBCS has other parameters (fac_{hard}, fac_{post}) that are of relevant importance when considering cyclic behaviors as the perceived ones through earthquake loads. When using monotonic responses the mentioned parameters have no relevant importance to describe the soil's behavior. As cyclic loads are not part of this study, they will not be mentioned in further detail.

The main advantage from this model is its simplicity for application, regarding the parameter determination, which may be performed by best fitting of tests such as tri-axial or direct shear. The parameters may be even estimated based on SPT N_{60} correlations, which at the same time could prove to be not reliable for more demanding geotechnical applications (Makra, 2013). The 11 needed input parameters for UBCS are listed below as :

Critical state friction angle	φ_{cv}
Peak friction angle	φ_p
Cohesion	c
Elastic bulk modulus	K_B^e
Elastic shear modulus	K_G^e
Plastic shear modulus	K_G^p
Elastic bulk exponent	m_e
Elastic shear exponent	n_e
Plastic shear exponent	n_p
Failure ratio	R_f
Reference stress	P_A

The following equations are SPT correlations may be used for parameter determination:

$$K_G^e = 21.7 \cdot 20 \cdot (N)_{60}^{0.333} \quad \text{(Eq. 3)}$$

$$K_B^e = K_G^e \cdot 0.7 \quad \text{(Eq. 4)}$$

$$K_G^p = K_G^e \cdot (N)_{60}^2 \cdot 0.003 + 100 \quad \text{(Eq. 5)}$$

$$\varphi_p = \varphi_{cv} + \frac{(N)_{60}}{10} \quad \text{(Eq. 6)}$$

$$R_f = 1.1 \cdot (N)_{60}^{-0.15} \quad \text{(Eq. 7)}$$

Additionally, the SPT corrected number N_{60} may be estimated by the following empirical equation 8:

$$N_{60} = (D_r)^2 \cdot 46 \quad \text{(Eq. 8)}$$

The main disadvantage of this model lies in its potential to simulate realistic deformations. The model response could overestimate the amount of deformations from a result involving liquefaction behavior.

This model's main intended application is for earthquake engineering with regard of cyclic loads and enhanced prediction of excess pore water pressure generation. Nevertheless, its ability to generate soil contraction is still of relevant importance for the study's scope. Because of its simplicity in parameter determination, it will serve as an auxiliary model to study the static liquefaction phenomenon.

2.2.4 Hypoplasticity model (von Wolffersdorff's HP)

The traditional elasto-plastic formulations such as HS model, rely on a clear distinction between the elastic and plastic domain a soil may be subjected to. Such EP formulations make use of yield and plastic potential definitions, as well as flow (hardening) rules. For the Hypoplasticity (HP) model, the aforementioned qualities of EP models are not needed.

Hypoplasticity could be defined as an explicit interdependence of strain rate and stress rate direction (Dafalias, 1986). HP's framework is a constitutive law of the rate-type, implying a relationship that associates strain rate to stress rate. (Kolymbas, 1991)

As a first impression from this model, the main features that it describes from soil behavior, are a non-linear stress dependence of stiffness and the inclusion of contractive-inelastic behavior.

The motivation of this alternative constitutive framework was to have a means to describe non-cohesive soils by means of the grain's properties or more specifically the grain's assembly. At first it could look promising to describe the mechanical behavior in terms of granulometric properties such as the coefficient of uniformity C_u, but this is far from being practical. Real soil behavior is too complex to simply describe it by single grains only. However studying the grain assembly as a continuum may proof to be resourceful. (Herle & Gudehus, 1999)

Effects such as grain crushing, heterogeneous interparticle contact and grain erosion are neglected for this framework. This assumption leads to a ''simple grain skeleton'' which would then rely on a permanent grain size description. A general formulation may be adopted for HP:

$$\dot{T} = h(T,D,e) \qquad \text{(Eq. 9)}$$

From Equation 9, four basic components of such formulation may be observed. can I $\dot{T}$ defined as the skeleton stress rate tensor, which would be a representation of the mean grain contact forces in the soil's continuum. ***T*** is the soil skeleton's stress tensor, **D** represents the strain rate, and ***e*** is the void ratio. These 3 main components conform the non-linear tensor-valued function **h** that describes the constitutive relationship. (von Wolffersdorff, 1996)

Enhanced formulations such as Equation 10 have been defined for the HP model, from which the following constitutive equation is the one adopted for this projects scope:

$$\dot{T} = \frac{f_s}{tr(\hat{T}\cdot\hat{T})}\left[F^2 D + a^2 \hat{T}\, tr(\hat{T}\cdot D) + f_d a F(\hat{T}+\hat{T}^*)\|D\|\right] \qquad \text{(Eq. 10)}$$

From Equation 10, the Cauchy stress tensor $\dot{T}$ and strain rate **D** may be seen, as well as two scalar factor f_s and f_d, a deviator stress ratio tensor **F**, and a parameter named **a**. A remark will be done specifically for the factor f_s which is shown in the following Equation 11:

$$f_s = \frac{h_s}{n}\left(\frac{1+e_i}{e_i}\right)\left(\frac{e_i}{e}\right)^{\beta}\left(\frac{-tr(T)}{h_s}\right)^{1-n}\left[3+a^2-\sqrt{3}a\left(\frac{e_{i0}-e_{d0}}{e_{c0}-e_{d0}}\right)^{\alpha}\right]^{-1} \quad \text{(Eq. 11)}$$

The factor f_d may considered as a pressure dependent relative void ratio and it is one sub-component that forms part of the factor f_s. The influence of mean soil skeleton pressure as well as the void ratio ***e*** are considered in the HP framework due to the factor f_s. Several model parameters are included inside the formulation of f_s (Equation 11) , which will be discussed in further detail in this section.

$$\frac{e_i}{e_{i0}} = \frac{e_c}{e_{c0}} = \frac{e_d}{e_{d0}} = \exp\left[-\left(\frac{3p_s}{h_s}\right)^n\right] \quad \text{(Eq. 12)}$$

From Equation 12, it may be seen a dependence of void ratio states (e_i, e_c, e_d) with respect to a mean stress pressure P_s and two parameters, namely the granulate hardness h_s and an exponent **n**. These three void ratio parameters decrease with an increasing confining pressure P_s until they reach a state of nearly zero pressure P_s in which they represent the diminished void ratio values of e_{i0}, e_{c0}, e_{d0}. Figure 2.12 illustrates a linear scale representation of this void ratio dependence over an applied P_s.

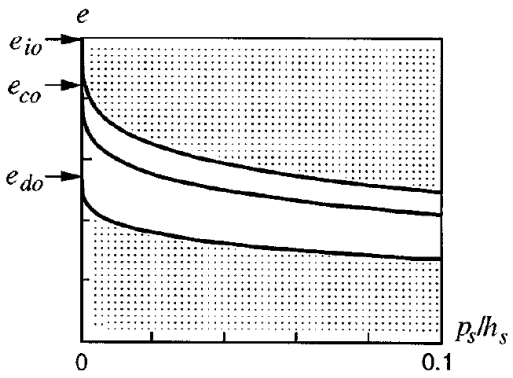

Figure 2.12- Linear scale of relationship between e_i, e_c, e_d and P_s, shaded areas are inadmissible states for the constitutive approach based on simple grain skeletons. (Herle & Gudehus, 1999)

e_{i0}, e_{c0}, e_{d0} are void ratio states at zero P_s and due to the impracticality to measure such values at zero confining pressure, estimations based on experimental results are commonly adopted. The definitions e_{i0}, e_{c0}, e_{d0} will as well be referred as e_i, e_c, e_d for the scope of this work

For the case of the minimum void ratio e_{do}, a good approximation was found with the minimum void ratio e_{min} measured from index tests such as the Japanese standard. The parameter e_{c0}

represents the critical void ratio and it was found that e_{c0} is approximately equal to the maximum void ratio e_{max}, which is obtained from index tests (Japanese standard).

The maximum void ratio at zero pressure e_{i0} is by far the most difficult one to determine experimentally, hence theoretical relationships have been proposed. A relationship of $e_{i0}/ e_{max} \approx 1.2$ was proposed for an ideal case of spherical grains and a ratio of $e_{i0}/ e_{max} \approx 1.3$ for angular grains. An assumption of $e_{i0}/ e_{max} \approx 1.25$ may be used for sub-angular-circular grains. (Herle & Gudehus, 1999)

The granulate hardness h_s is a parameter used as a reference pressure and takes into account the sensitivity of the grain skeleton to such pressures. The exponent **n** serves as the component that allows for non-proportional increases of the perceived stiffness when the pressure P_s is increased. These two parameters may obtained experimentally by tri-axial compression tests or Oedometer tests. Equation 13 and Equation 14 define h_s and **n**.

$$h_s = 3\,p_s\left(\frac{n e_p}{C_c}\right)^{1/n} \qquad \text{(Eq. 13)}$$

$$n = \frac{\ln(e_{p1}\,C_{c2}/e_{p2}\,C_{c1})}{\ln(p_{s2}/p_{s1})} \qquad \text{(Eq. 14)}$$

Figure 2.13 depicts the approach for estimating h_s and **n** by means of Oedometer test results. Two curve point are computed for a void ratio ***e*** and compression indexes C_c, and these points define the range of P_s in which the determined HP parameters are valid. The experimental range in which usually soil mode calibrations have been performed is usually around (20÷2000) kPa.

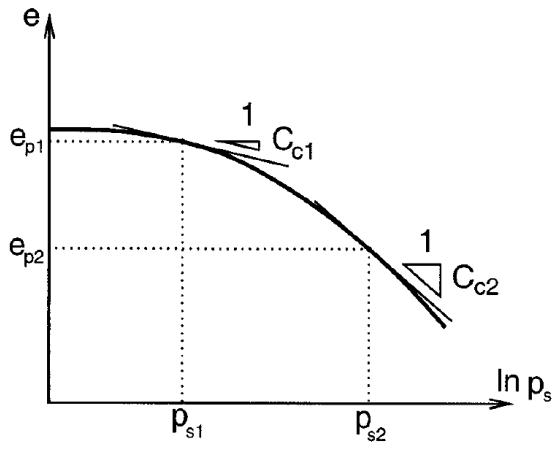

*Figure 2.13- Determination of **n** and h_s from experimental results over a particular stress range.* (Herle & Gudehus, 1999)

The following model parameter **a**, may expressed as the following equation:

$$a = \frac{\sqrt{3}(3 - \sin\varphi_c)}{2\sqrt{2}\sin\varphi_c} \qquad \text{(Eq. 15)}$$

Equation 15 brings an additional model parameter which is the critical state friction angle φ_{cv} and it may be obtained experimentally by measuring the angle of repose of the studied dry granular material. No standard procedure has yet being proposed for measuring this parameter.

The parameter α (Equation 11) is a factor that controls the dependency of peak friction angle on relative density D_r. α serves mainly as an exponent for a component of the general hypoplasticity formulation which controls the evolution of the soil behavior towards the critical state (Tsegaye, 2009). The way to determine α experimentally is by means of a drained tri-axial test as expressed in Equation 16:

$$\alpha = \frac{\ln\left(6\frac{(2+K_p)^2 + a^2K_p(K_p - 1 - \tan\psi)}{a(2+K_p)(5K_p-2)\sqrt{4+2(1+\tan\psi)}}\right)}{\ln\left(\frac{e-e_d}{e_c-e_d}\right)} \qquad \text{(Eq. 16)}$$

Equation 16 takes into account the previously defined void ratio states, as well as the initial void ratio ***e***. The peak ratio $K_p = \left(\frac{1+\sin(\varphi_p)}{1-\sin(\varphi_p)}\right)$ and the peak dilatancy ψ are as well involved in this formulation.

The parameter β (Equation 11) is a factor that controls the dependency of soil stiffness on relative density D_r. This parameter holds a significant importance for dense soils, if the initial void ratio ***e*** is substantially lower than the maximum void ratio e_{i0}. It may be determined by isotropic compression tests such as the tri-axial or Oedometer tests.

$$\beta = \frac{\ln\left[E\frac{3+a^2-f_{d0}a\sqrt{3}}{3+a^2-f_d a\sqrt{3}}\frac{e_i}{1+e_i}\frac{n}{h_s}\left(\frac{3p_s}{h_s}\right)^{n-1}\right]}{\ln\ (e_i/e)} \qquad \text{(Eq. 17)}$$

$$f_{d0} = \frac{e_{i0} - e_{d0}}{e_{c0} - e_{d0}} \qquad \text{(Eq. 18)}$$

$$f_d = \left(\frac{e - e_d}{e_c - e_d}\right)^{\alpha} \qquad \text{(Eq. 19)}$$

From Equation 17, several known parameters may be observed, as well as the elastic modulus **E** at a reference pressure P_s. The factor f_d (Equation 10) is also used for determining β . The parameter β is approximately equal to 1 for natural sands, and it lies usually in a range of (0÷2.5) for non-cohesive soils.

The 10 input parameters for the HP model stand as follows:

Critical state friction angle	φ_{cv}
Cohesion	p_t
Granulate hardness	h_s
Granulate exponent	n
Minimum void ratio	e_{d0}
Critical void ratio	e_{c0}
Maximum void ratio	e_{i0}
Factor alpha	α
Factor beta	β
Initial void ratio	e

One distinction between the hypoplasticity formulation (von Wolffersdorff) and EP models, is that the Mohr-coulomb failure criteria is not used. Instead, the Matsuoka-Nakai criteria is adopted, which super exceed the Mohr-Coulomb criteria in terms of numerical efficiency at non-corner points of its contour. This criteria matches the MC failure contour at the compression and extension points, while also slightly overestimating the MC at other points but at the same time smoothing the failure contour (von Wolffersdorff, 1996).

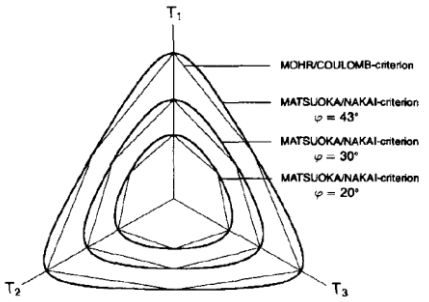

Figure 2.14- Matsuoka-Nakai and MC criteria compared at different peak friction angles. (von Wolffersdorff, 1996)

The HP model parameters are relatively difficult to be obtained from real test data. Nevertheless, this model provides a more or less unique set of parameters for a particular soil type at a chosen stress range. As the HP model depends on the soil's D_r at the initial condition, this makes it a great asset to simulate the SL-tank.

The adjusted set of parameters may be used with the only variation of the initial void ratio condition, which is highly sensitive and care must be taken in its use (Anaraki, 2008). The model excels in generating significant contractive behavior from the very start of the simulation which would continue in a progressive way until the CSL is reached. (Tsegaye, 2009)

2.2.5 Hypoplasticity model with intergranular strains (Niemuni's ISHP)

The HP formulation presented at section 2.2.4 was later enhanced into a model named the HP model with intergranular strains (ISHP) (Niemunis, 2002). This Extended version of the HP model provides the possibility to model small-strain stiffness effects in hypoplasticity. ISHP exhibits the main advantage over the standard HP when cyclic loads are considered by reducing the excessive accumulation of deformations predicted at small stress cycles (Niemunis, 2002). A poor prediction of hysteresis cycles is described as ratcheting or saw-tooth curves in stress-strain plots of cyclic behaviors. The hysteresis behavior could be defined as the deformation of an interface layer between particles and this deformation is dictated by the available recent history of strains. (Niemunis, 2002)

5 additional parameters are for the ISHP and they are of extreme difficulty to estimate by experimental results such as cyclic tri-axial tests. For most practical applications, parametric studies are used to calibrate the ISHP parameters. Due to their complexity, very limited data of calibrated sands are available. The input parameters stand as follows:

Factor for 180° reversal	m_R
Factor for 90° reversal	m_T
Elastic range size	R
Steepness degradation factor	β_R
Steepness degradation factor	χ

The parameter m_R controls the initial small-strain shear modulus when a 180° strain path reversal occurs. The parameter m_T controls specifically the initial shear modulus upon 90° strain path reversal. **R** may be seen as the size of the elastic range in which the integranular concept works. The parameters β_R and χ control the rate of degradation of the stiffness within this elastic range **R**. The following Figure 2.15 depicts most of the commented definitions.

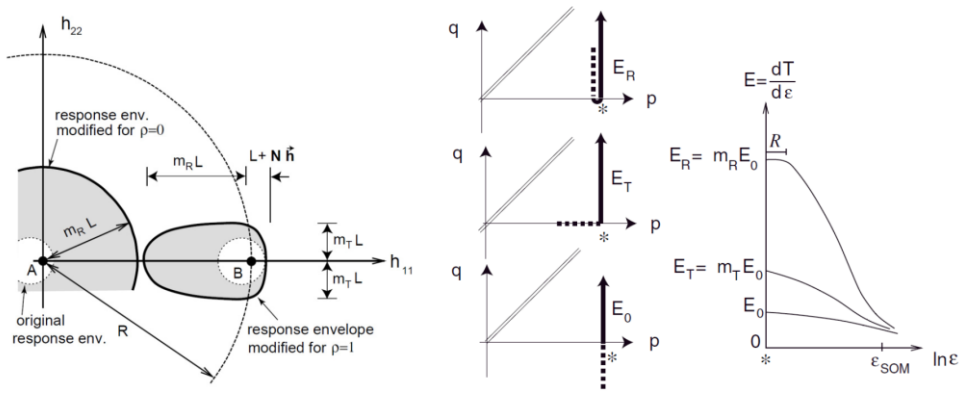

Figure 2.15.- Illustration of parameters m_R, m_T and R (Niemunis, 2002).

Comments regarding on how to estimate these parameters are not presented here, as it not part of the scope to experimentally determine such parameters. Some important guidelines

stated by Niemunis (2002) will be shown that are necessary for the intergranular formulation to be properly used within realistic bounds :

- For m_T and m_R it must be valid that: $m_R > m_T > 1$
- χ Should be within a range of 1÷10
- β_R should be within a range of 0÷1
- **R** is commonly adopted within the ranges of [1E-05÷1E-04]

The aforementioned parameters will be adopted from previous studies and also by calibration from best-fit undrained tri-axial tests. The guidelines commented before will be respected. Even though the scope of this research is the study of monotonic loads, the control of the small-strain stiffness and to take into account stress path reversal may be useful for this work.

Chapter 3: Experimental study

3.1 Geba sand characterization

The granular material that was chosen as the unique tested soil for this project is the Geba sand. This sand is mainly composed by a 99% of $Si0_2$, and a 1% of several chemical compound traces (Sibelco Europe, 2014).

From previous studies on Geba sand performed by Krapfenbaur (2016), some relevant properties that serve for characterizing this granular material will be used for this work as well. Table 3.1 shows the adopted averages of the mentioned soil characterization.

Table 3.1- General properties of Geba sand. (Krapfenbauer, 2016)

Gs [-]	C_u [-]	c_c [-]	D_{60} [mm]	D_{50} [mm]	D_{10} [mm]	Roundness [-]	e_{min} [-]	e_{max} [-]	Υ_{min} [kN/m³]	Υ_{max} [kN/m³]	K [m/s]	φ_{cv} [°]
2.67	1.50	1.20	0.123	0.118	0.084	0.77	0.64	1.07	12.9	16.3	4.2E-05	34

From the grain size distribution main properties, it may be stated that Geba sand is a material with high uniformity or well graded. Additionally, it's particle size is close to the lower boundary for classifying sands, which may be at a range between [0.063÷2.000]mm.

The specific gravity G_s for this material could be related to a value significantly close to the boundary between silts and fine sands. Some studies have shown that generally for sand Gs=2.63÷2.7 and for silts it may be around Gs=2.65÷2.7. (Mukhtar, n.d.)

Krapfenbaur (2016) reported that the adopted hydraulic conductivity *K* is an average that satisfactorily complies to a wide range of D_r= (0.3÷1.0). A pseudo-linear variation of *K* was seen from D_r=(0.0÷0.3). Within the loose state range, reported *K* were as high as 1.2E0-4 m/s.

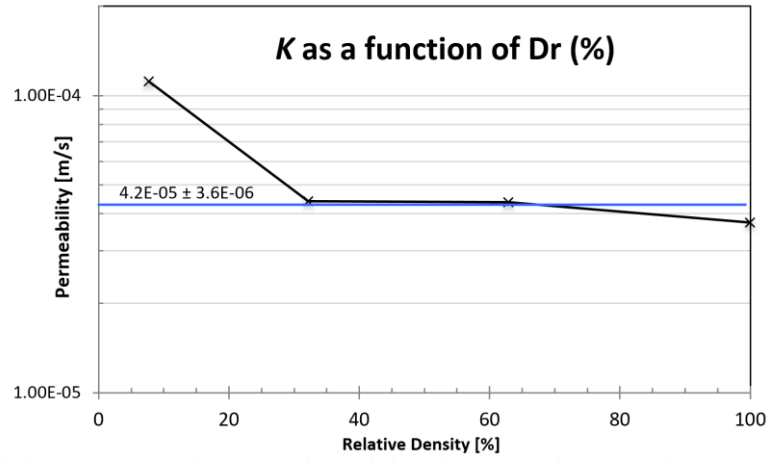

Figure 3.1.- Measurement of relationship between D_r and K for Geba sand. (Krapfenbauer, 2016)

The roundness factor of 0.77 relates to an assigned shape factor of a sample that would ideally represent the entire soil mass. An either automatic or manual analysis is carried for defining the particles geometry and obtaining this factor based on Equation 20 proposed for such method (Ferreria & Rasband, 2012).

Roundness: $\frac{4 \cdot \pi \cdot Area}{Perimeter^2}$ (Eq. 20)

The shape factor lies in between 0÷1, from which 1 is a circular shape and 0 is fully angular. Geba sand was stated to have a sub angular particle geometry, but leaning more towards the circular geometry spectrum. Having particles as circular as possible, provides a better homogenous mechanical response from the soil mass.

Masin (2017) measured for Geba sand the constant volume friction angle φ_{cv}=34, which is an stress and density independent state parameter. This parameter may be seen as a material property. Based on grain size distribution, volumetric properties and $\varphi_{cv,}$ Geba sand holds a strong resemblance to some well-known sands such as the Toyoura sand and the Karlsruhe fine sand.

Soil heterogeneity is an issue when dealing element tests or complex procedures such as the SL-tank. Having homogenous conditions will enhance the test's reproducibility potential as well as more accurate results. Regardless of the type of test, having a controlled environment is usually a key factor for achieving satisfactory results. From all the commented soil properties, Geba sand is a viable option for having improved control in test conditions.

3.2 Physical model characterization

3.2.1 Static Liquefaction tank

The SL-tank serves as the main framework in which to analyze the numerical simulations performed in this research project. This physical model has fixed or limited conditions for simulating the static liquefaction behavior that may occur at a real-scale submarine slope.

The SL-tank has external dimensions of height, length and width of respectively of 5,2 and 2 meters. The sidewalls (5m) are made of transparent hardened glass that allow a reduced lateral friction. The back walls and floor are made of steel. The SL-tank is supported in such a way that no external forces will affect the performed tests. The internal measurements of the SL-tank's sidewall is equal to 4.8m long (Figure 3.2). The bottom contact surface inside of the SL-tank (in contact with the sand layer) is made of a synthetic grid combined with a geotextile, which has a contact surface rough enough to not easily allow soil displacements.

The slope failure mechanism is triggered by employing a tilting mechanism around the axis shown in Figure 3.2. The initially resting sand layer is accelerated by a tilting mechanism at a

prescribed tilting rate until failure is reached. The process to prepare the sample is known as fluidization, in which pressurized water is applied through a highly porous filter layer located at the bottom of the SL-tank. As the granular soil is in a suspended state by the fluidization process, the particles reach very loose states after having resettled. Recording measurement tapes labeled as E1-E6 for axis A-A' and W1-W6 for axis B-B' were used for estimating the sand's D_r inside the SL-tank before testing it (de Jager, 2015).

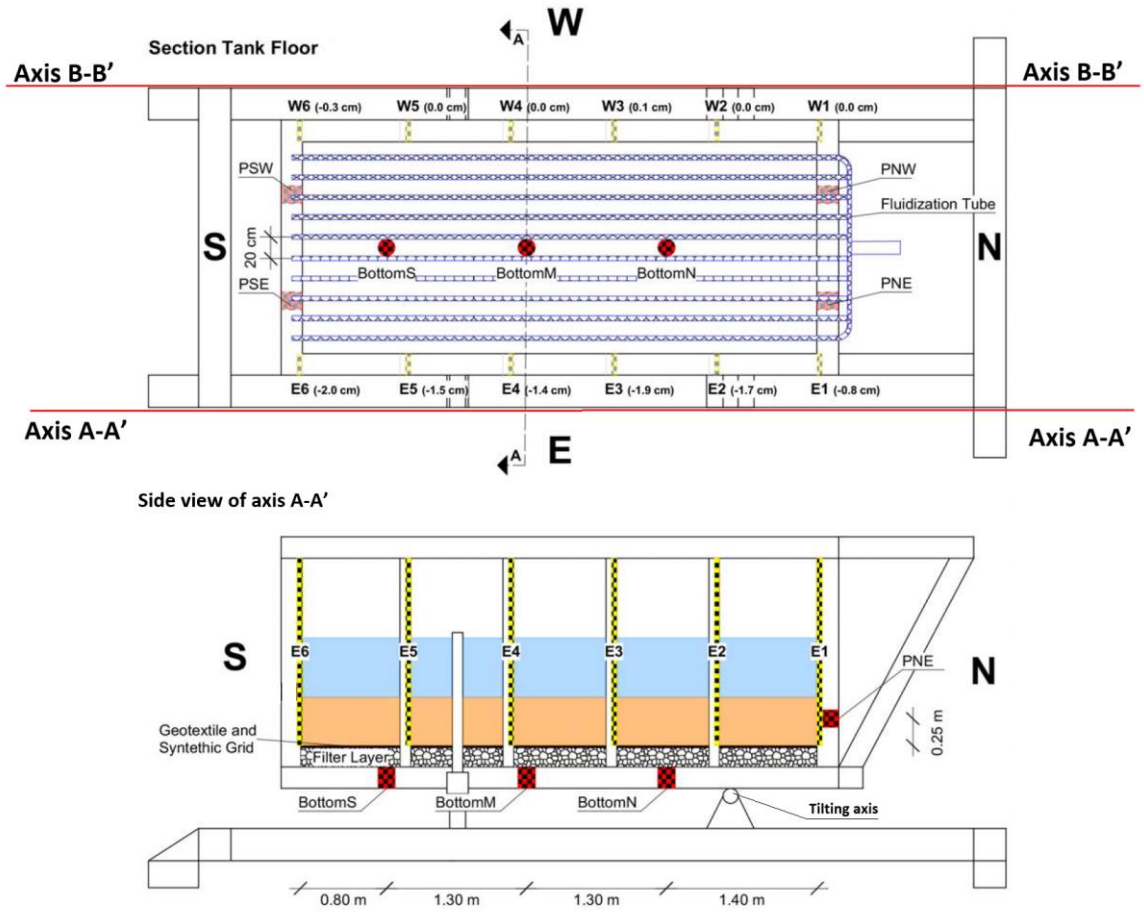

Figure 3.2- Longitudinal and transversal cross section of SL-tank. (Krapfenbauer, 2016)

Because of either safety or limitations of the current facility, fixed testing conditions were established. The tilting rate, maximum tilting angle, soil layer height and the density state (D_r) of the tested sand are the main prescribed test conditions.

The tilting rate options which were available as an input for the test are 0.11, 0.03 and 0.01 °/s (Krapfenbauer, 2016) . Currently, a sand layer of 0.5m was used for testing with the Static liquefaction tank.

Figure 3.2 presents the locations where Pore water pressure sensors are currently available for recordings. The data of 4 sensors were used, namely BottomS, BottomM, BottomN, and PNE. When referring to the SL-tank test's behavior, the terms Southern and Northern sides will be

used in this work. BottomS is the furthest sensor location at the Southern section, and PNE is the furthest at the northern side.

Eastern and Western sides will not be used as any reference for this research, since a simple approach of plane strain through the axis A-A' was adopted for the performed numerical simulations.

3.2.2 Experimental results

Figure 3.3 depicts the excess P_w evolution from an experimental SL-tank test executed with Geba sand at a tilting rate of 0.11 °/s.

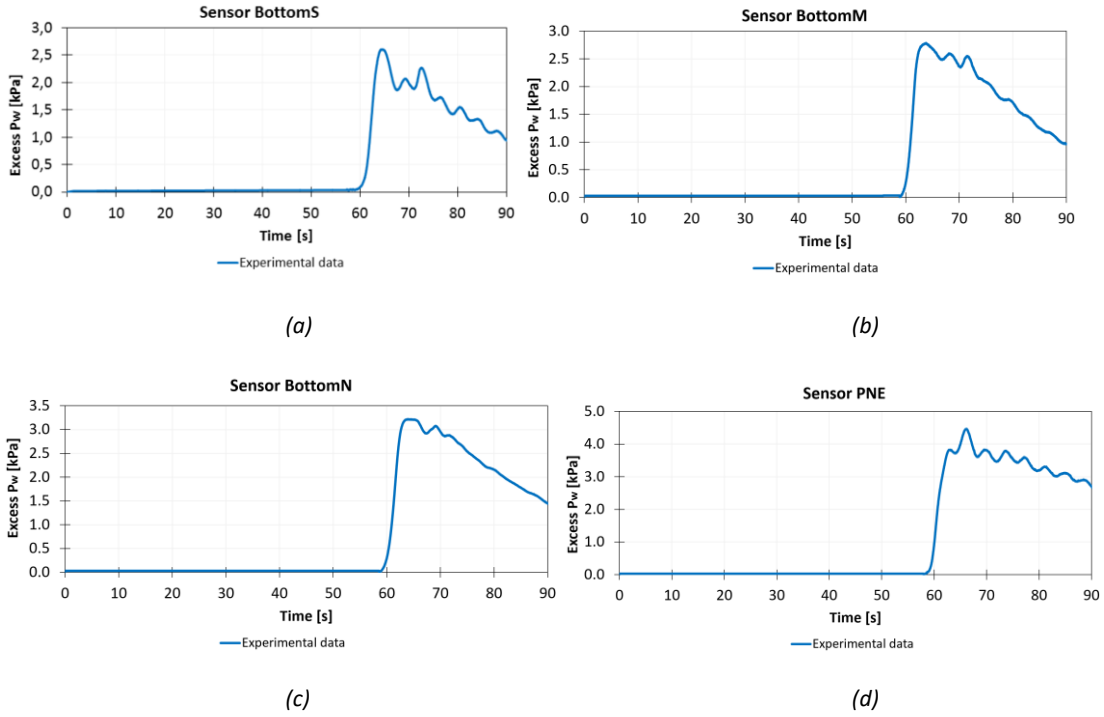

*Figure 3.3-Excess P_w evolution over time for sensors BottomS **(a)**, BottomM **(b)**, BottomN **(c)** and PNE **(d)**.*

Results of Figure 3.3 show zero excess P_w until a tilting angle of circa 6.5°, after approximately 60s have passed. It may be stated that drained conditions are occuring for the most part of the test until a sudden trigger allows a significant development of excess P_w. Failure of the soil layer occurs at the moment in which recorded peaks as high as 4.5kPa (Figure 3.3b) of excess P_w may be observed. The peak excess Pw occur approximately after 63s from the test's start.

The following secuence of images (Figure 3.4) depict the flow pattern of the failure mechanism for a test of 90s at a tilting rate of 0.11 °/s:

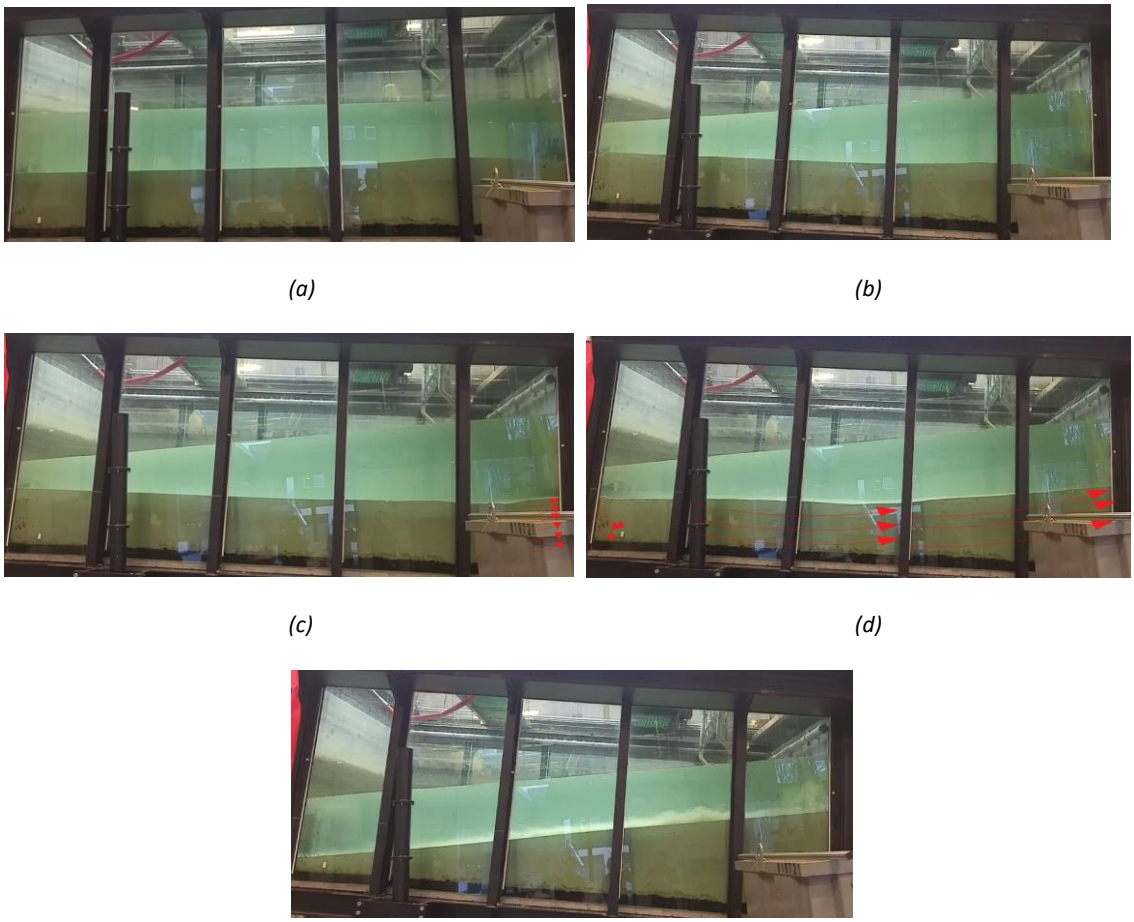

(a) *(b)*

(c) *(d)*

(e)

Figure 3.4- ***(a)*** *Initial state of test.* ***(b)*** *1s before failure (no visible deformations compared to initial state).* ***(c)*** *At failure (noticeable deformations develop at the northen section of the SL-tank).* ***(d)*** *5 seconds after failure (flow failure keeps propagating in the shown pattern).* ***(e)*** *20 seconds after failure (No more noticeable deformations may be seen).*

From the observations of the flow mechanism, it may be reported that no visible failure plane is seen before liquefaction is triggered. The instantaneous collapse of the sand layer may have potentially initiated at the Northern side and it further propagates towards the Southern side. This may be supported by the higher excess Pw at the Northern side compared to the southern area, as well as an earlier trigger of peak excess Pw at the Northern section of the SL-tank (Krapfenbauer, 2016).

3.2.3 In-Situ test conditions

Regarding the relative Density D_r:

The initial soil D_r at the SL-tank test was narrowed to a reliable and reproducible range depending on the degree of fluidization used during the sample preparation. A consistent relative density between 0.27÷0.34 was obtained for a loose sample preparation from a proposed method by de Jager (2015). This approach relied on measuring heights of the sand layer at several fixed locations (Figure 3.2) and relating them to the existing soil mass, volumetric dimensions and specific gravity (see Appendix A). The upper boundary D_r at the densest configuration after fluidization is a value of approximately D_r=0.60. A representative value (D_r=0.30) was adopted by the author to represent D_r at its loosest possible state.

The Geba sand's saturated unit weight Υ_{sat} at a D_r=0.30 may be obtained from:

$$\gamma_{sat} = \gamma_w \cdot \frac{e+G_s}{e+1} \qquad \text{(Eq. 21)}$$

From which the void ratio ***e*** at a D_r=0.30 is calculated as 0.94.

Regarding the vertical stress level:

During the current stages of the research project involving the Static liquefaction tank, experimental tests have been performed with a Geba sand layer of a height equal to 0.5m.By considering an effective vertical stresses σ'_v as a reference of stress level at the initial test conditions, this yields the following result:

$\sigma'_v = (\Upsilon_{sat} - \Upsilon_w) \cdot$ (Layer height)= 4 kPa

The stress range (0÷4)kPa over the soil layer is considered a very low stress range. Considering 4kPa as a peak effective vertical stress in the SL-tank, the observed excess P_w at some locations exceed 4kPa, which would imply an effective stress of zero at critical zones of the soil layer.

Regarding the initial field stress conditions (K_o):

the lateral earth pressure coefficient at rest K_o may be usually estimated by an empirical approach such as the one proposed by Jaky (1944) or through in-situ tests by performing a pressuremeter test. This correlation relies on the adopted friction angle through Equation 22 (Jaky, 1944).

$K_o = 1 - \sin(\varphi)$ (Eq. 22)

If φ_{cv} is used for this computation, then approximately a Ko=0.44 is obtained. But if a significantly higher φ is used (i.e. φ=52°) , then the obtained K_o would be far from realistic, obtaining K_o values such as K_o=0.21.

Due to very low effective stresses found at the SL-tank, results of peak friction angles φ_p and residual friction angles φ_r significantly differed from φ_{cv} (section 4.2.4). A series of pressuremeter tests performed with Hostun sand were used to verify a reasonable K_o value (Gay, Boutonnier, Flavigny, *et al.*, 2003). One of these particular pressuremeter tests was sampled at a relative density D_r=0.30 and it yielded a K_o=0.40 (Gay, Boutonnier, Flavigny, *et al.*, 2003). From this result, it was chosen do adopted the K_o=0.44 as a fixed condition for the experimental tests of the SL-tank, which is based on Equation 22 and using the φ_{cv} corresponding to Geba sand.

Chapter 4: Element tests

Two types of experimental element tests were performed by the author, the Direct Shear (DS) and Oedometer (OED) tests. Additionally, consolidated-drained tri-axial (CDTX) results performed with Geba sand by Noriega (2015) were employed for the scope of this project. The aforementioned tests were performed in low stress ranges which could be attributed to confining stresses of approximately 1÷50 kPa.

For the specific case of the Hypoplasticity framework, the relevant results from Masin (2017) of oedometric tests at a stress range [40÷4000kPa] were used as a key reference. Different and non-standardized sample preparations for DS and OED tests were performed by the author.

4.1 Oedometer test

4.1.1 General aspects

The purpose of realizing Oedometer tests was to obtain stiffness parameters of the Geba sand, particularly the tangent Oedometer stiffness modulus E_{oed}, and the unloading-reloading stiffness E_{ur}.

A non-standardized sampling method was performed at very low stresses σ_v= (1÷5)kPa, and up to medium-low stresses of 100kPa. This approach is subdivided in two sample preparations that were chosen to compare their effectiveness in this application, namely the dry and wet pluviation.

The results of both dry and wet samples were presented in two batches which follow different test setups regarding the loading-unloading processes. The first batch of tested samples was performed solely in a very narrow stress range of (1÷5) kPa. A total of 12 loading steps with increments of approximately 0.3kPa per loading phase were performed for the first batch.

The second batch aimed at a low-medium stress range of (5÷100) kPa with a total of 18 loading steps. Initially, the loading increments started with 1kPa but it was multiplied by a factor of 2 after 4 successive loading steps have been performed.

The chosen OED test results do not include unloading-reloading phases due to problems with the test procedure. The results and comments regarding E_{ur} are presented in further sections.

Both types of samples preparation were carried with the same equipment, being a standard Oedometer and a single LVDT implemented for deformation readings per chosen intervals of time. The mentioned equipment is depicted in the Figure 4.1. A ring mold of a height of 2.1cm was used for all the tests. For filling-in the mold with sand, a funnel was used in a clockwise pattern. A set of weights with values as low as 100gr were used through the loading/unloading

stages of the tests, as well as heavier weights for reaching peak vertical stresses up to 100kPa. Particularly for the dry pluviation method, a circular metallic cap was used (Figure 4.1b) as part of this non-standardized approach.

One aspect of the custom approach for these Oedometer tests was that constant load steps were used, contrary to common practice of increasing the load by factors of 2 and higher per consecutive phase. This is mainly because of the narrow stress range that is studied and also provided the low compressibility of such a granular material.

(a) *(b)*

Figure 4.1 ***(a)*** *Oedometer test equipment.* ***(b)*** *Mold ring, ring base and circular metallic cap.*

The tested sand's expected time for consolidation per loading phase is considerably smaller in comparison to cohesive soils. A nearly instantaneous settlement was a great advantage in terms of efficiency to perform a significant number of tests and assess the reproducibility and quality of the results. Sufficient time was allowed for the recordings to no longer show significant increases in deformation, which through trial and error was established as approximately 180 seconds per loading/unloading phase.

It was of significant importance to obtain results with a D_r as close as possible to the adopted ones in the SL-tank, which is around D_r=0.30. After performing several trials with both the dry and wet approach, it was found out that achieving a D_r <0.40 was challenging and that little to no precision was achieved. Due to the low reproducibility of a D_r=0.30, a different value was adopted. A D_r=0.40 was successfully obtained over a wide number of tests, regardless of the preparation approach.

A main inconvenient during sample preparation was the high sensitivity and variation of recordings when handling very low loads. It was necessary to ensure the least disturbance while loading-unloading the samples. When handling weights as low as 100gr, any additional exerted force when placing the loads in the weight hanger system would significantly alter the recordings, especially the initial ones.

Even though unloading-reloading paths were performed for a few tests, it was demanding to obtain accurate or even reproducible results from these paths. Notable discrepancy of the unloading-reloading response between different tests, deemed it inappropriate to study at small stress ranges.

4.1.2 Dry pluviation method

Sand was first poured inside the ring mold in a clockwise and spiral pattern with the use of a funnel. Particular attention was needed in maintaining a close distance between the funnel and the poured sand layer. After reaching the total ring height, a circular cap was used by carefully exerting mild pounds over the sand's surface. After trial and error, it was found that a total of 3 pounds were necessary for achieving the desired D_r. The aforementioned method enabled a preparation of D_r=0.40 with a margin of error of ±0.05.

Placing the sample and carefully zeroing the Oedometer with the top cap of the equipment was relatively easy as it was possible to always observe the contact between the sand and the top cap. One of the main concerns with this approach was the potential of having packages of void, even though mild compactions were used to minimize this potential issue.

If no compaction was used after filling-in the ring mold, the calculated relative densities from a series of tests would hardly be the same. This is due to the generation of void packages, which means that achieving consistent results of D_r<0.30 is of considerable difficulty. This characteristic was the main shortcoming of the dry pluviation method. Special care for filling-in the ring mold was needed, as the minimum loss of sand significantly affects the estimated D_r.

4.1.3 Wet Pluviation method

The ring base was filled-in with enough water, after which the sand is poured in as close as possible to the water's surface and in a clockwise-spiral pattern. The obtained relative density was within the limits of D_r=0.40 with a margin of error of ±0.05.

This method was significantly faster to perform and less prone to error at sample preparation, when compared to the dry pluviation approach.

The wet pluviation showed a significantly better performance in terms of efficiency but it's test procedure had one main shortcoming. For the case of dry pluviation, it was possible to observe when the top load cap was in contact while zeroing the equipment but with the wet pluviation it was not possible to fully see the initial contact. If no full contact was prepared, then the initial recording would under predict the actual displacement that should occur, while if the contact was overexerted then exaggerated deformations would be recorded.

4.1.4 Results and discussions of the Oedometer test

Table 4.1 and Table 4.2 present the Oedometric stiffness results from the two mentioned test batches, which both have dry and wet preparations.

Table 4.1- Oedometer stiffness of Geba sand at stress range of [1÷5] kPa.

	E_{oed} [kPa] at very low stress range				
Stress range [kPa]	1÷1.5	1.5÷3.0	3.0÷5.0	D_r [-]	State
D1T1	650	1300	1950	0.44	Dry
D2T1	400	700	1000	0.42	Saturated
D3T1	650	1350	2300	0.47	Saturated
D4T1	200	500	750	0.42	Saturated
D4T2	100	300	800	0.38	Saturated
D4T3	350	500	800	0.40	Saturated
Adopted	**500**	**750**	**1000**	**0.40**	**Saturated**

Table 4.2- Oedometer stiffness of Geba sand at stress range of [5÷100] kPa.

		E_{oed} [kPa] at medium-low stress range				
Stress range [kPa]	5÷15	15÷35	35÷50	50÷100	D_r [-]	State
D5T2	1500	7500	10000	-	0.45	Saturated
D5T4	1500	8000	12000	-	0.40	Saturated
D5T1	2000	6000	10000	15000	0.41	Saturated
D5T5	2500	7500	12000	-	0.45	Dry
D5T6	2000	5000	7500	-	0.37	Dry
Adopted	**2000**	**7000**	**10000**	**15000**	**0.40**	**Saturated**

The results were solely expressed in terms of the E_{oed}, since E_{ur} was difficult to assess from the tested samples. As an example of this problem, a typical test result with unloading-reloading stages is shown in Figure 4.2. It may be seen (Figure 4.2) that the recorded unloading stiffness is not similar to the reloading counterpart by a significant amount. This issue may be attributed to the small load increments that were used, which generated significant equipment sensitivity. Even for Oedometer tests with unloading-reloading (UR) paths performed at higher stress levels of approximately 50kPa, the same issue was observed.

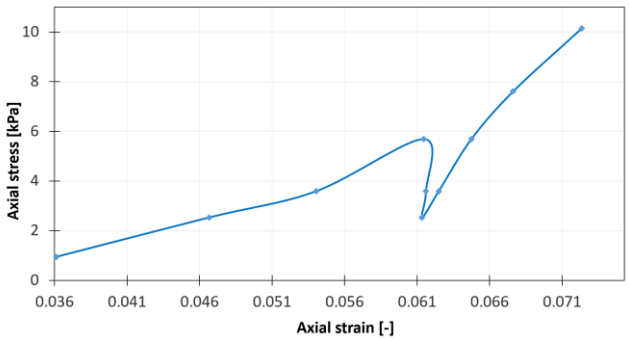

Figure 4.2- Results from a representative OED test with unloading-reloading stages at [1÷10] kPa.

Even though the estimation of E_{ur} was challenging for very low stress ranges, a representative factor for assessing E_{ur} was identified. Judging from experimental results, Geba sand showed a rough correlation that approximates the unloading-reloading stiffness by multiplying the Oedometer stiffness E_{oed} by a factor that was found to be between around [4÷7]. From previous studies performed by Schanz and Vermeer (1998), it was stated that for sands a rough correlation of $E_{ur} \approx [4 \div 5] \cdot E_{oed}$ may be used. By relating this correlation with the obtained results, a relation of $E_{ur}=4 \cdot E_{oed}$ was adopted for this research project.

Geba sand shows a relatively flexible response (Table 4.2) compared to medium-loose sands that usually have a stiffness (p_{ref}=100 kPa) around E_{50}= (30÷50) kPa. An expression $E_{oed} \approx [1 \div 1.5] \cdot E_{50}$ may be applied for normally consolidated sands assumption (Schanz & Vermeer, 1998). For simplicity, $E_{oed} \approx 1 \cdot E_{50}$ will be adopted, since these results as well showed satisfactory matching with constitutive model calibrations (Chapter 5) . The stiffness E_{50} from Geba sand at CDTX tests also showed strong similarities to this adopted assumption (Section 4.3).

4.2 Direct shear test

4.2.1 General aspects

Two sample preparation procedures were performed for the DS test, namely a medium-loose preparation and a medium-dense method. The medium-loose approach aimed for achieving relative densities at a range of D_r=[0÷0.3],while the medium-dense method had a target density of D_r=[0.3÷0.6] . Both sample preparations were non-standardized and elaborated mainly for the purpose of achieving a reproducible range of relative density.

The main challenge that affected the DS results was the approach in which the acting normal load was applied to the sand sample. The target stress range for these tests was within vertical stresses of σ_v=[1÷10] kPa, having a particular interest in the results that were closer to a D_r=0.3. It was necessary to load the sample directly on top of the load cap (Figure 4.3b) with light-weights, instead of using the pulley jockey system for placing loads (The light-weights didn't fit the jockey system). By applying the load on top of the cap, this generated an undesired tilting effect, which more likely distributed the vertical loads in a significantly uneven configuration. This tilting effect also occurred when using higher loads applied in the pulley jockey system but at a lesser extent.

The obtained tests that exhibit the lesser degree of cap tilting and more appropriate D_r values were chosen. Two batches of test results were executed to estimate the strength parameters of peak friction angle φ_p, residual friction angle φ_r, and peak dilatancy angle ψ. The first batch is named ''medium-loose DS results'' at D_r =[0÷0.3] and vertical stress range between (1÷10) kPa. The second batch of results named ''medium-dense DS results'' was performed at the medium-high range of D_r=[0.3÷0.6] and at very low stress of (1÷5)kPa.

The medium-loose DS results focused in capturing similar conditions to the ones in the SL-tank. The medium-dense DS results served as an additional means to further study how the mobilization of φ_p, φ_r, and ψ s at low stress at medium-dense conditions

The sheared samples were tested until reaching deformations that were relatable to horizontal displacements of approximately 10mm. Figure 4.3 depicts the equipment used for testing the soil.

(a) *(b)*

Figure 4.3- ***(a)*** *Direct shear equipment.* ***(b)*** *Shear box mold, load cap and wooden cap.*

4.2.2 Medium-loose sample preparation

The medium-loose method followed a similar procedure as the one performed for obtaining a maximum void ratio if the Japanese standard was used. The total height of the shear box mold (31mm) was filled-in with sand using a funnel as close as possible of the poured sand. A Clock-wise pluviation was performed, ensuring a uniform filling with no compaction.

The main issue in the sample preparation with a shear box mold is the high inaccuracy and low reproducibility of target densities. This lack of precision was due to the joints and small cavities of the shear mold. Estimations of soil mass inside the box mold had a significantly uncertainty of approximately ±0.10 in terms of D_r. The approximate range of D_r obtained from this preparation was of $D_r = [0.10 \pm 0.10]$.

4.2.3 Medium-dense sample preparation

For this approach, a procedure similar to the Japanese standard was used. The soil was poured in the shear box mold in two layers, from which between each layer a total of 5 mild compactions per layer were performed with a wooden cap. Through trial and error by adopting this approach, a relative density was obtained in a rough range of approximately $D_r = [0.50 \pm 0.10]$.

4.2.4 Results and discussion of Direct shear test

Table 4.3 and Table 4.4 depict the obtained strength parameters from these tests. At the medium-loose results (Table 4.3), some tests with a D_r=0.45 were used to calculate the required shear strength parameters

Table 4.3- Medium-loose shear strength parameters of Geba sand at stress range of [1÷10] kPa.

Shear strength results from medium-loose batch					
Sample #	σ_v [kPa]	D_r [-]	φ_p [°]	φ_r [°]	Ψ [°]
D6T1	9.5	0.05			
D6T2	10	0.10			
D6T3	6.5	0.05	48	38	13
D6T4	2.5	0.45			
D6T5	5	0.50			
D6T6	8.5	0.45			

Table 4.4 – Medium-dense shear strength parameters of Geba sand at stress range of [1÷5] kPa.

Shear strength results from medium-dense batch					
Sample #	σ_v [kPa]	D_r [-]	φ_p [°]	φ_r [°]	Ψ [°]
D7T1	2	0.45			
D7T2	3	0.5			
D7T3	3	0.7	52	41	19
D7T4	4.5	0.6			
D7T5	1.5	0.6			
D7T6	2	0.6			

Figure 4.4 shows some of the test results from Table 4.3 and Table 4.4, from which linear trends may be observed as function of applied normal and shear stresses. The trends were close enough to the axis origin (0,0) as no cohesion may be attributed to this clean and uniform sand.

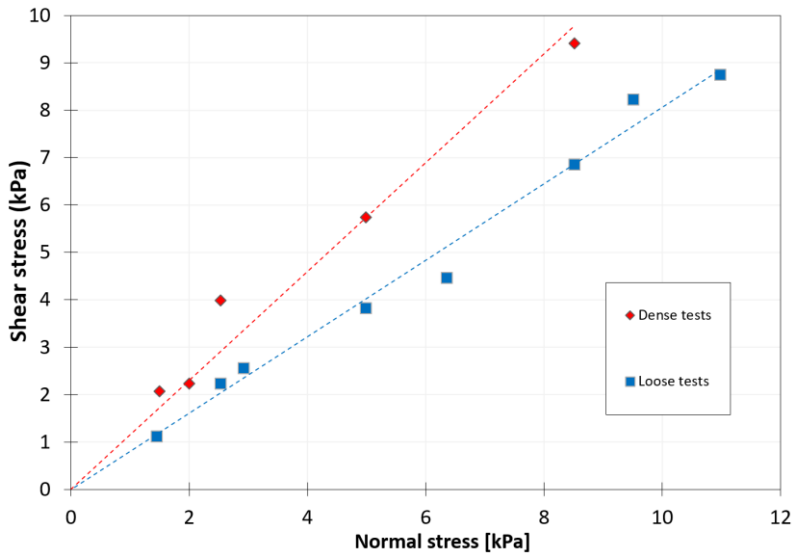

Figure 4.4- Linear approximation from DS tested samples for φ_p , φ_r determination at (1÷10) kPa.

Regarding the loose test results of Figure 4.4, even though results corresponding to D_r=0.05 are used for a linear trend, the estimated φ_r is significantly higher than φ_{cs}=34°. The mobilized shear strains of approximately ζ_{xy}=15%, were not high enough to fully reach the critical state at $\varphi_r=\varphi_{cs}$= 34°. This outcome was a limitation of testing Geba sand at low stress levels.

The best-fit linear approximation of Figure 4.4 could be further enhanced by assuming that an apparent cohesion of 0.5kPa is exhibit at zero normal stresses. As commented by Ponce and Bell (1971) for very low stress, the significant increase in shear strength may be attributed due to an apparent cohesion. Even though Geba sand has virtually no silty-clayey content and cohesion is zero at medium-high stress levels (P_{ref}>100 kPa), there is a possibility for a cohesive force to be acting at stresses around [1÷10] kPa . With the supporting test data of Ponce and Bell (1971) and the reported results from this work, this apparent cohesion may be occurring at low stress conditions but more research should be carried on this topic to confirm it.

At a P_{ref}=100 kPa, a range of φ_p=[35÷40]° is usually depicted for medium-dense sands, and may as well be the case for Geba sand under similar density states. If φ_p=37.5° is used as reference for a P_{ref}=100 kPa and by comparing it to φ_p=52°(P_{ref}=2kPa), then a difference of a larger φ_p in a factor of 1.4 times may be observed. Substantial variations of φ_p were reported by comparing Table 4.3 and Table 4.4, evidencing the incidence of lower stress levels in shear strength.

The estimated Ψ based on the recorded vertical and horizontal deformations from tests exhibited a high variation between the medium-loose batch and the medium-dense batch. Both Ψ values, namely 12° and 18° are significantly high dilatancy angles, if compared to Ψ as low as [0÷5] degrees for fine sands at P_{ref}=100 kPa (Bolton, 1986).

An observation from these unusual results is that they seem to not violate the conventional empirical formulations that have been usually adopted for granular soils, proposed by Bolton (1986). These correlations were tested over a wide range of sands, from which reasonable results have been obtained for sands at medium-high stress levels (P_{ref}> 100 kPa) of previous case studies (Bolton, 1986).

If the correlations proposed by Bolton (1986) and Rowe (1962) are used for the Geba sand at the calculated φ_p results and taking into account φ_{cv} =34°, then the following results are observed:

$[\varphi_p= \varphi_{cv} + \Psi\cdot 0.8]$ (Bolton, 1986) (Eq. 21)

$[\varphi_p= \varphi_{cv} + \Psi]$ (Rowe, 1962) (Eq. 22)

Table 4.5 Shear strength parameters comparison from empirical correlations and real tests.

φ_p [°]	Ψ (Bolton) [°]	Ψ (Rowe) [°]	Ψ (DS test) [°]
48	17.5	14	13
52	22.5	18	19

From these results, it was observed how the stress dependency in the small stress range can affect the shear strength response of a sand. This phenomenon is re-stated in the following Section 4.3 involving tri-axial test results of Geba sand at low stress ranges of [25÷50] kPa. Additionally, the dilatancy of sands may be reasonably estimated from empirical correlations that were tested at medium-high stress levels.

4.3 Tri-axial test

Consolidated-drained (CD) tri-axial tests performed on Geba sand at low stress levels [25÷100] kPa (Table 4.6) were revisited for this study (Noriega, 2015). The peak friction angle ϕ_p and secant Elastic modulus E_{50} were estimated. Figure 4.5 illustrates the two test results that were used to obtain the results from Table 4.6.

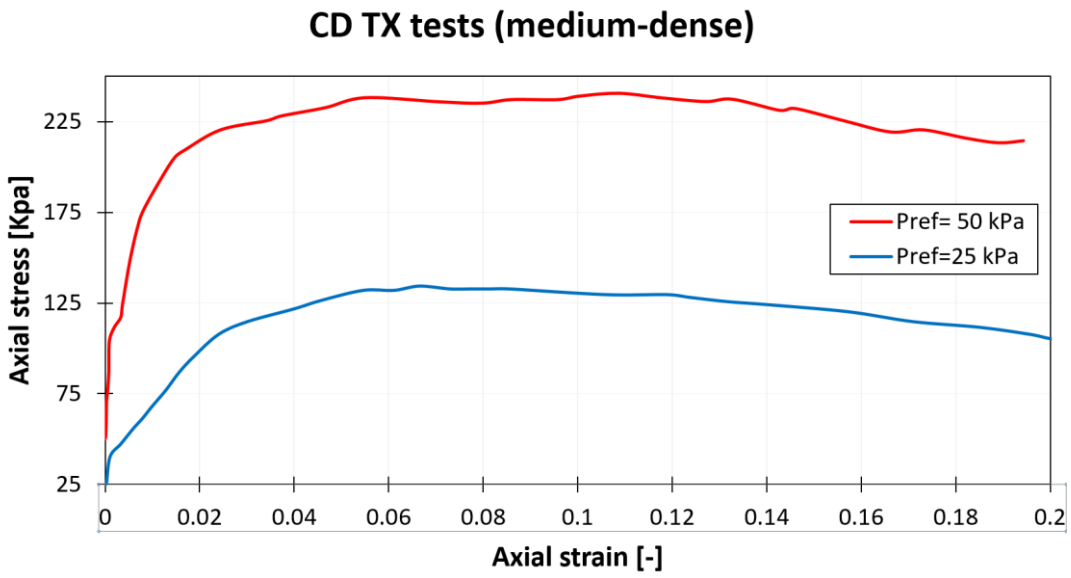

Figure 4.5- Consolidated and drained tri-axial tests performed at medium-dense D_r.

Table 4.6- Estimated stiffness and shear strength parameters of the available CDTX tests.

TXCD #	P_{ref} [kPa]	D_r [-]	φ_p [°]	E_{50} [kPa]
1	25	0.48	43	4500
2	50	0.58	41	20000

From these results, the previous estimations of E_{50} and φ_p (From DS and OED tests) can be related to the ones obtained at table 4.6. The difference in φ_p may be seen from these CDTX results, as a lower P_{ref}=25 kPa yielded a higher φ_p than at P_{ref}=50 kPa. The D_r from the two CDTX results show that regardless if the sample was slightly denser or looser, a lower P_{ref} has an stronger impact in the shear strength behavior. For cases in which the D_r is low enough (i.e. D_r=[0÷0.3]), it will have a significant impact in φ_p, as well as in the developed Ψ.

Based on the CDTX results, an extrapolated power trend may be constructed to estimate the shear strength development in terms of confining stress (Figure 4.6). The main characteristic of this trend is the strong response of the mobilized shear strength at stress levels lower than 25kPa, as the high non-linearity is observed.

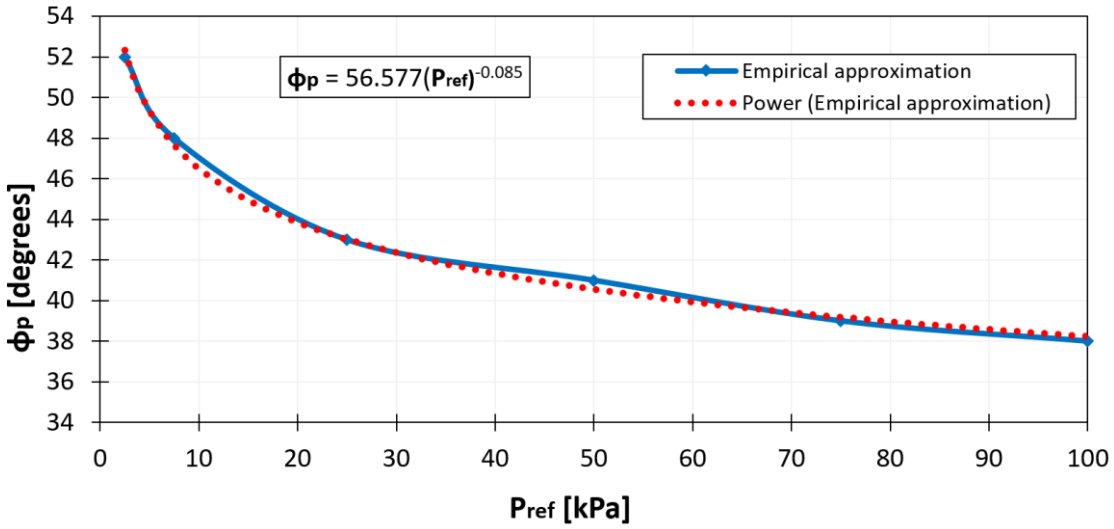

Figure 4.6.- Geba sand shear strength ϕ_p evolution in terms of confining stress P_{ref} at a D_r=(0.3÷0.6).

Regarding the estimated secant E_{50} from these TXCD tests, they may be related satisfactorily to the adopted values for E_{oed}. The assumption of $E_{oed} \approx E_{50}$ shows a strong correlation for this case, with slight differences that may be attributed to variations in D_r of 25% between the OED and the TXCD tests.

Chapter 5: Parameter determination and calibration

The parameter determination was initially realized by means of theoretical expressions or empirical approaches commented in Chapter 2 and Chapter 4. After obtaining these preliminary set of parameters, element test (DS, OED) simulations in PLAXIS were implemented. These simulations were compared to experimental test results done by the author. A best-fit of stress-strain curves was done between experimental and numerical results, from which updated sets of parameters were obtained (calibration). The use of DS and OED tests are the main basis of parameter calibration. The calibrated models are presented as well in terms of CUTX effective stress paths p'-q to show their potential in terms of liquefaction behavior.

Two sets of parameters are presented per each model. The first set is denoted as ''pre-calibrated'', which were estimated based on experimental results, empirical/theoretical formulations or correlations. The second set of parameters denoted as ''calibrated'', were obtained through best-fit curve refinement of the OED and DS simulations. The calibrated results were focused in being best-fitted as much as possible to the DS simulations, while still having acceptable calibrations from the Oedometer simulations.

The selected direct shear test for calibration was done at a vertical stress of 3kPa and a D_r=0.40. Approximately a shear strain of 15% was attained from this test, which was based on a back-calculation of the horizontal displacements.

The chosen Oedometer test for calibration, was tested at a vertical stress range of [1÷5] kPa, from which a wet pluviation was performed and thus obtaining a D_r=0.40.

5.1 MC parameter determination & calibration

The preliminary set of MC parameters was obtained directly from the shear strength results (section 4.2.4) and OED test results (section 4.1.4). The unique E modulus was taken as 0.75 times the E_{oed}, while φ and ψ were defined as reported in section 4.2.4. Cohesion was assumed as zero, provided that this is a clean sand. The Poisson's ratio was assumed as 0.30, which is an usual value adopted for sands. The usual range for *v* is (0.2÷0.35) for loose to medium sands.

The following Table 5.1 and Table 5.2 depict respectively the preliminary and calibrated sets of parameters for MC. It must be noted that the calibrated stiffness E complies with the commented empirical correlation of $E_{oed} \approx [1 \div 1.5] \cdot E_{50}$. Figure 5.1 and Figure 5.2 show the comparison between the 2 sets of parameters and the experimental results.

Table 5.1 MC determined parameters prior to calibration.

MC parameters pre-calibrated		
Elastic modulus [kPa]	E	500
Poisson's ratio [-]	*v*	0.3
Cohesion [kPa]	c	0
Friction angle [°]	φ	48
Dilatancy angle [°]	ψ	13

Table 5.2 MC parameters after calibration.

MC parameters calibrated		
Elastic modulus [kPa]	E	700
Poisson's ratio [-]	*v*	0.2
Cohesion [kPa]	c	0
Friction angle [°]	φ	46.5
Dilatancy angle [°]	ψ	12

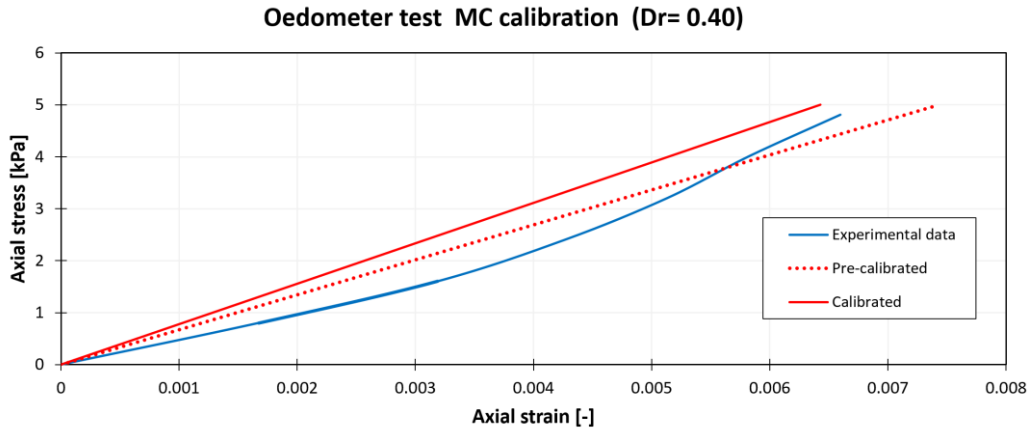

Figure 5.1 Oedometer test MC simulations and experimental results comparison.

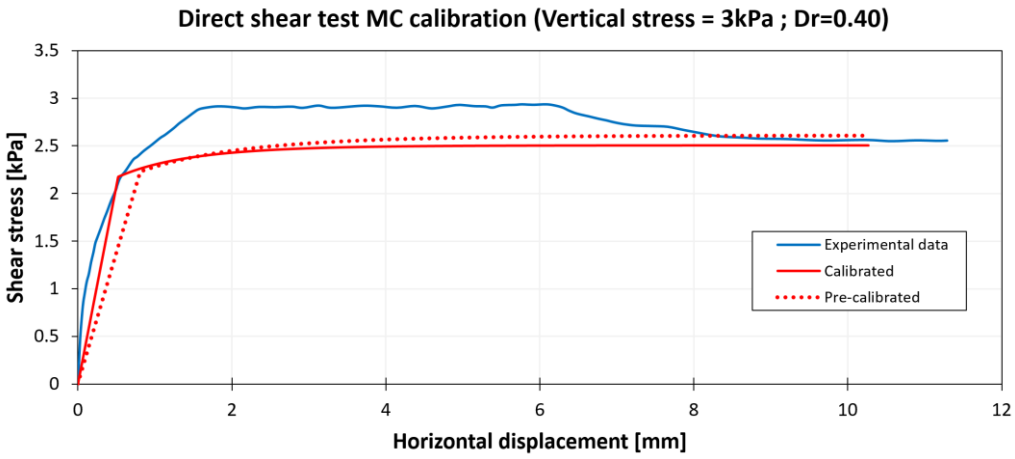

Figure 6.2 Direct shear test MC simulations and experimental results comparison.

5.2 HS parameter determination & calibration

The HS preliminary set of parameters were obtained from the empirical results and correlations of Chapter 4 and by as well adopting default parameters for R_f, **m** and v_{ur} that are commonly used for sands. For the calibrated set of parameters, a best-fit curve was done but also taking into consideration a parameter determination procedure that relies on D_r. (Brinkgreve, Engin & Engin, 2010). This cited procedure presents empirical formulations based on a large database of sands, using D_r as the sole input value. From these correlations, the obtained R_f and **m** were adopted for the calibrated set of parameters, which yielded satisfactory best-fit results. The unloading-reloading Poisson's ratio was adopted as a value within the usual range of 0.1÷0.25 for loose-medium sands. The stress reference for the stiffness parameters is 1kPa.

Table 5.3 and Table 5.4 show the preliminary and the calibrated set of parameters for the HS model. Figure 5.3 and Figure 5.4 show the comparison between the 2 sets of parameters and the experimental results.

Table 5.3 HS determined parameters prior to calibration.

HS parameters pre-calibrated		
Reference Elastic modulus [kPa]	E_{50}	500
Oedometer stiffness [kPa]	E_{oed}	750
Unloading-reloading stiffness [kPa]	E_{ur}	3000
Cohesion [kPa]	c	0
Peak friction angle [°]	φ_p	48
Dilatancy angle [°]	ψ	13
U-R Poisson's ratio [-]	v_{ur}	0.175
Power exponent [-]	m	0.5
Failure ratio factor [-]	R_f	0.9
Lateral earth pressure at rest [-]	K_o	0.426
Reference stress [kPa]	P_{ref}	3

Table 5.4 HS parameters after calibration.

HS parameters calibrated		
Reference Elastic modulus [kPa]	E_{50}	700
Oedometer stiffness [kPa]	E_{oed}	700
Unloading-reloading stiffness [kPa]	E_{ur}	2800
Cohesion [kPa]	c	0
Peak friction angle [°]	φ_p	47.2
Dilatancy angle [°]	ψ	12
U-R Poisson's ratio [-]	v_{ur}	0.2
Power exponent [-]	m	0.6
Failure ratio factor [-]	R_f	0.8
Lateral earth pressure at rest [-]	K_o	0.426
Reference stress [kPa]	P_{ref}	1

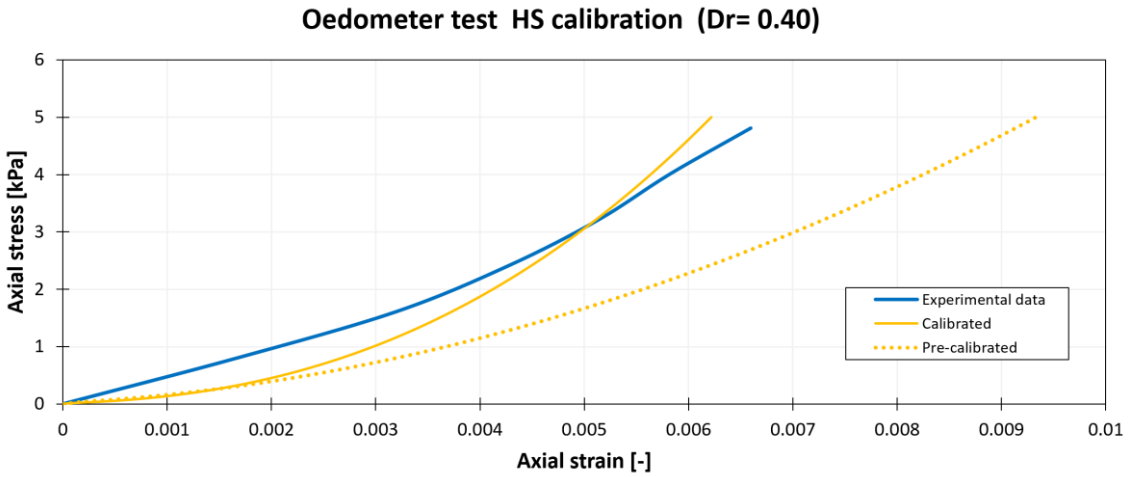

Figure 5.3 Oedometer test HS simulations and experimental results comparison.

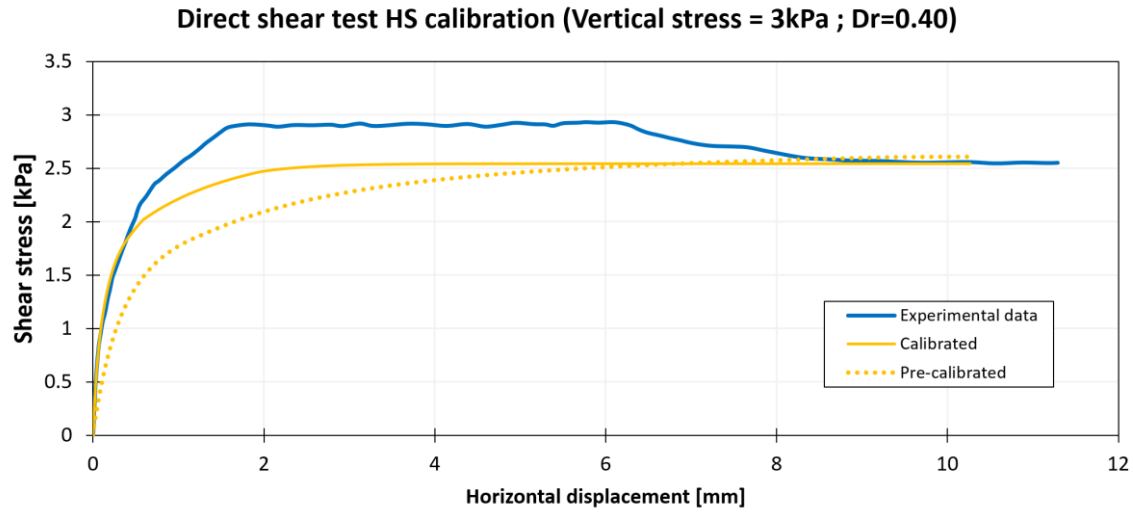

Figure 5.4 Direct shear test HS simulations and experimental results comparison.

5.3 UBCS parameter determination & calibration

For the UBCS model, the 3 stiffness modulus were initially estimated by the empirical correlations based on a SPT-corrected number N_{60}=4, which was as well obtained from the correlation of Equation 8 (Section 2.2.3). The stiffness exponents m_e, n_e , p_e were defined as the default values commonly used for this model. The failure ratio R_f was defined as the default for UBCS. The stress reference was fixed at 3kPa. φ_{cv} was defined as the one measured by Masin (2017) and the peak friction angle as shown in Section 4.2.4.

The Calibration of the UBCS parameters were done by modifying the stiffness modulus and the shear strength parameters. The stiffness exponents and failure ratio remained unmodified to conserve the usual values as adopted in common engineering practice.

The following Table 5.5 and Table 5.6 show the preliminary and the calibrated set of parameters for the UBCS model. Figure 5.5 and Figure 6.6 show the comparison between the 2 sets of parameters and the experimental results.

Table 5.5 UBCS determined parameters prior to calibration.

UBCS parameters pre-calibrated		
Critical state friction angle [°]	φ_{cv}	34
Peak friction angle [°]	φ_p	48
Cohesion [kPa]	c	0
Elastic shear modulus [-]	K_G^e	700
Elastic bulk modulus [-]	K_B^e	500
Plastic shear modulus [-]	K_G^p	150
Elastic bulk exponent [-]	m_e	0.5
Elastic shear exponent [-]	n_e	0.5
Plastic shear exponent [-]	n_p	0.5
Failure ratio [-]	R_f	0.9
Reference stress [kPa]	P_A	3

Table 5.6 UBCS parameters after calibration.

UBCS parameters calibrated		
Critical state friction angle [°]	φ_{cv}	34.5
Peak friction angle [°]	φ_p	46.9
Cohesion [kPa]	c	0
Elastic shear modulus [-]	K_G^e	400
Elastic bulk modulus [-]	K_B^e	300
Plastic shear modulus [-]	K_G^p	450
Elastic bulk exponent [-]	m_e	0.5
Elastic shear exponent [-]	n_e	0.5
Plastic shear exponent [-]	n_p	0.5
Failure ratio [-]	R_f	0.9
Reference stress [kPa]	P_A	3

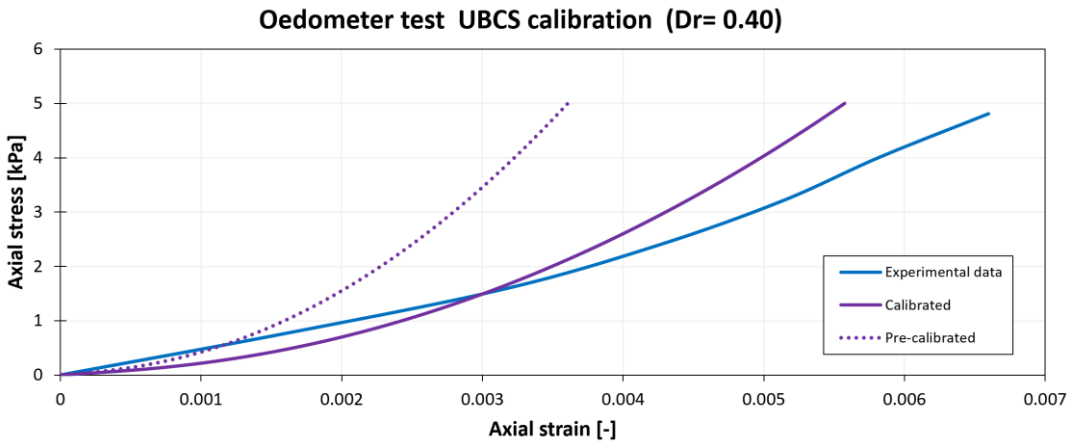

Figure 5.5 Oedometer test UBCS simulations and experimental results comparison.

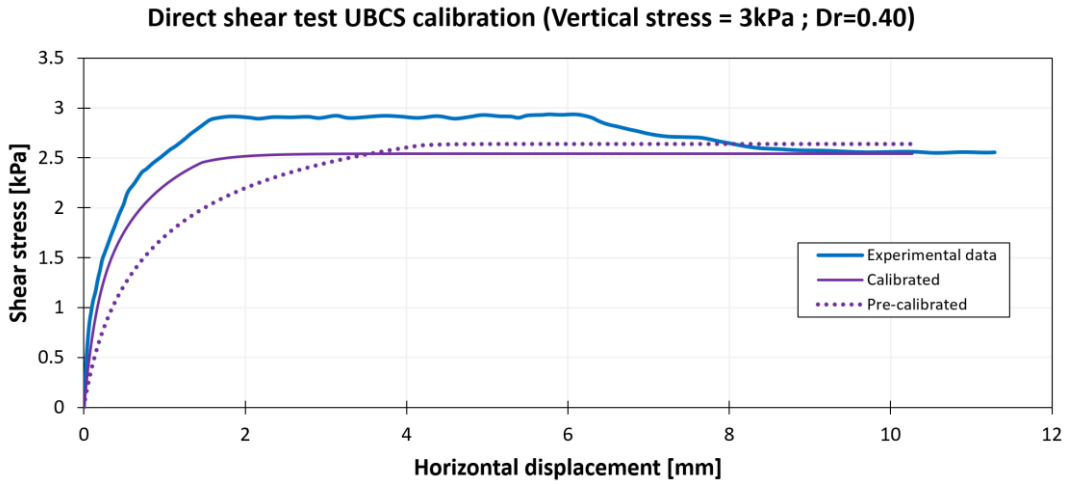

Figure 5.6 Direct shear test UBCS simulations and experimental results comparison.

5.4 HP parameter determination & calibration

For the preliminary HP parameter determination it was originally intended to calculate h_s and **n** from Oedometer tests at a low stress range of (1÷5) kPa. A fundamental issue regarding h_s and **n** determination at low stresses is shown in Figure 5.7. An example of an Oedometer test (Geba sand) performed at a medium-high stress range was used for commenting this parameter determination issue (Azua, 2017). As it may be seen, obtaining two different slopes of compression indexes C_c within a range of approximately (1÷50) kPa is not feasible. The difference between C_{c1} and C_{c2} at this range is negligible, thus attributing to nearly linear-paths at low stresses. Researchers have determined the HP parameters within higher stress ranges than the one used in this research project. An attempt was done to use the parameters obtained by this linear paths but the simulations were highly diverging from the experimental results of the OED and DS tests. As a consequence, the measured and calibrated parameters of a recent work were used as the preliminary set of parameters (Masin, 2017) .

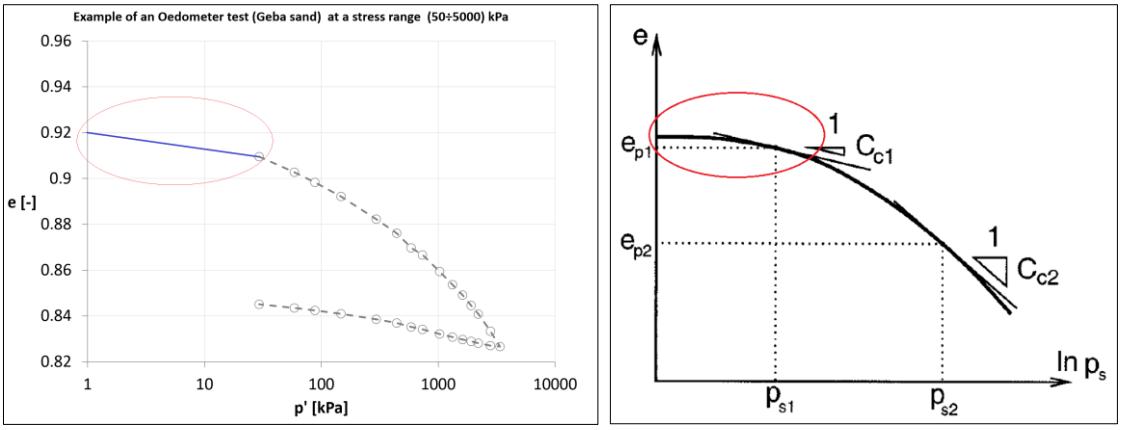

(a) *(b)*

*Figure 5.7 h_s and **n** issue at very low stress ranges for Geba sand. **(a)** (after Azua, 2017) , **(b)*** (Herle & Gudehus, 1999).

Regarding the parameters α and β, the available CDTX tri-axial data was used to estimate them. A value of 0.15 was obtained for α, and β=1.65, but it was preferred to adopt as well the calibrated parameters from Masin (2017). The void ratio parameters e_{d0} and e_{c0} were obtained from the measurements of minimum and maximum void ratio of Krapfenbaur (2016). For e_{i0} a correlation adopted for sub-angular-circular particles was assumed, as mentioned in section 2.2.4. The critical friction angle was defined as the measurement done by Masin (2017).

A calibration was performed by best-fitting the OED and DS curves, and it was necessary to only modify the critical state friction angle by increasing it significantly. The other parameters remained unchanged and decent best-fit curves where obtained.

The following Table 5.7 and Table 5.8 show the preliminary and the calibrated set of parameters for the HP model. Figure 5.8 and Figure 5.9 show the comparison between the 2 sets of parameters and the experimental results.

Table 5.7 HP determined parameters prior to calibration

HP parameters pre-calibrated		
Critical state friction angle [°]	φ_{cv}	34
Cohesion [kPa]	p_t	0
Granulate hardness [kPa]	h_s	2500000
Granulate exponent [-]	n	0.3
Minimum void ratio [-]	e_{d0}	0.64
Critical void ratio [-]	e_{c0}	1.07
Maximum void ratio [-]	e_{i0}	1.28
Factor alpha [-]	α	0.11
Factor beta [-]	β	2
Initial void ratio [-]	e	0.9

Table 5.8 HP parameters after calibration.

HP parameters Calibrated		
Critical state friction angle [°]	φ_{cv}	44.7
Cohesion [kPa]	p_t	0
Granulate hardness [kPa]	h_s	2500000
Granulate exponent [-]	n	0.3
Minimum void ratio [-]	e_{d0}	0.64
Critical void ratio [-]	e_{c0}	1.07
Maximum void ratio [-]	e_{i0}	1.28
Factor alpha [-]	α	0.11
Factor beta [-]	β	2
Initial void ratio [-]	e	0.9

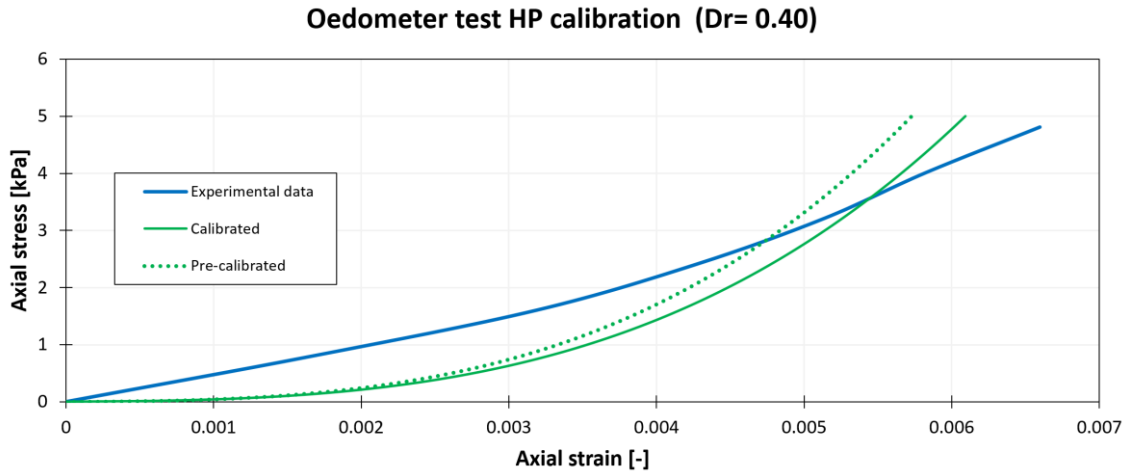

Figure 5.8 Oedometer test HP simulations and experimental results comparison.

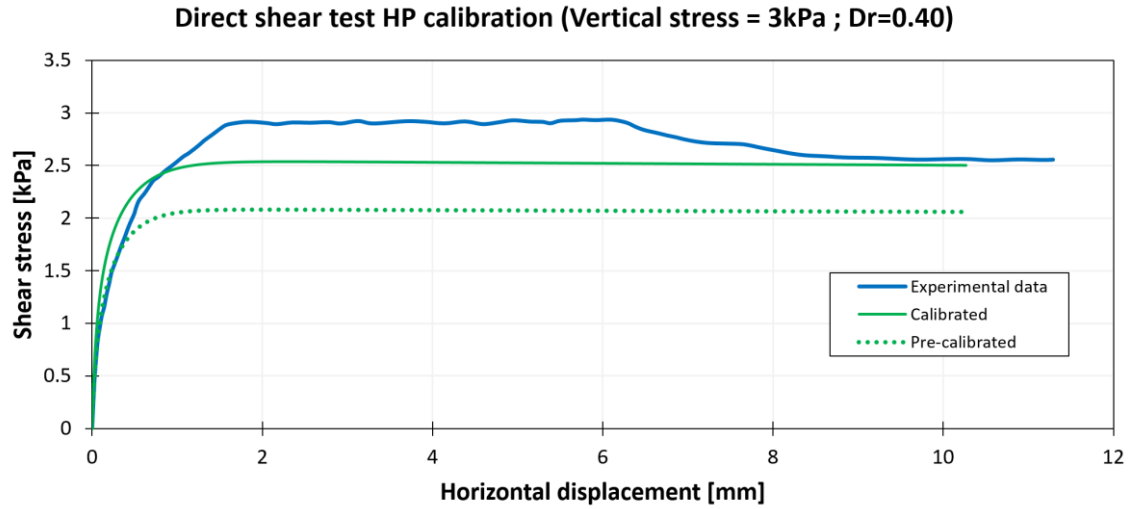

Figure 5.9 Direct shear test HP simulations and experimental results comparison.

It was not necessary to calibrate the preliminary HP parameters, with the only exception of φ_{cv}. This observation implies that the HP calibration experimental range of (20÷2000) kPa as stated by Herle and Gudehus (1999), might be extended. Results from these calibration show that the HP parameter determination at least for Geba sand may be used for an experimental range of (1÷2000) kPa.

5.5 ISHP parameter determination & calibration

No attempt was carried for estimating the additional 5 parameters of the ISHP model, as the lack of proper equipment rendered it unfeasible. For a first attempt, the parameters obtained by Masin (2017) were used in the preliminary set of parameters. A best-fit calibration was done for the 5 parameters, while still adopting the guidelines mentioned in 2.2.5.

The following Table 5.9 and Table 5.10 show the preliminary and the calibrated set of parameters for the ISHP model. Figure 5.10 and Figure 5.11 show the comparison between the 2 sets of parameters and the experimental results.

Table 5.9 ISHP determined parameters prior to calibration

ISHP parameters pre-calibrated		
Critical state friction angle [°]	φ_{cv}	44.7
Cohesion [kPa]	p_t	0
Granulate hardness [kPa]	h_s	2500000
Granulate exponent [-]	n	0.3
Minimum void ratio [-]	e_{d0}	0.64
Critical void ratio [-]	e_{c0}	1.07
Maximum void ratio [-]	e_{i0}	1.28
Factor alpha [-]	α	0.11
Factor beta [-]	β	2
Initial void ratio [-]	e	0.9
Factor for 180° reversal [-]	m_R	5.5
Factor for 90° reversal [-]	m_T	3.9
Elastic range size [-]	R	1E-04
Steepness degradation factor [-]	β_R	0.3
Steepness degradation factor [-]	χ	0.7

Table 5.10 ISHP parameters after calibration.

ISHP parameters calibrated		
Critical state friction angle [°]	φ_{cv}	44.7
Cohesion [kPa]	p_t	0
Granulate hardness [kPa]	h_s	2500000
Granulate exponent [-]	n	0.3
Minimum void ratio [-]	e_{d0}	0.64
Critical void ratio [-]	e_{c0}	1.07
Maximum void ratio [-]	e_{i0}	1.28
Factor alpha [-]	α	0.11
Factor beta [-]	β	2
Initial void ratio [-]	e	0.9
Factor for 180° reversal [-]	m_R	2.1
Factor for 90° reversal [-]	m_T	1.05
Elastic range size [-]	R	1E-05
Steepness degradation factor [-]	β_R	0.5
Steepness degradation factor [-]	χ	1

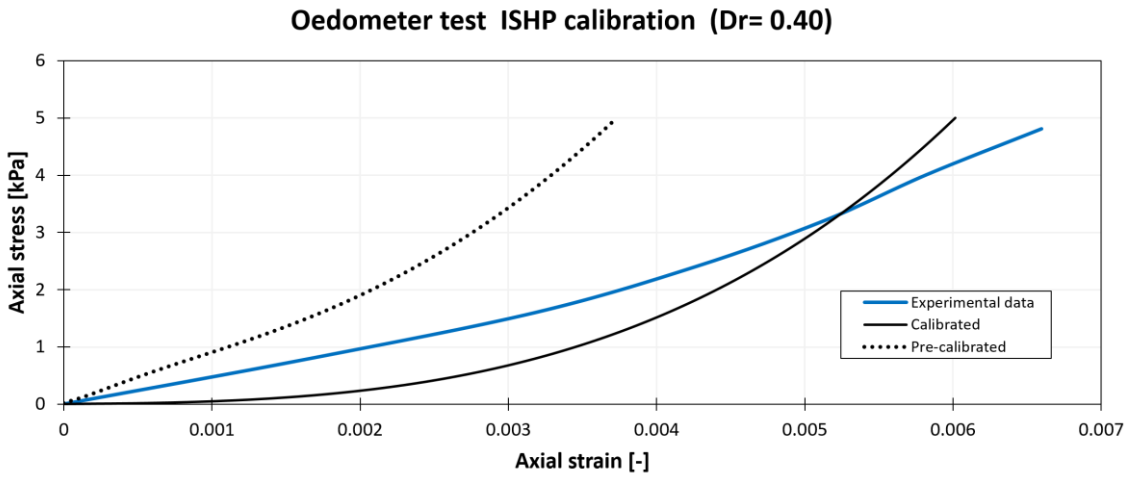

Figure 5.10 Oedometer test ISHP simulations and experimental results comparison.

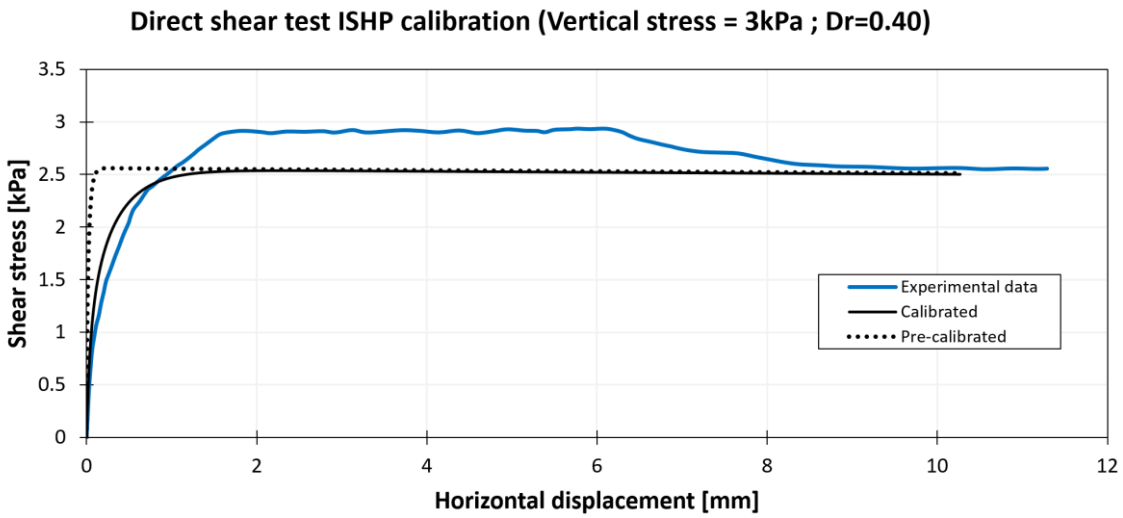

Figure 5.11 Direct shear test ISHP simulations and experimental results comparison.

Some comments may be done regarding the ISHP calibration. The preliminary set of parameters shows a dilative behavior if an undrained tri-axial simulation is done at a very low stress reference (P_{ref}=2 kPa). This is contrary to the observed behavior at a stress level of P_{ref}=100 kPa with the same set of parameters (as seen in Figure 5.12, Figure 5.13 and Figure 5.14).

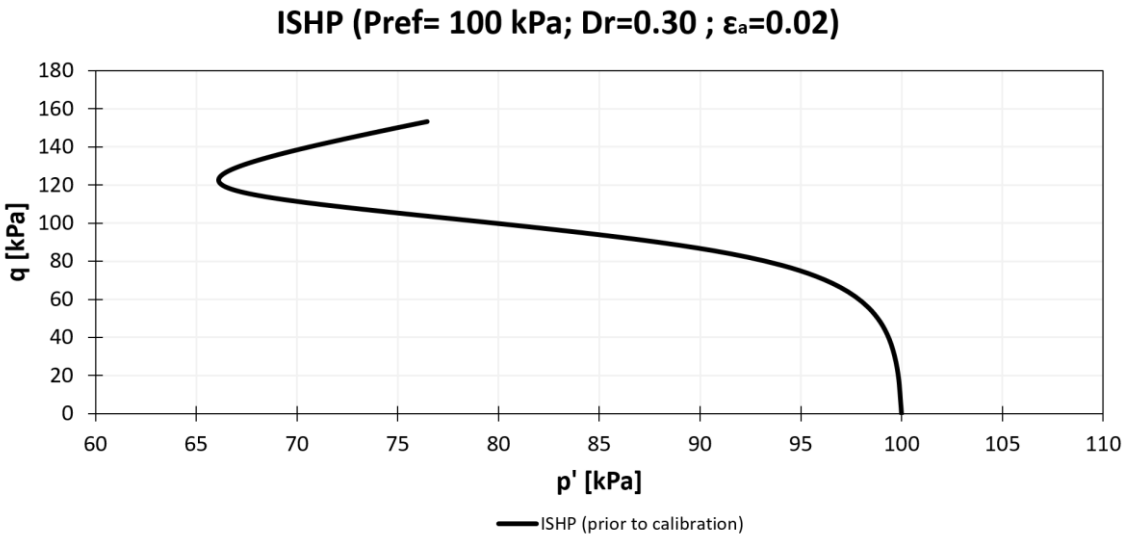

Figure 5.12 Contractive behavior of CUTX simulation at P_{ref}=100 kPa using the pre-calibrated ISHP set.

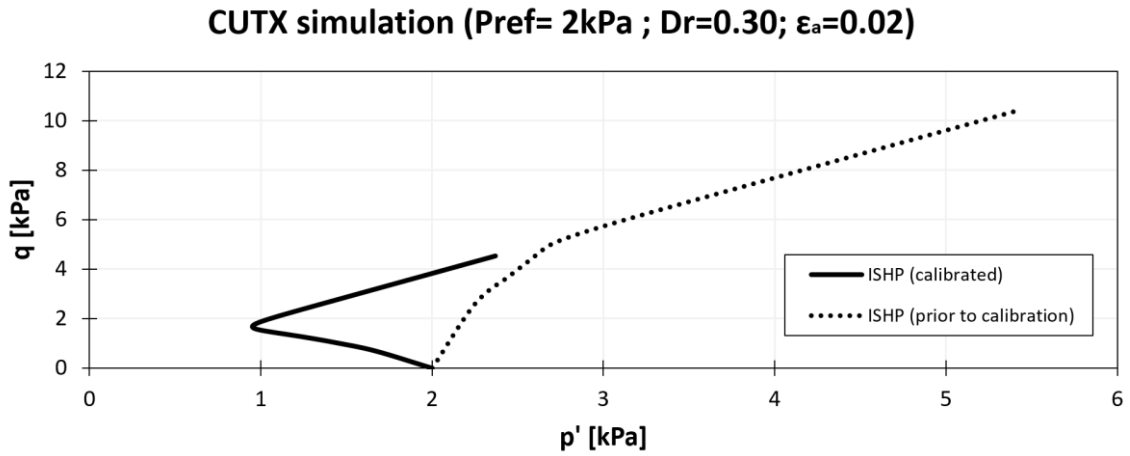

Figure 5.13 Dilative behavior of CUTX simulation at P_{ref}=2 kPa using the pre-calibrated ISHP set, and compared to the contractive behavior with the calibrated ISHP set.

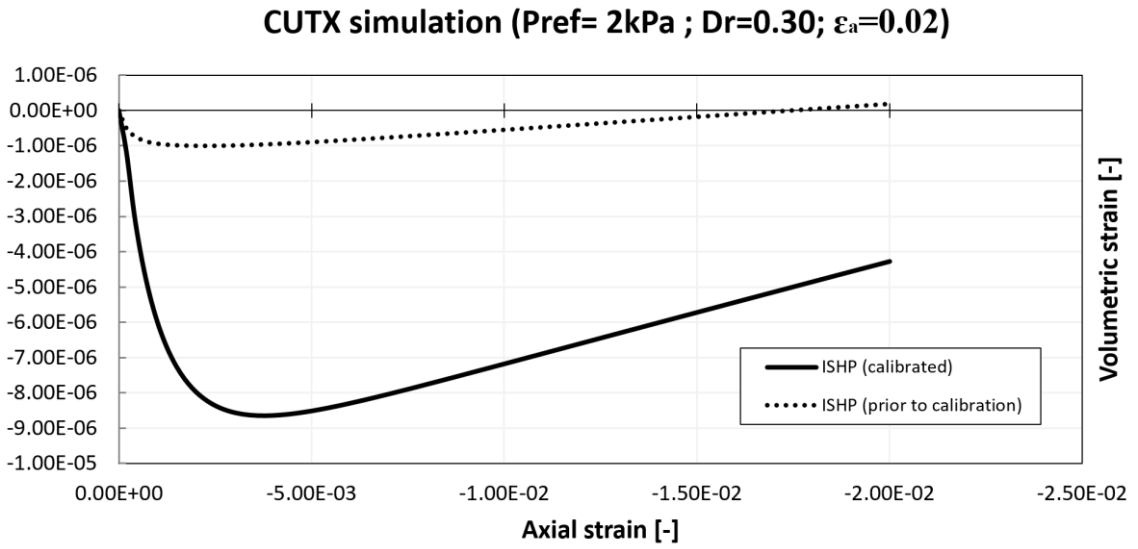

Figure 5.14 Dilative behavior of CUTX simulation at P_{ref}=2 kPa using pre-calibrated ISHP set, and compared to the contractive behavior with the calibrated ISHP set. (+ sign is extension, - sign is compression)

The observed results after testing several simulations at different stress levels, show that the 5 additional parameters of ISHP cannot be used with the current constitutive formulation for a full range of stresses (i.e. 1÷2000 kPa). It was found that the set obtained by Masin (2017) shows significant contractive behavior up to stresses as low as 50kPa, and at values lower than 50kPa it started showing an increased tendency towards dilative behavior. The calibrated set of ISHP parameters is suitable for working at least within the stress range of this project (i.e. 1÷4 kPa). A sensitivity analysis of the ISHP parameters may be found at Appendix B.

5.6 Model calibration comparisons

Figure 5.15 and Figure 5.16 show undrained tri-axial simulations at a pressure reference of 2kPa, D_r=0.30 and axial strain of 0.02 for all the calibrated models.

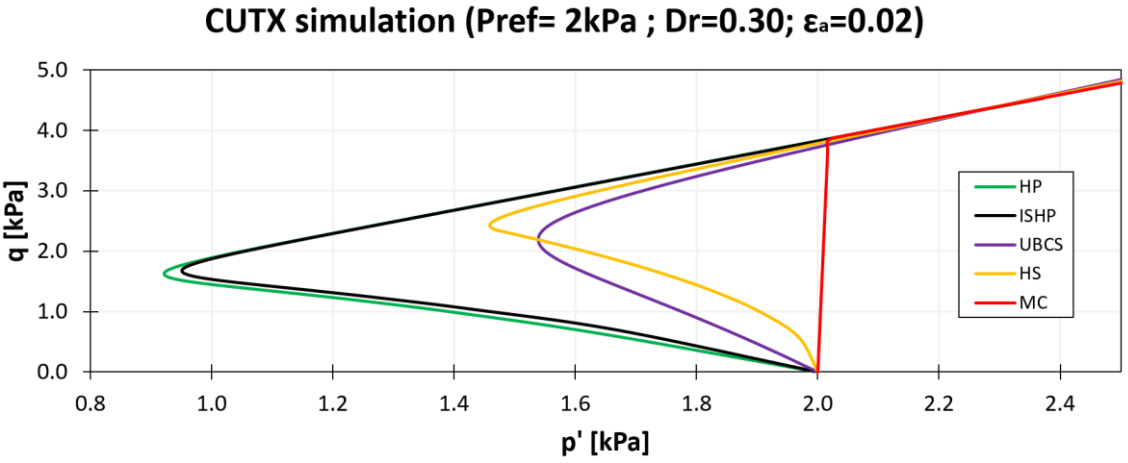

Figure 5.15 Effective stress path p'-q comparison of all calibrated constitutive models.

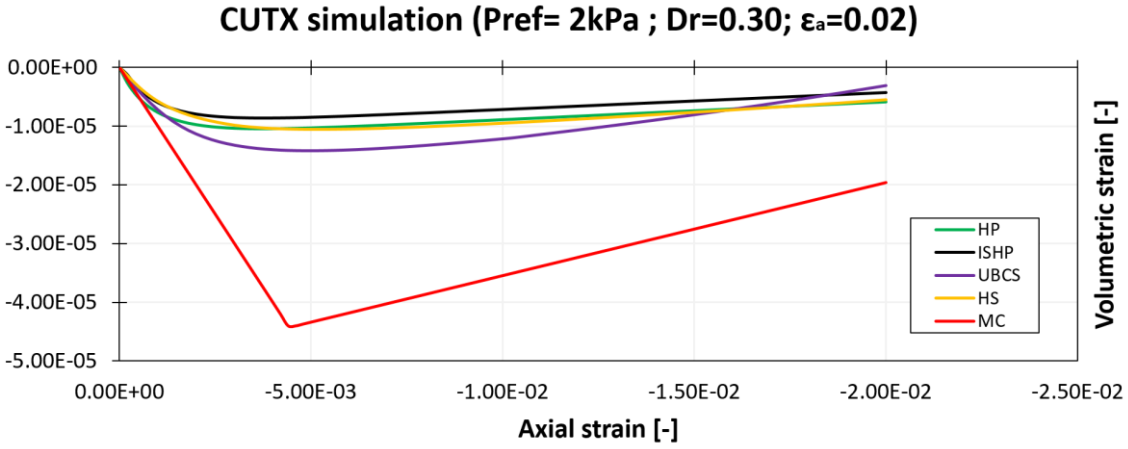

Figure 5.16 CUTX simulations at P_{ref}=2 kPa of all the calibrated constitutive models. (+ sign is extension, - sign is compression)

The hypoplasticity super exceeded the EP models in terms of contractive behavior. It must be noted that the UBCSAND model had the potential to generate significant soft behaviors that far surpassed the HP model, but this additional simulations were poorly calibrated and thus discarded.

Chapter 6: FEM application and modelling results

6.1 General description of FEM approach

As stated before, the software PLAXIS is the main tool for numerically analyzing the SL-tank through a finite elements approach (FEM) with chosen constitutive models.

A plane strain condition with 15-Noded elements were implemented to model the SL-tank. A total of 2076 elements, 17029 nodes and an average element size of 0.057m were used. A preliminary mesh sensitivity analysis showed that a denser element mesh was not required.

The adopted scheme for simulating a SL-tank test was by means of a staged construction analysis through a consolidation calculation-type procedure. Consolidation in PLAXIS works as an initially undrained behavior-calculation which is followed by a drained calculation after a determined time (depending of permeability *K*). The numerical simulations aimed for a total time of approximately 90s (approximately at a maximum tilting angle of 9°). Failure from the available experimental tests was observed approximately at 60s of elapsed time, in which at 63s peak excess pore pressures were detected. All models were based solely on a fixed tilting rate of 0.10 °/s.

The model scheme was carried through a total of 9 phases , in which from phases (0÷6) a time interval of 10s per phase was used (Table 6.1). At phase 7, a time interval of 3s was used as a means to study the short time interval in which failure and peak excess P_w were observed from experimental results. Phases 8 and 9 had time intervals of 7s and 20s respectively, as a means to allow excess P_w dissipation and reaching the same total elapsed time as real tests. Vertical and horizontal pseudo static acceleration components α_v and α_h were used to progressively simulate the tilting mechanism by modifying the gravitational components of the model over each phase (Table 6.1) . The last but most crucial component of this model scheme lies in the adopted bottom fixities. From phases (0÷6) a fully fixed condition (Figure 6.1) did not allow any material displacements but at phase 7 a triggering mechanism was induced. Horizontal displacements were allowed at the bottom boundary to induce a failure effect, which was maintained as a normally fixed condition (Table 6.1) from phases (7÷9).

Table 6.1- Adopted model scheme for SL-tank model.

Phase	Time interval [s]	Tilting angle [°]	α_h [-]	α_v [-]	Bottom fixity
0	0	0	0	0	Fully fixed
1	10	1	-0.01745	-0.00015	Fully fixed
2	10	2	-0.0349	-0.00061	Fully fixed
3	10	3	-0.05234	-0.00137	Fully fixed
4	10	4	-0.06976	-0.00244	Fully fixed
5	10	5	-0.08716	-0.00381	Fully fixed
6	10	6	-0.10973	-0.00604	Fully fixed
7	3	6.3	-0.12187	-0.00745	Normally fixed
8	7	7	-0.12187	-0.00745	Normally fixed
9	20	9	-0.15643	-0.01231	Normally fixed

The motivation for changing boundary fixities at phase 7 (Figure 6.2) is due to the chosen approach to simulate the Static liquefaction tank. Initially, the SL-tank was modelled by using solely fully fixed conditions at the bottom horizontal boundary, since the SL-tank's bottom contact surface was described as significantly rough. Preliminary simulations showed no notorious soil responses that could relate to failure or prone to failure scenarios if only fully fixed conditions (at the bottom) were used. Hence, an induced-failure condition was generated by modifying the lower boundary condition.

Figure 6.1 and Figure 6.2 illustrate the adopted mesh and boundary fixities. For the 2 vertical boundaries, a normally fixed condition was adopted (i.e. no allowable displacements in the x-direction), the upper horizontal boundary is free (i.e. allowed displacements in x and y directions) and the lower horizontal boundary is fully fixed (i.e. no displacements in x and y direction). These boundary fixities were modified for phases (7÷9) (Figure 6.2), in which the bottom horizontal boundary was changed to normally fixed conditions.

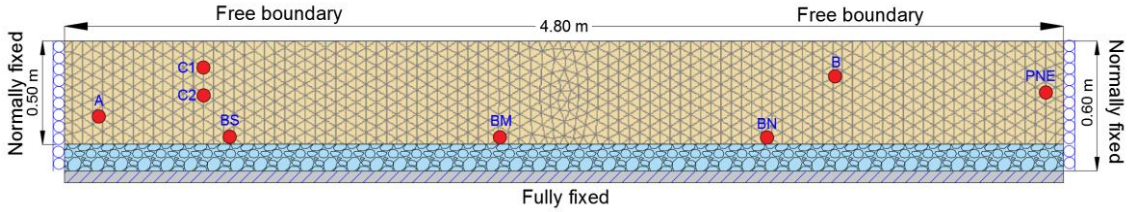

Figure 6.1- Adopted mesh, curve points, and boundary fixities at phases (1÷6)

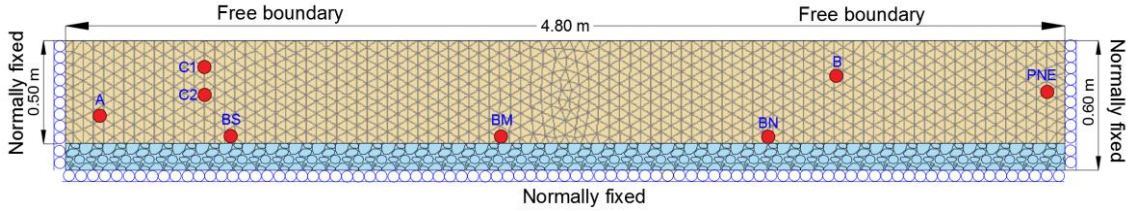

Figure 6.2- Adopted mesh, curve points, and boundary fixities at phases (7÷9) (triggering mechanism).

Figure 6.1 and Figure 6.2 depict the modelled Geba sand layer of 0.5m, which lies on top of a highly porous material of 0.1m. In the experimental tank facility, this porous material is directly interacting with the bottom sand material, which is the motive why it was added to study its behavior within this model. Dissipation of excess P_w, as well as groundwater flow between the two given materials is of crucial relevance within the experimental test.

An important remark is that this model does not use input of water Heads, nor groundwater flow. The model may be described as a dry condition but with the distinction that an effective unit weight γ'_{soil}=8 kN/m^3 is used as input parameter.

The dry model condition was chosen because a groundwater flow condition was not feasible for neither Consolidation or Fully coupled calculation-types when adopting pseudo static accelerations. Obtained results with groundwater flow were not reliable and generated unrealistic flow conditions (flow in contrary direction and incorrect Head values), thus

groundwater flow was not used for this work. The purpose of the highly porous layer was merely to allow excess P_w dissipation at the bottom sand layer location, which occurs for the experimental test as well.

Excess pore pressure within the chosen model scheme was purely by means of a mechanical calculation (not based in Head inputs), and its development is based on the following expression:

$$dP_w = \frac{e \cdot K_w}{e+1} \cdot d\varepsilon_v \qquad \text{(Eq. 23)}$$

From which, K_w is the bulk water stiffness (approximately 2.2GPa), e the void ratio, dP_w the excess pore water pressure and $d\varepsilon_v$ the change in volumetric strains. Equation 23 depicts that excess P_w is calculated as a function of the current void ratio and the change in volumetric strains. Regardless if a water layer is active or not in the model, excess P_w will still be generated.

The induced-failure approach relied mainly in the observation from experimental results in terms of excess P_w data recorded from the available sensors and failure pattern observations. As commented in Chapter 3, excess P_w were approximately zero through the main part of the tests until a sudden event triggers instantly a significant amount of excess P_w. This behavior could be related as a drained condition from a time interval t_o=(0÷60)s. Approximately at t=60s failure is reached, in which a tilting angle of approximately (6.5÷7) degrees was exhibited at that time. After the peak excess P_w is reached, it starts to dissipate at a noticeably fast rate.

The following commented points were of crucial relevance for the adopted numerical model:

- Using the value of permeability reported by Krapfenbauer (2016), as a means to simulate a quasi-drained behavior during phases (1÷6) of the model. At phase 7, an instant undrained behavior is triggered by means of a very short time interval of 3s and a modified bottom boundary fixity.
- The bottom boundary fixity of the SL-tank was modified from fully fixed to a normally fixed condition (at phase 7). Lateral displacements are allowed just at the moment in which the desired tilting angle (6.3°) and total time (60s) are reached.
- The overall modelled soil mass must show a flow pattern similar to the one reported from experimental observations (Section 3.2.3).
- The modelled highly porous layer has a permeability significantly higher than the one of the modelled sand layer for representing a realistic condition.
- The highly porous layer was modelled with the same chosen constitutive model as the one used for simulated sand layer. A linear elastic model for the porous layer was not used, as it yielded unrealistic and unreliable results in the sand layer.

Table 6.2- General SL-tank model input conditions.

General SL-tank model conditions		
Initial stress field [-]	K_0	0.44
Initial void ratio [-]	e	0.94
Soil unit weight [kN/m^3]	γ'_{soil}	8
Geba sand permeability [m/s]	K	4.2E-05
Porous layer permeability [m/s]	K_g	5.0E-02
Horizontal pseudo-acceleration [-]	α_v	Table 6.1
Vertical pseudo-acceleration [-]	α_h	Table 6.1

The simulated results from curve points BS, BM, BN, and PNE (Figure 6.1) were compared to the experimental data of excess Pw from the sensors BottomS, BottomM , BottomN, and PNE. Two stress points A, and B (Figure 6.1 and Figure 6.2) were chosen to show effective stress paths p'-q at these locations. Stress points C1 and C2 (Figure 6.1 and Figure 6.2) were used for Section 6.3. Additionally, an overview of the SL-tank will be shown in terms of stresses before (Phase 6) ,at failure (Phase 7), and after a significant dissipation of excess P_w (Phase 9).

6.2 Model simulation results

The MC, HS, UBCS and HP models were successfully run with no issues regarding solution convergence or any particular errors. The ISHP model was not able to perform flawlessly, as numerical converge issues did not allow to fully run past phase 7 (triggering mechanism). Due to this problem, results of the SL-tank involving the ISHP model were discarded.

Simulations of excess P_w evolution through time are shown in Figures 6.3, 6.4, 6.5 and 6.6. A shortened time interval of (50÷90)s is shown from the total test time of (0÷90)s. Peak excess P_w are reported in both the simulations and experimental results at approximately t=63s.

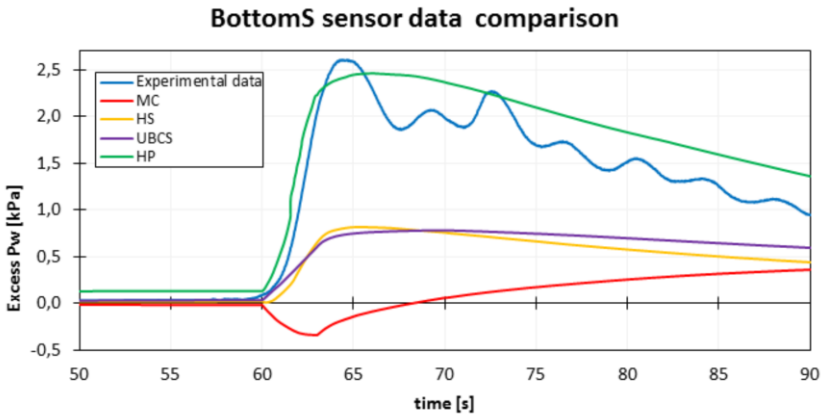

Figure 6.3- Comparison between numerical simulations and experimental result at location BottomS.

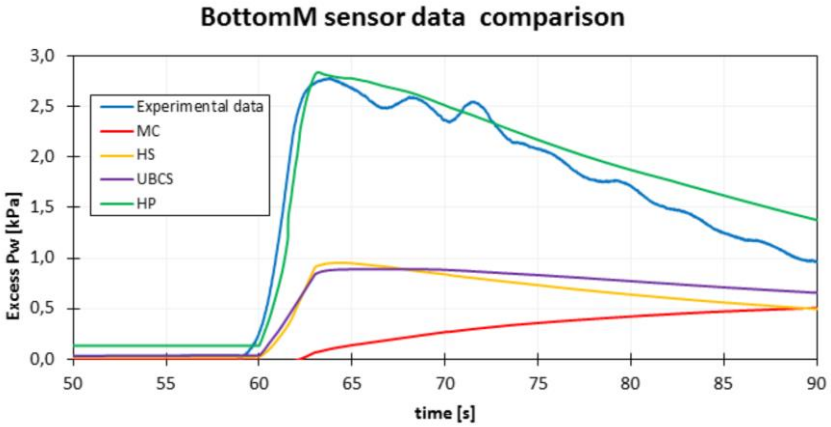

Figure 6.4- Comparison between numerical simulations and experimental result at location BottomM.

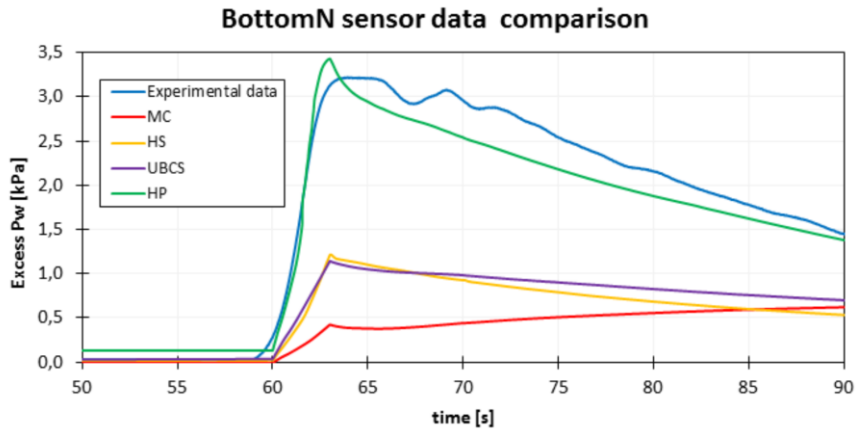

Figure 6.5- Comparison between numerical simulations and experimental result at location BottomN.

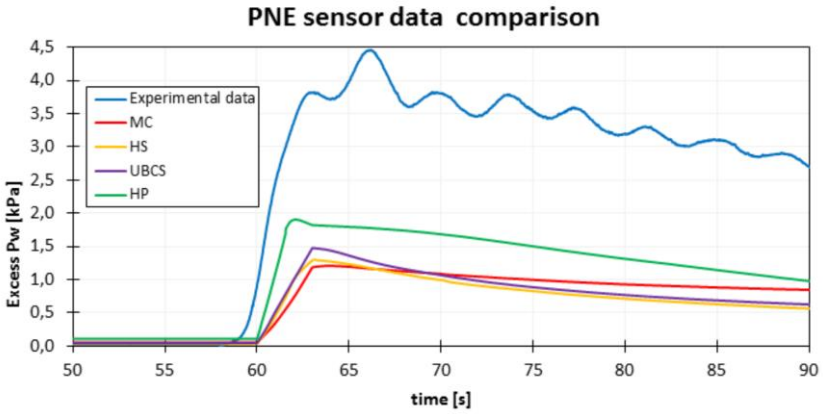

Figure 6.6- Comparison between numerical simulations and experimental result at location PNE.

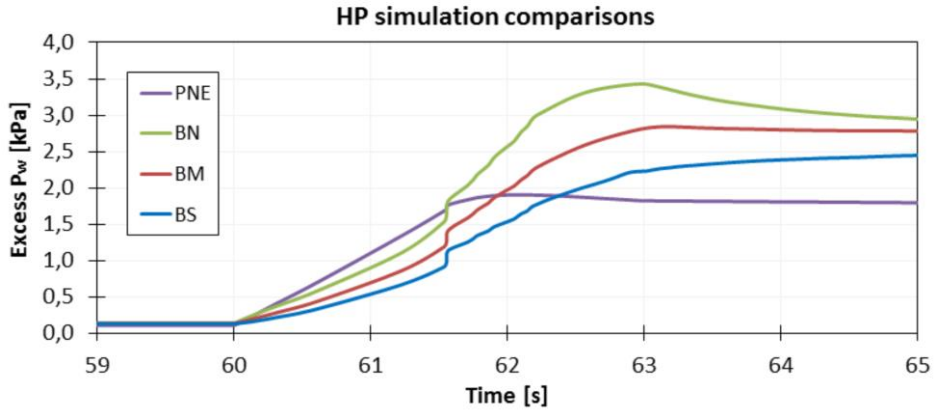

Figure 6.7- Comparison between simulation results for the HP model at the sensor locations.

The most prominent outcome of the excess P_w simulations is that the HP model is able to replicate comparable outputs to experimental results, with the only exception of the PNE location. Boundary issues from the numerical model are attributed to this significant discrepancy between simulation and experimental data at location PNE. The Elasto-Plastic models showed significantly lower excess Pw generations at all locations and even suction P_w (negative) at Southern locations.

At the Northern side of the SL-tank, excess P_w are larger than at the Southern side for both simulations and experimental results. The Northern side shows a behavior more prone to failure than the opposite side of the SL-tank (except at PNE) , which complies with experimental results and observations. Figure 6.7 may be related to the earlier failure of the soil mass at the Northern side, since Excess P_w develop at higher magnitudes during failure at the North side of the SL-tank (with exception of the location PNE). It must be noted that for location PNE, approximately until just before 61.5s it is still showing a larger P_w development than the other sensor locations during the triggering mechanism of phase 7.

Results in terms of deformation had a significantly low development, with deviator strains in ranges of circa 1E-04. Vertical strains were approximately in a range of (0.1÷2)%. See the Appendix C for output results regarding deformations for the HP model.

The following output illustrations will compare the HS and HP output results of the SL-tank model in terms of excess P_w and mean effective stress p'. Additionally, the principal stress directions of the HP model are shown as well, which also resemble the observed ones from the EP models. These model outputs are displayed by means of 3 sequences, before failure (phase 6), during failure (phase 7) and post failure after P_w dissipation (phase 9).

HS was chosen as the representative model for the EP formulations, as it was more reliable in terms of parameter determination-calibration than the UBCS model.

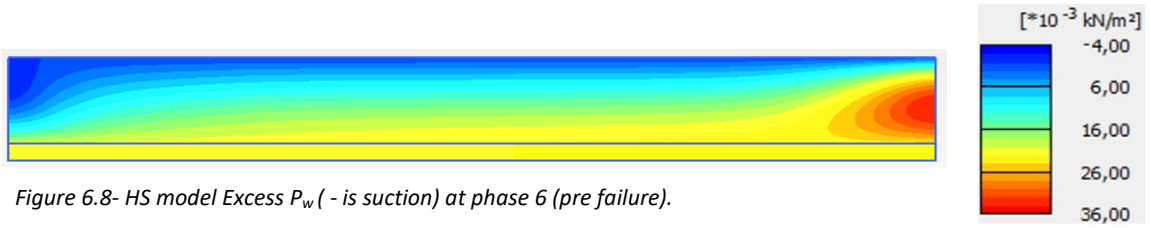

Figure 6.8- HS model Excess P_w (- is suction) at phase 6 (pre failure).

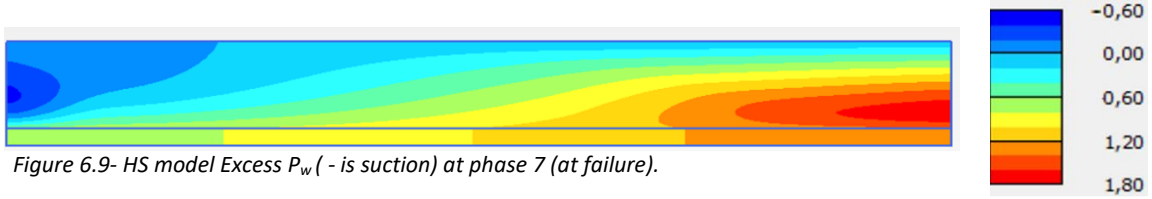

Figure 6.9- HS model Excess P_w (- is suction) at phase 7 (at failure).

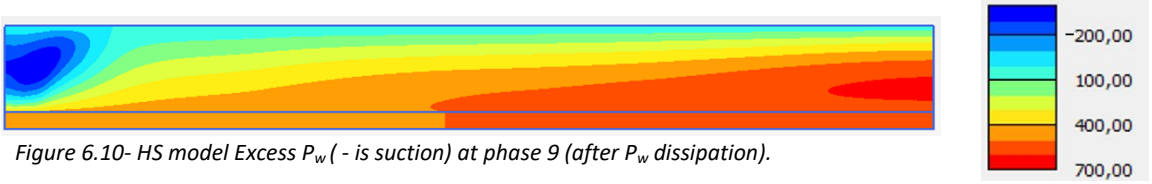

Figure 6.10- HS model Excess P_w (- is suction) at phase 9 (after P_w dissipation).

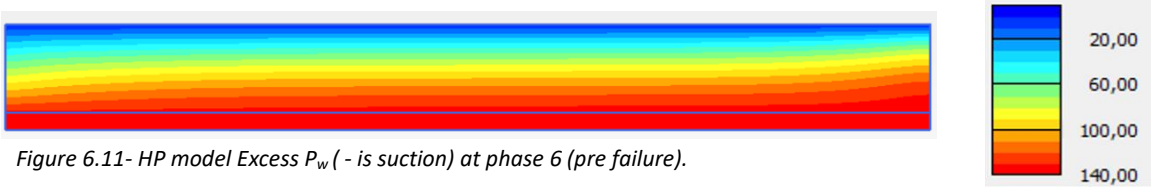

Figure 6.11- HP model Excess P_w (- is suction) at phase 6 (pre failure).

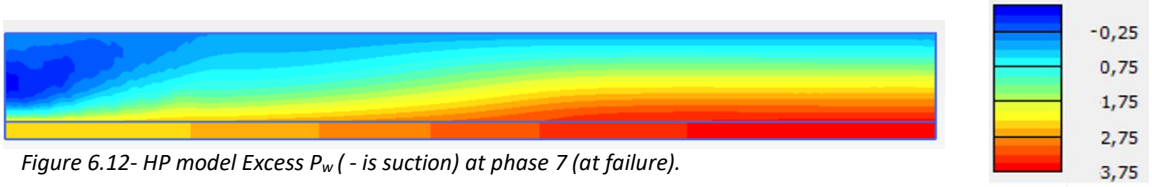

Figure 6.12- HP model Excess P_w (- is suction) at phase 7 (at failure).

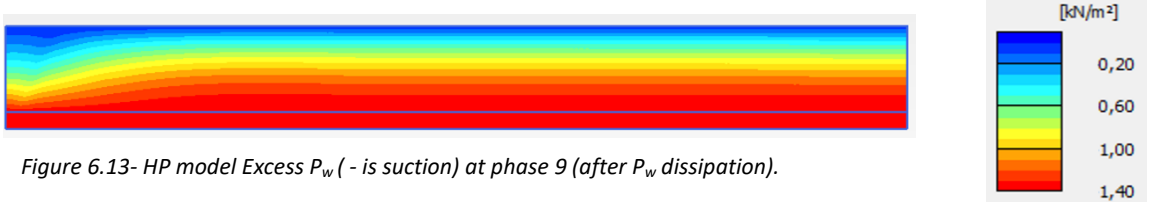

Figure 6.13- HP model Excess P_w (- is suction) at phase 9 (after P_w dissipation).

The excess P_w of the HP model is developed at a wider area in the Northern side of the SL-tank than the HS simulation. The magnitude of peak excess P_w from the HP results is 2 times higher than the HS peak outputs. The dissipation of excess P_w at the HS model exhibits a lower rate and magnitude in contrast to the faster and larger dissipation occurring in the HP model (Figure 6.13). At approximately 90s of elapsed modelled time, the excess P_w values reach diminished values of approximately 1.4kPa (as seen in experimental results as well).

The excess pore pressures are developing for both models mainly at the bottom location of the sand layer, and afterwards being immediately dissipated towards the porous layer from North to South direction. At isolated locations of the Southern side (next to the left boundary) negative (suction) P_w are generated during failure and they change to positive P_w as dissipation occurs. This suction generation may be attributed to boundary issues with the given models.

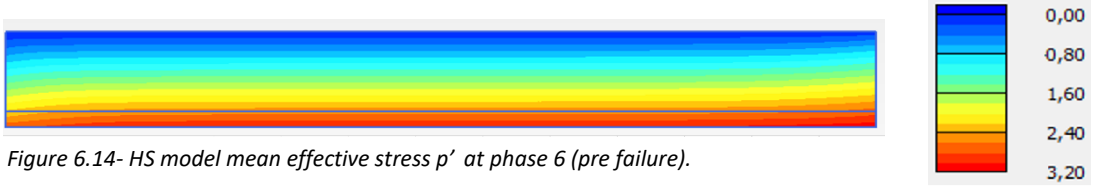

Figure 6.14- HS model mean effective stress p' at phase 6 (pre failure).

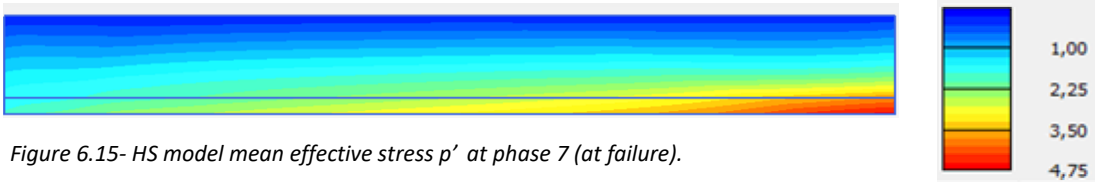

Figure 6.15- HS model mean effective stress p' at phase 7 (at failure).

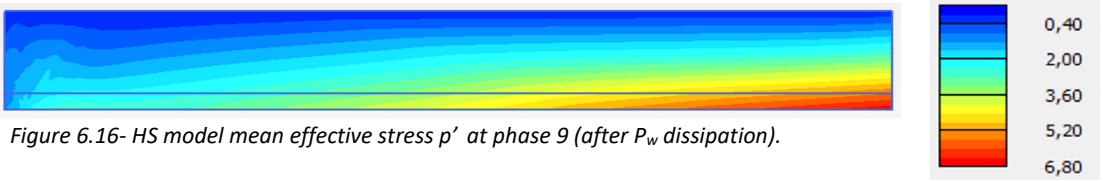

Figure 6.16- HS model mean effective stress p' at phase 9 (after P_w dissipation).

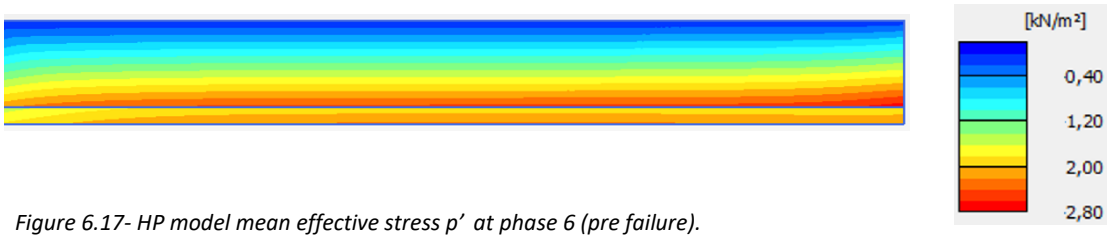

Figure 6.17- HP model mean effective stress p' at phase 6 (pre failure).

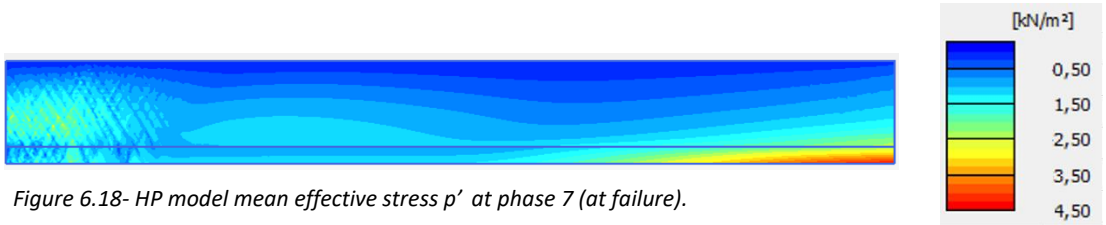

Figure 6.18- HP model mean effective stress p' at phase 7 (at failure).

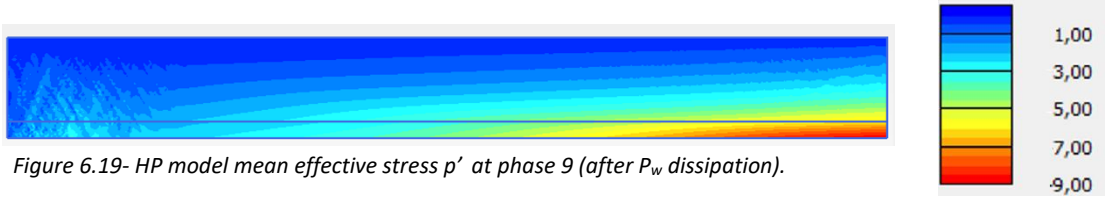

Figure 6.19- HP model mean effective stress p' at phase 9 (after P_w dissipation).

The HS model exhibits significant drops of mean effective stress at shallow locations of the sand layer but closer to the bottom boundary there is an increase of p' for HS outputs. It must be noted that no significant changes in the overall tank may be observed for p' in the HS. The HP outputs depict relevant reductions of mean effective stress at both shallow and locations closer to the bottom-North side (Figure 6.18) of the SL-tank. Boundary issues may be observed in Figure 6.18, from which significant drops of p' are developed and unusual fluctuations are obtained at this southern location. Outputs of deviator stress development manifest in a similar trend as the one appreciated in Figure 6.17, Figure 6.18 and Figure 6.19.

The following outputs of principal stress directions are solely presented for the HP model:

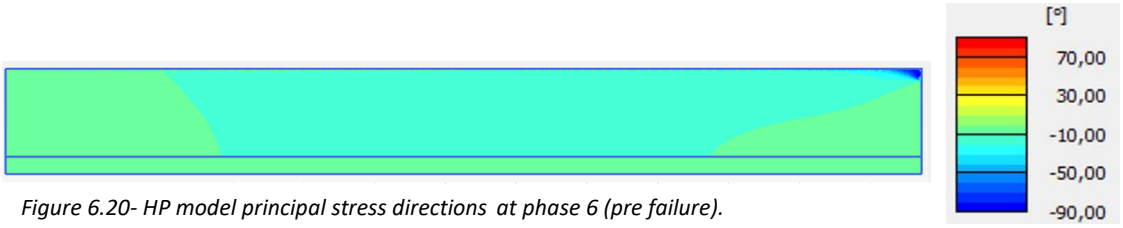

Figure 6.20- HP model principal stress directions at phase 6 (pre failure).

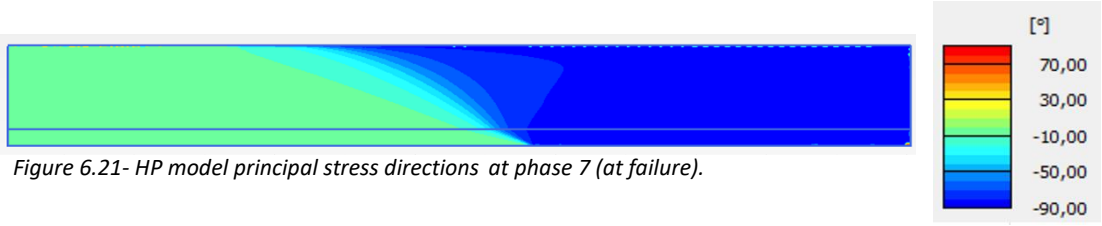

Figure 6.21- HP model principal stress directions at phase 7 (at failure).

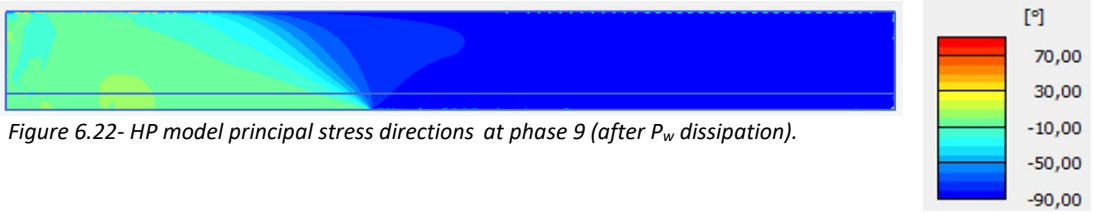

Figure 6.22- HP model principal stress directions at phase 9 (after P_w dissipation).

The principal stress directions of the SL-tank model before phase 7 show very mild deviation from its initial state, meaning that the major principal stress have only slightly rotated in less than 10°. At phase 7, stresses are rotated 90° at the Northern section of the SL-tank for both models, while stresses at the Southern side have rotated in angles approximately of (0÷10)°. These results show a behavior similar to tri-axial compression at the Southern side and tri-axial extension at the Northern side. Rough assumptions have been proposed for the geo-stress field of slopes, which fit with the description mentioned in this case. The Northern side would resemble the toe of the slope and the crest of the slope would be the Southern side.

Figure 6.23 illustrates a comparison of the CSL calculated theoretically by either tri-axial compression/extension, a plane strain approximation and the observed slope M for the CSL of the SL-tank model. The following equations are used for obtaining the M slope of the mentioned conditions:

$$M = \frac{6 \cdot \sin\varphi}{3 - \sin\varphi}$$ (Tri-axial compression) (Eq. 24)

$$M = \frac{6 \cdot \sin\varphi}{3 + \sin\varphi}$$ (Tri-axial extension) (Eq. 25)

$$M \approx \sqrt{3} \cdot sin\varphi$$ (Plane strain estimation) (Eq. 26)

From which, the friction angle φ in these formulations is related to φ_{cv}, but the parameter calibrations required to significantly modify this input parameter to a value of approximately φ=45°. Equation 26 was adopted from estimations presented by PLAXIS (2016).

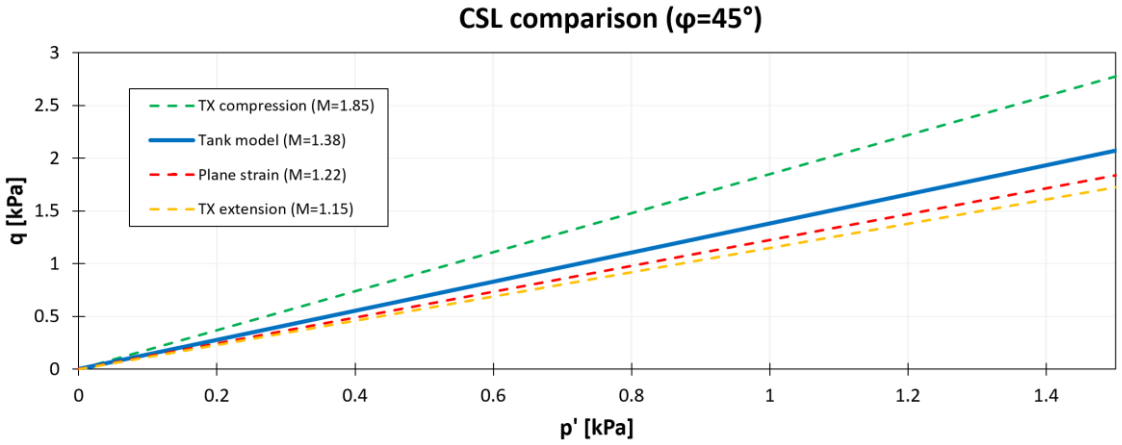

Figure 6.23- Critical state lines comparison between different assumptions and the numerically estimated CSL.

The Critical state line M=1.38 that was obtained from the numerical simulations of the SL-tank (Figure 6.23), lies between the tri-axial compression M-line and the plane strain approximation M-line, being closer to the plane strain case.

The following Figure 6.24 and Figure 6.25 show two representative stress paths of the Northern and Southern sides of the SL-tank.

Preliminary simulations with MC at fully undrained cases showed that the line M=1.38 coincides with the observed slope M for this given MC estimation.

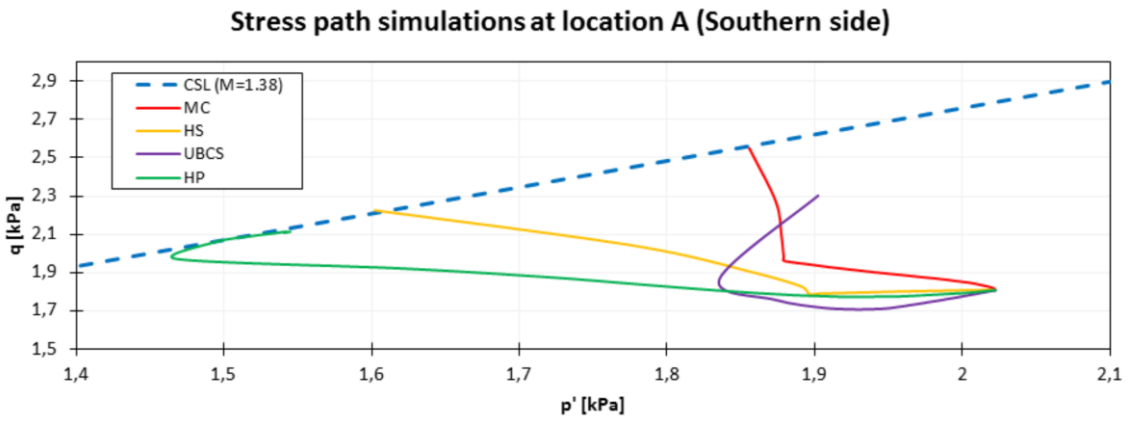

Figure 6.24- Stress path comparison p'-q of all chosen constitutive models at point A (representative result of the Southern side of the SL-tank).

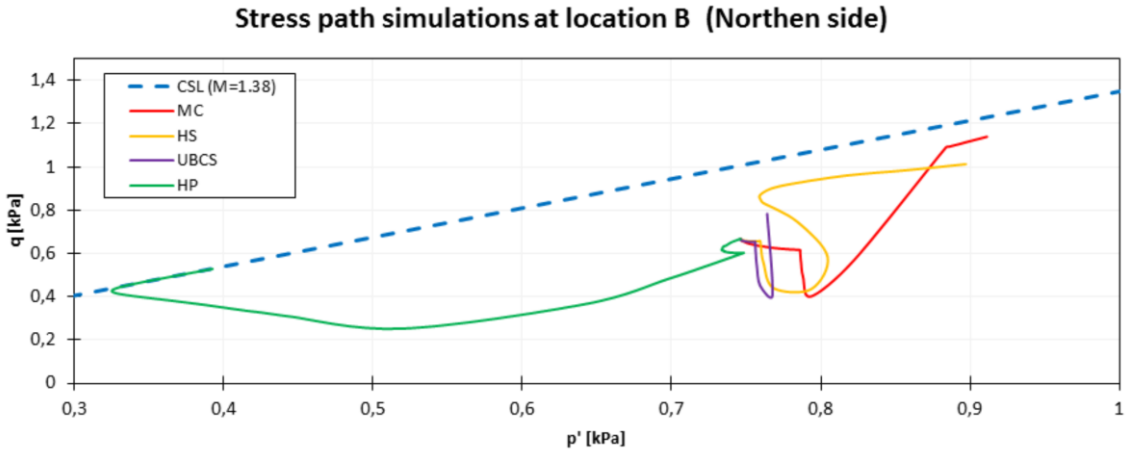

Figure 6.25- Stress path comparison p'-q of all chosen constitutive models at point B (representative result from the Northern side of the SL-tank).

Results from the EP models at the Southern side are not able to fully reach the CSL and their behavior is considerably less contractive than what may be observed for HP models. The most prominent difference lies in the sharper decrease of p' for the HP models, as well as reaching the CSL. The Northern side simulations showed a significant difference between the EP and HP models. Elasto-plastic models seem to be unable to model appropriately a significant loss of mean effective stress for it to be relatable to static liquefaction potential. EP models at the North section are merely describing a hardening behavior until any critical could be reached afterwards (not observed in simulations).

The constitutive laws of the HP model are a main limitation to the exposed results but the adopted boundary conditions are as well a critical aspect of the simulated SL-tank model. Output results from the numerical simulations such as in Figure 6.18 may be evidence of boundary effects or improper conditions adopted at the boundaries.

In Appendix F, output results of excess P_w and mean effective stresses are displayed for the same SL-tank HP model, with the main difference that a layer of 1m is modelled instead of 0.5m. The

exhibited behavior was similar to the previous SL-tank HP model but at higher stress levels. P_w dissipation was less effective for the same total elapsed time of 90s at a layer of 1m, given its longer drainage path.

Simulations with faster tilting rates than 0.10 deg/s were not adopted, as preliminary calculations showed no failure potential enhancement even if tilting rates as high as 1 deg/s was used at phase 7. Nevertheless, mild changes in the model behavior were observed if sufficiently high and unrealistic tilting rates were tested(such as (0.5÷1) deg/s)

6.3 Instability line framework

An instability region was estimated for the SL-tank by means of the instability line criteria. This framework was adopted by means of following 3 steps, as proposed by the author.

The first step (Section 6.3.1) consists in gathering undrained tri-axial data from non-cohesive soils similar to Geba sand. In this first approach, a representative instability line IL was adopted from empirical data and is further compared to results from the next steps.

The second step (Section 6.3.2) is based purely on a numerical simulation of an undrained tri-axial test, based on the UBCS model. This model was chosen particularly for being able to generate peak deviator stresses and trace a potential instability line IL. The used model parameters for this step were significantly modified from the ones obtained at Section 5.3. The UBCS parameters were calibrated as close as possible to the OED and DS data from Geba sand at low stresses. The instability line obtained from the second step is compared to the IL adopted from the first step, from which a representative line IL is chosen between these 2 steps.

The third step (Section 6.3.3) relies on observing stress paths at locations in which any unusual behavior could be observed in the SL-tank HP model (as presented in section 6.2). A potential instability line is traced from the chosen stress path locations, and finally a representative IL is adopted overall from the 3 commented steps within this framework.

6.3.1 Empirical data for IL estimation

Initially, experimental tests of sands with similar characteristics to Geba sand were revised from the works of Wichtmann & Triantafyllidis (2016) and Tsegaye (2009) . After selecting appropriate data based on granular properties, Toyoura sand and Karlsruhe fine (KF) sand CUTX results were used. Figure 6.26 illustrates the experimentally obtained instability lines for KF and Toyoura sand. It must be noted that these experimental results are within a medium-high stress range of (100÷200) kPa. Additionally, an instability line IL=0.65 was estimated from the revised empirical relationship mentioned in Section 2.1.6.

Table 6.3- General soil properties comparisons of Geba, KF, and Toyoura sand

Soil properties	Geba sand	Karlsruhe fine sand	Toyoura sand
φ_{cv} [°]	34	33.1	30.9
G_s [-]	2.67	2.65	2.64
e_{min} [-]	0.64	0.68	0.61
e_{max} [-]	1.07	1.05	0.98
D_{50} [mm]	0.118	0.14	0.16
c_u [-]	1.50	1.50	1.46
Angularity [-]	Sub-angular	Sub-angular	Sub-angular

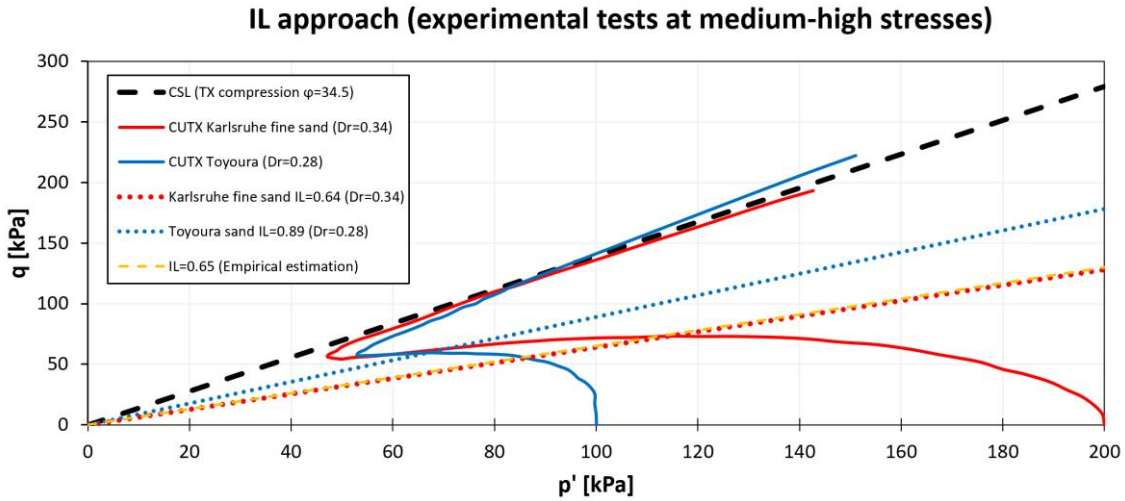

Figure 6.26- Effective stress paths of CUTX tests from Toyoura sand and KF sand

By adopting a factor of (φ_{cv}/ φ_{il})=1.77 for decreasing φ_{cv}=30° (Average φ_{cv} for fine sands) to a value of φ_{il}=17° and using Equation 24, an slope IL=0.65 is obtained. It may be observed from Figure 6.26 that the expression (φ_{cv}/ φ_{il})=1.77 for obtaining an IL=0.65, holds a strong resemblance to the estimated IL=0.64 from the KF fine sand. Thus, this empirical relationship may proof to be useful for the study of Geba sand.

6.3.2 CUTX simulation for IL estimation

The UBCS model was chosen to perform an additional calibration exclusively by being used in CUTX modelling for observing a peak deviator stress q. This calibration was done by trying to adopt curve fits from DS and OED of Geba sand data while still obtaining a CSL of M=1.38 within the CUTX simulations. An instability line IL=0.72 was traced at figure 6.27 for the simulated UBCS model. The line IL=0.72 holds a strong resemblance to an IL=0.74, which is the equivalent IL obtained through the empirical relationship of (φ_{cv}/ φ_{il})=1.77 and a φ_{cv}=34° (Geba sand φ_{cv}) after applying equation 24.

Table 6.4 Chosen parameter for the modified UBCS calibration

UBCS parameter set	Calibrated	Modified calibration
φ_{cv} [°]	34.5	31
φ_p [°]	46.9	31.5
c [kPa]	0	0
K_G^e [-]	400	700
K_B^e [-]	300	150
K_G^p [-]	450	500
m_e [-]	0.5	0.5
n_e [-]	0.5	0.5
n_p [-]	0.5	0.5
R_f [-]	0.9	0.9
P_A [kPa]	3	2

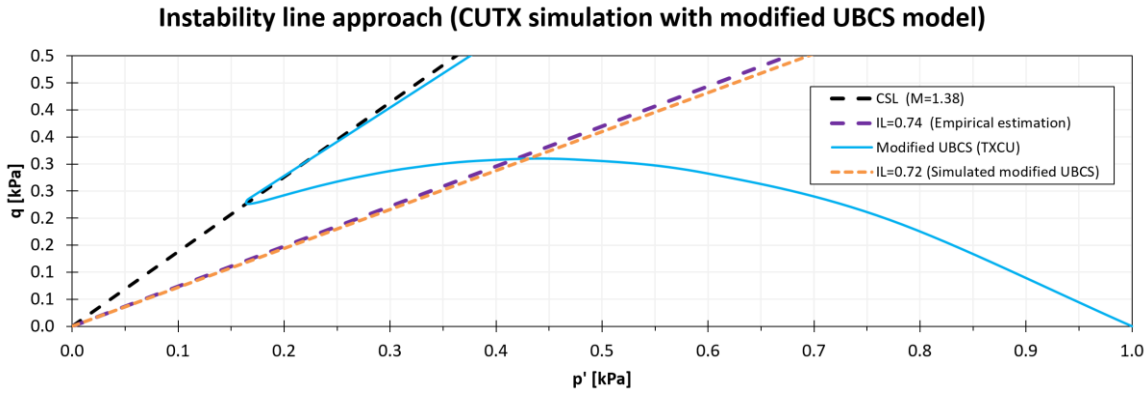

Figure 6.27- Simulated CUTX with modified UBCS model to estimate a IL for such conditions.

Figure 6.28 depicts that the modified UBCS has a nearly equal curve-fitting as the former calibrated set of parameters from Section 5.3, even though the new set of parameters is significantly different. Results from Figure 6.29 present the main differences between these calibrations in terms of shear strength. It was necessary to allow a low shear strength for matching the CSL of CUTX with the one observed at the SL-tank model (M=1.38).

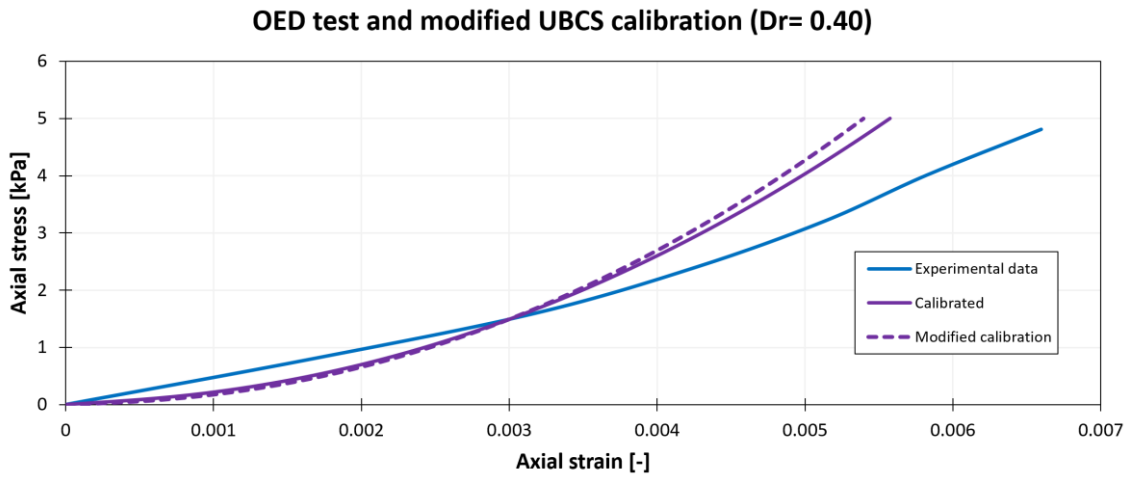

Figure 6.28- OED results from modified UBCS model compared to the calibrated results of Section 5.3.

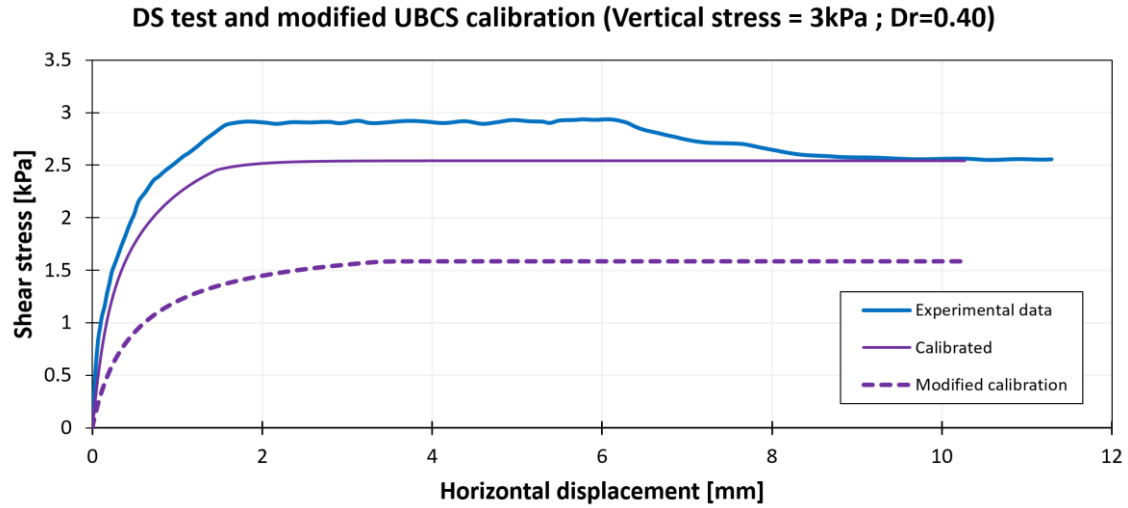

Figure 6.29- DS results from modified UBCS model compared to the calibrated results of Section 5.3.

From the comparison of potential IL from Section 6.3.1 and Section 6.3.2, the instability line IL=0.74 was the chosen overall from all the commented results of tri-axial tests/simulations.

6.3.3 HP Simulation of SL-tank model for IL estimation

The hypoplasticity model showed a significantly higher contractive behavior than the calibrated EP models but it was not able to generate notorious peak deviator stresses. The locations C1,C2 (Figure 6.30) are used to further study the potential location of instability lines in the SL-tank model.

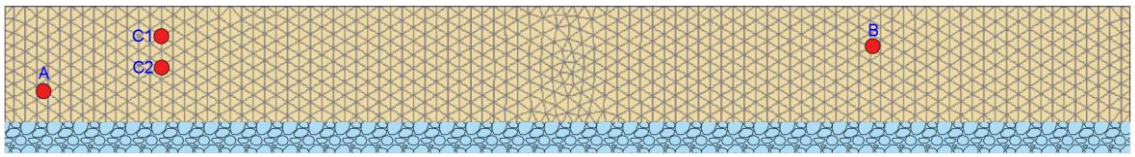

Figure 6.30- Selected locations to study the instability criteria in terms of effective stress paths.

The stress points C1,C2 shown in Figure 6.30 may be observed in terms of effective stress paths. At these locations, an unusual behavior were observed as inflexion points. As a preliminary approach, these inflexion points were traced as a potential instability lines IL=1.15 (C) as it may be seen in Figure 6.31.

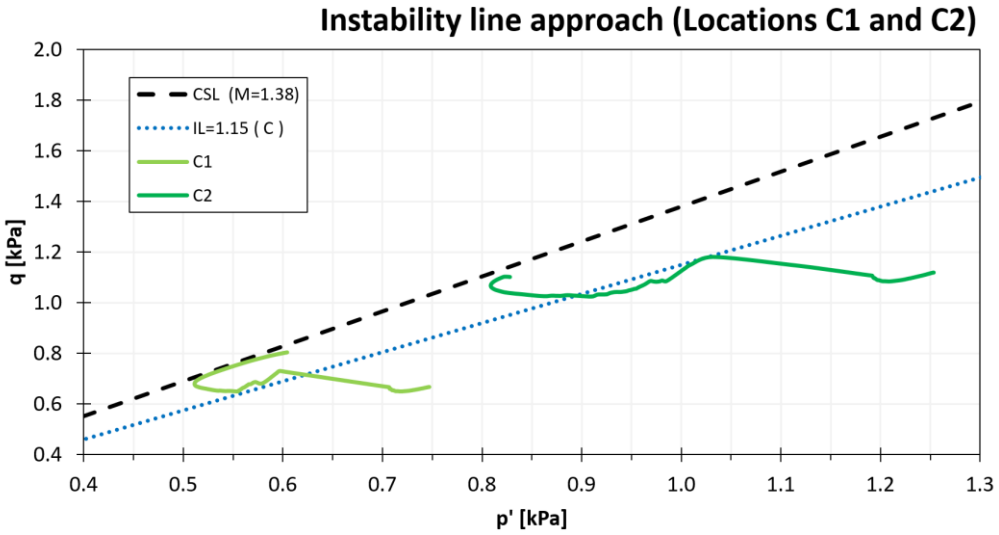

Figure 6.31- Preliminary adopted regions (IL) of the SL-tank model based on unusual behavior of stress points.

The instability line IL=1.15 was compared to the empirical approach IL=0.74, from which an average between these two IL was obtained as IL=0.95 (Figure 6.32). Figure 6.33 depicts the instability region at which a potential stress state could lead to liquefaction potential within the liquefaction tank test model.

As a summary of this approach: the adopted IL was based on experimental results from similar sands, CUTX simulations with a modified UBCS, and finally using output results from the FEM SL-tank HP model at locations C1 and C2.

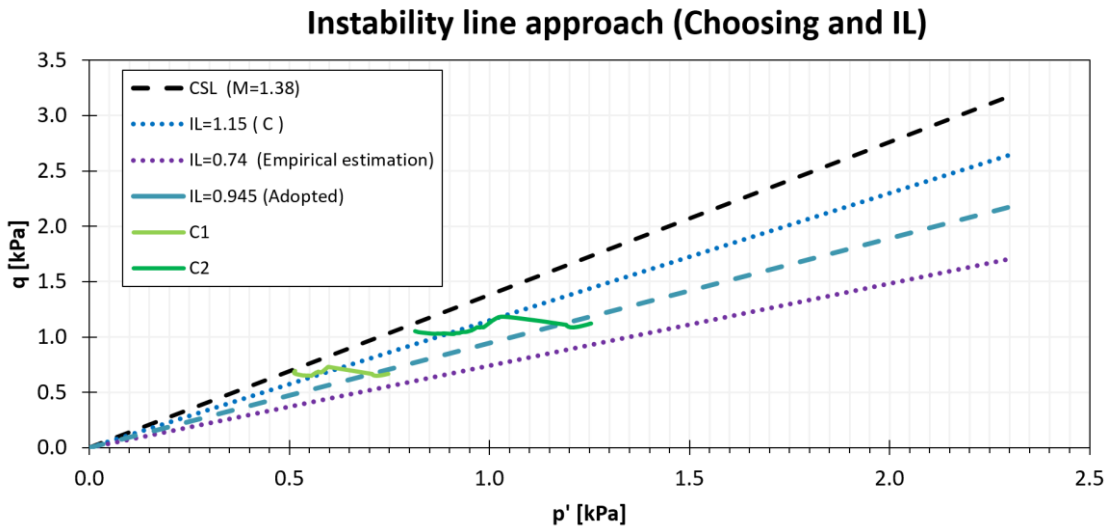

Figure 6.32- Selected IL for Geba sand SL-tank model.

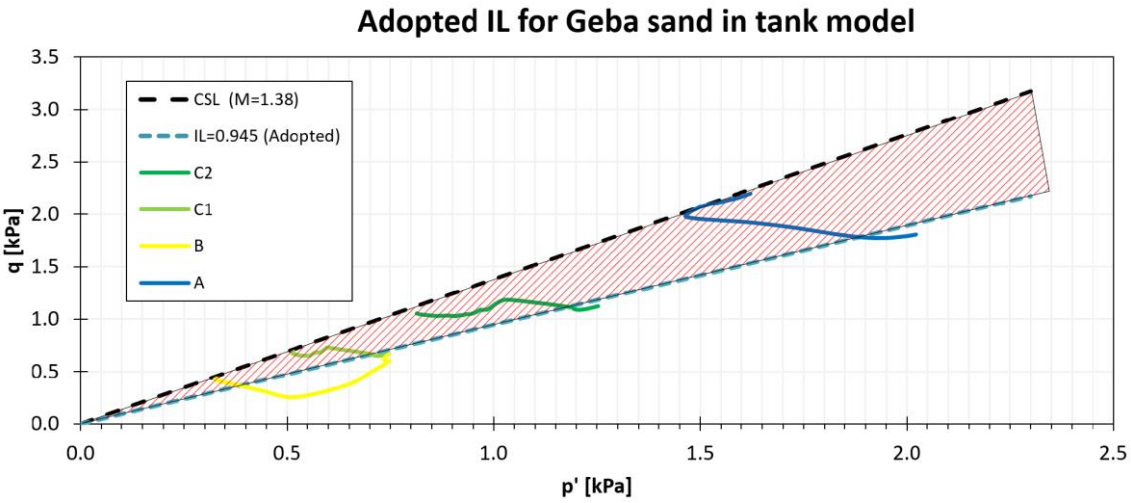

Figure 6.33- Shaded region of instability for the adopted IL in Geba sand SL-tank model.

Chapter 7: Conclusions and recommendations

In this final chapter, the conclusions of the research project are presented by being based on the stated research goals. The following sections draw the related conclusions for each of the four project objectives.

7.1 Experimental element tests at very low confining stresses

Regarding the Oedometer test:

A wet sample preparation for OED tests provide a more reproducible test setup for Geba sand at a target D_r=0.40 than a dry preparation. Unloading-Reloading stages are significantly difficult to perform at confining stresses lower than 50kPa. During the initial loading, a notorious load-sensitivity was the main challenge due to low stresses at a range of [1÷10]kPa. If any minimal additional force was applied during the initial loading, the recorded initial deformation would vary significantly.

The Unloading-Reloading stiffness E_{ur} of Geba sand may be related in terms of Oedometric stiffness E_{oed} by means of the expression $E_{ur} \approx [4 \div 5] \cdot E_{oed}$, which complies within empirical results of sands. The reported E_{oed} for Geba sand at the effective confining stresses of the SL-tank test [1÷4]kPa are at significantly low stiffness range ($E_{oed} <$ 1000 kPa). If compared to an Oedometric stiffness at P_{ref}= 100 kPa, the E_{oed} within this research scope is approximately 15 times smaller than at medium stresses.

Regarding the Direct Shear test:

For DS tests, achieving a consistent D_r was challenging due to the joints and cavities of the shear box mold. A significant margin of error for D_r was estimated as $\pm$0.10 from prepared samples at either loose or dense configuration. The shear strength at very low stresses of [1÷10]kPa obtained for Geba sand showed similar outcomes as the ones observed from previous tests on sands. Significantly large φ_p were obtained from medium-loose results (Dr≈0.40) , that could be reported as high as 1.4 times the φ_{cv} of Geba sand. Dilatancy angles were seen as high as 13° for medium-loose conditions. The use of empirical correlations for estimating the dilatancy angle of a sand yielded satisfactory results in comparison to the experimental results. As reported previously for tested loose sand at low stresses, a significant soil dilatancy is the most prominent shear strength behavior observed.

Regarding the Consolidated-Undrained tri-axial test.

The effect of confining stress had a more significant impact upon shear strength than the relative density from medium-loose CUTX tests. A highly non-linear behavior of shear strength as a function of confining stress was estimated for stresses lower than 25kPa. The results from CUTX on Geba sand confirmed that the empirical relationship $E_{oed} \approx E_{50}$ yielded satisfactory results.

7.2 Calibration of constitutive models

It was not necessary to significantly modify the experimentally calculated parameters of MC and HS models. The parameters from these two EP models are directly influenced by the obtained experimental results in this project, so they yielded satisfactory best-fits of curves.

The calibrated UBCS model was modified in terms of stiffness response to best-fit experimental curves, from which the empirical relationships based on D_r and SPT-number N_{60} did not provide sufficiently reliable results for parameter determination. This was the only tested model that showed the possibility to lower the shear strength response to such lengths as nearly observing liquefaction behavior in a modelled CUTX p'-q curve.

The HP model showed the most relevant result in terms of parameter calibration from all the tested models. The experimental results derived from tests at medium-high stresses yielded a set of parameters that were satisfactory for a confining stresses range of [1÷4000] kPa. The only parameter that was needed to calibrate was the φ_{cv} , since the HP formulation does not directly use dilatancy or peak angles as input parameters.

The calibration of the EP models and the HP model showed a proportional response for CUTX simulations if the confining stress was modified, but the ISHP model didn't show this trait. Highly dilatant behavior was noticed if the preliminary parameter set of ISHP was used at stresses lower than 50kPa. In the other hand, contractive behavior was obtained for CUTX simulations at stresses higher than 50kPa with the same preliminary parameter set. The calibrated ISHP parameters are significantly different than the preliminary ones but they provided reasonably better curve-fits.

CUTX simulations performed at similar confining stress conditions as the tank test, showed that the HP formulation significantly outperforms the other EP models in contractive behavior characteristics.

7.3 Comparisons between EP and HP model results

The modelled excess pore water pressure at the tank's sensor locations was noticeably larger for the HP framework than the EP models. The elasto plastic models simulated excess P_w at some areas of the SL-tank that were even negative (suction), whereas the HP model showed a smaller extent of such an erroneous model response. The ISHP model was not used as reference for comparison due to the numerical instability that did not allow a complete model simulation. The excess Pw generated at the triggering 7th phase of the SL-tank model was acting over a significantly larger area in the HP model than the EP simulations.

The sharp reduction of mean effective stress after triggering the induced failure of the SL-tank model was noticeable prominent for the HP outputs, while not for the EP models. The critical state was not reached for some locations of the tank when using EP models, whereas the HP model was able to reach this ultimate state at the same analyzed locations.

The North side of the tank, which is probably the critical zone of failure initiation, generated unsatisfactory modelled results from the EP models. MC, HS and UBCS exhibited a similar effective stress path response, which differs from what would be expected at failure (reaching the CSL). In terms of failure potential at the North side, the HP model provided a more reliable response. In the other hand, EP models failed to model a significant loss of effective mean stress during the induced failure applied to the SL-tank model.

As a final statement of this section, Hypoplasticity was not able simulate static liquefaction but nevertheless it generated significantly better results than the compared Elasto-Plastic models.

7.4 Numerical results comparison with experimental data

The main limitation that exhibited all the chosen constitutive models were the nearly negligible strains obtained, particularly deviator and vertical strains. Visual observations of vertical deformations from a SL-tank test showed significant strain levels reached at failure that did not manifest in the given simulations. Nevertheless, the tilted sand layer was deformed in a pattern similar to experimental observations but deformations in the model were drastically smaller than the experimental results.

The fixed boundary condition at the bottom of the modelled SL-tank did not allow horizontal displacements. The HP formulation was not able to generate deformations significant enough to reach failure conditions without an additional trigger mechanism. The induced-failure by allowing a normal fixity at the 7^{th} phase of the model was the main factor for allowing a model failure through sudden excess P_w generation.

The abrupt generation of excess pore water pressure was not distributed over the entire area of the modelled SL-tank, but instead only a significant portion of the Northern side experienced this sudden jump of excess P_w. The magnitude of the modelled excess P_w at the North side was comparable to the experimental results.

The use of the porous layer beneath the Geba sand layer merely served as a means to dissipate the excess P_w generated by a mechanical process (change in void ratio) but not by taking into account groundwater flow. The inability to adopt water flow within the model is one of its main limitations. It must be considered that the modelled porous layer was stressed and deformed, as well as being subjected to the direct action of the boundary fixity change in phase 7. Limitations of the current software interface did not allow to exclude the porous material from being affected by the boundary fixity and stress-strain effects over the modelled granular material for this porous layer.

The model response emphasizes a more prone behavior to failure at the Northern location, than the Southern side of the tank, which may be related to the experimental observations of the SL-tank test. The principal stress directions of the model demonstrate that the Northern side is acting as a the toe of a failing slope during the triggered induced-failure at the final modelled phase.

7.5 Adopted instability line approach

No clearly defined peak deviator stresses could be observed from the modelled SL-tank response with the HP formulation. Nevertheless, an attempt using empirical and numerical data was performed. The obtained instability line for the modelled SL-tank is merely a rough estimation of the instability region of Geba sand within the experimental SL-tank test conditions. No clear estimation of IL was possible with the available numerical simulations of the SL-tank model.

7.6 Recommendations for further research

- For further numerical simulations with the Hypoplasticity framework, an enhancement in the model boundary conditions may provide better results. Alternatives such as correctly adopting interface elements between the modelled soil and porous layer may be used. More likely, a different modelling approach without the constraints of a commercial code such as PLAXIS will be necessary to adjust the boundary conditions to more realistic conditions. A different constitutive framework or an enhanced version of the Hypoplasticity model should as well be tested within similar conditions as the ones adopted for these numerical simulations.
- The effect of groundwater flow through the soil layer and the highly porous layer of the SL-tank should be taken into consideration for further numerical studies. This process should be analyzed by means of a transient flow analysis with a flow-deformation fully coupled process, which was unavailable for this project due to technical issues within the software PLAXIS.
- The bottom face of the SL-tank test should be studied into more detail to obtain more accurate results when modelling this boundary condition. Having assumed a fully rigid interface at the lower boundary of the SL-tank may have hindered the possibility to observe significant strains during the simulations.
- A shallow soil layer of 0.5m was tested both experimentally and numerically for this research scope. With the current SL-tank model, increasing the height of the slope did not generate more favorable results. An experimental dredged and tilted slope may be tested and observe any further details of the failure mechanism by numerically simulating it with the available SL-tank model.
- Excess pore water pressures were the main and only available experimental data to compare with the SL-tank simulations, which hindered more potential model verifications. A significant enhancement to the available data would be to implement load cells to measure shear and normal stresses at several tank locations.

References

Anaraki, K.E. (2008) *Hypoplasticity Investigated Parameter Determination and Numerical Simulation*. Master thesis. Delft University of Technology, The Netherlands.

Azua, C. (2017) Hypoplasticity parameter determination with Geba sand. Internal report. Delft University of Technology, The Netherlands.

Been, K. & Jefferies, M.G. (1985) A state parameter for sands. *Géotechnique 35, No.2*. 99–112.

Been, K., Jefferies, M.G., Hachey, J. & Chu, J. (1992) The critical state of sands: discussion. *Géotechnique, 42* (4).

Bolton, M.D. (1986) The strength and dilatancy of sands. *Géotechnique*. 36 (1), 65–78.

Brinkgreve, R.B.J., Engin, E. & Engin, H.K. (2010) Validation of empirical formulas to derive model parameters for sands. *Numerical Methods in Geotechnical Engineering*, 137–142.

Castro, G. (1969) Liquefaction of sands. ph. D. thesis. *Harvard Soil Mech*.

Charles, W.W. (2009) *What is Static Liquefaction Failure of Loose Fill Slopes ? The 1st Italian Workshop on Landslides.*

Chu, J., Leroueil, S. & Leong, W.K. (2003) Unstable behaviour of sand and its implication for slope instability. *Canadian Geotechnical Journal*. 40 (1984), 873–885.

Dafalias, Y.F. (1986) Bounding surface plasticity. I: Mathematical foundation and hypoplasticity. *Journal of Engineering Mechanics*. 112 (9), 966–987.

Davies, M., McRoberts, E. & Martin, T. (2002) Static liquefaction of tailings–fundamentals and case histories. *AMEC Earth and Environmental*. 23.

Eckersley, J.D. (1990) Instrumented laboratory flowslides. *Géotechnique*. 40 (3), 489–502.

Fannin, R.J., Eliadorani, A. & Wilkinson, J. (2005) Shear strength of cohesionless soils at low stress´. *Geotechnique*. (6), 467–478.

Ferreria, T. & Rasband, W. (2012) *ImageJ user guide*. 2012. https://imagej.nih.gov/ij/docs/guide/146.html.

Gay, O., Boutonnier, L., Flavigny, E. & Foray, P. (2003) Laboratory characterization of Hostun RF sand at very low confining stresses. *Deformation Characteristics of Geomaterials / Comportement Des Sols Et Des Roches Tendres*.

Herle, I. & Gudehus, G. (1999) Determination of parameters of a hypoplastic constitutive model from properties of grain assemblies. *Mechanics of Cohesive-frictional Materials*. 4 (5), 461–486.

Hicks, M.A. & Wong, S.W. (1988) Static liquefaction of loose slopes. *Numerical Methods in Geomechanics*. 1361–1367.

Jacobs, R. (1998) *Aerial Oosterscheldekering ID179670*. 1998. https://beeldbank.rws.nl/MediaObject/Details/179670.

de Jager, R. (2015) *Determination of global sand density in liquefaction tank*. Technical report. Delft University of Technology, The Netherlands.

de Jager, R. (2006) *The behavior of soilds during static liquefaction in Geotechnical engineering*. Master thesis. Delft University of Technology, The Netherlands.

Jaky, J. (1944) The coefficient of earth pressure at rest. *Journal of the Society of Hungarian Architects and Engineers*. 78 (22), 355–358.

Kolymbas, D. (1991) An outline of hypoplasticity. *Archive of Applied Mechanics*. 61 (3), 143–151.

Kramer, S.L. (1988) Triggering of liquefation flow slides in coastal soil deposits. *Engineering Geology*. 2617–31.

Krapfenbauer, C. (2016) *Experimental Investigation of Static Liquefaction in Submarine Slopes*. Master Thesis. Swiss Federal Insititute of Technology in Zurich, Switzerland.

Lade, P. V. & Yamamuro, J.A. (2011) Evaluation of Static Liquefaction Potential of Silty Sand Slopes. *Canadian Geotechnical Journal*. 48 (2), 247–264.

Lade, P.V. (1993) Initiation of static instability in the submarine Nerlerk berm. *Canadian Geotechnical Journal*. 895–904.

Lade, P.V. & Pradel, D. (1990) Instability and plastic flow of soils. I: Experimental observations. *Journal of Engineering Mechanics, ASCE, 116(11)*. 2532–2550.

Makra, A. (2013) *Evaluation of the UBC3D-PLM constitutive model for a prediction of earthquake induced liquefaction of embankment dams*. Master thesis. Delft University of Technology, The Netherlands.

Masin, D. (2017) *Report on the triaxial tests on GEBA sand carried out for client : IHC IQIP, NL*. Technical report.

Mukhtar, H. (n.d.) *Geotechnical parameter documentation*. https://dnr.mo.gov/env/hwp/docs/geotech parameter.pdf

Muscolino, S. (2015) *Infinite slopes software*. 2015. http://www.infiniteslopes.net/the-model.html.

Niemunis, A. (2002) *Extended hypoplastic models for soils*. Postdoctoral research habilitation. Karlsruhe Institute of Technology, Germany.

Noriega, S.P. (2015) *Characterisation of Saturated Loose Sand Samples prepared by Fluidization*. Master thesis. Delft University of Technology, The Netherlands.

van de Oever (2013) *The instrumentation and control of experiments in liquefaction tank*.Technical report. Delft, University of Technology, The Netherlands.

Petalas, A. & Galavi, V. (2013) *PLAXIS LIQUEFACTION MODEL UBC3D-PLM*. Technical report. PLAXIS BV, The Netherlands.

PLAXIS (2016) *2D-3-Material-Models*. Technical report. PLAXIS BV, The Netherlands.

Ponce, M. & Bell, J. (1971) Shear strength of sand at extremely low pressures. *Soil Mechanics and Foundations Division*.

Roscoe, K.H., Scho eld, M.A. & Wroth, C.P. (1958) On the yielding of soils. *Géotechnique 8*. 22–52.

Rowe, P.W. (1962) The Stress-Dilatancy Relation for Static Equilibrium of an Assembly of Particles in Contact. *Proceedings of the Royal Society of London. Series A. Mathematical and Physical Sciences*. 269 (1339), 500 LP-527. http://rspa.royalsocietypublishing.org/content/269/1339/500.abstract.

Schanz, T., Vermeer, a & Bonnier, P. (1999) The hardening soil model: formulation and verification. *Beyond 2000 Comput. Geotech. 10 years PLAXIS Int. Proc. Int. Symp. beyond 2000 Comput. Geotech. Amsterdam Netherlands 1820 March 1999*. 281.

Schanz, T. & Vermeer, P.A. (1998) On the Stiffness of Sands. *Pre-failure deformation behaviour of geomaterials*. 383–387.

Sfriso, A.O. (2009) The friction angle and critical state void ratio of sands. *Proceedings of the 17th International Conference on Soil Mechanics and Geotechnical Engineering: The Academia and Practice of Geotechnical Engineering*. 1 (3), 433–435.

Sibelco Europe (2014) *Technical data of Geba sand*. 2014. http://www.eurogrit.nl/prod/prod33_Datasheet Geba (UK).pdf.

Silvis, F. & Groot, M.B. De (1995) *Flow slides in the Netherlands: experience and engineering practice*. Canadian geotechnical journal, 32 (6), 1086-1092.

Sladen, J.A., Hollander, R.D. & Krahn, J. (1985) "The liquefaction of sands, a collapse surface approach. *Canadian Geotechnical Journal 22,*. 564–578.

Sture, S., Costes, N., Batiste, S., Lankton, M., et al. (1998) Mechanics of granular materials at low effective stresses. *Journal of Aerospace Engineering*. 11 (3), 67–72.

Ti, K.S., Gue See, S., Huat, B.B.., Noorzaei, J., et al. (2009) A Review of Basic Soil Constitutive Models for Geotechnical Application. *Electronic Journal of Geotechnical Engineering*. 1418.

Tjie, L. (2014) Common Mistakes on the Application of Plaxis 2D in Analyzing Excavation Problems. *International Journal of Applied Engineering Research*. 98291–8311.

Tsegaye, A.B. (2009) *Evaluation of Material models for Liquefaction*. Master thesis. Delft University of Technology, The Netherlands.

Urciuoli, G. (2001) Strains preceding failure in infinite slopes. *International Journal of Geomechanics*. 1 (1), 1–20.

Vermeer, P.A. & de Borst, R. (1984) Non-Associated Plasticity for Soils, Concrete and Rock. *Heron*. 29 (3).

Watson, I. & Jr., C.W.F. (1990) State of the Art in Storm-Surge Protection: The Netherlands Delta Project. *Journal of Coastal Research*. 6 (3), 739–764.

von Wolffersdorff, P.A. (1996) Hypoplastic relation for granular materials with a predefined limit state surface. *Mechanics of Cohesive-Frictional Materials*. 1(3), 251–271.

Appendix

Appendix A: Estimation of D_r in SL-tank test

Height measurement of tapes E1÷E6 and W1÷W6 for Dr determination								
Tape tag	Gross H [cm]	C. [m]	Height [m]	Vc [m3]	V [m3]	P [kg/m3]	*e* liq	Dr (%)
E1	48.5	2	0.47	4.38	4.61	1428	0.87	**47**
E2	54.5	1.5	0.53	4.99	5.22	1261	1.12	**-11**
E3	50	1.4	0.49	4.58	4.81	1369	0.95	**28**
E4	48.5	1.9	0.47	4.39	4.62	1425	0.87	**46**
E5	48.75	1.7	0.47	4.43	4.66	1412	0.89	**42**
E6	49	0.8	0.48	4.54	4.77	1380	0.93	**32**
W1	49.75	0.3	0.49	4.66	4.89	1347	0.98	**20**
W2	54.5	0	0.55	5.14	5.36	1227	1.18	**-25**
W3	48	0	0.48	4.52	4.75	1386	0.93	**33**
W4	47.5	0.1	0.47	4.47	4.69	1402	0.90	**39**
W5	47.5	0	0.48	4.48	4.70	1400	0.91	**38**
W6	48	0	0.48	4.52	4.75	1386	0.93	**33**

Fixed data for D_r estimation	
P_s [kg/m^3]	2670
A_{liq} [m^2]	9.424
V_g [m^3]	0.225
Mass [kg]	6580

Average Dr	30%

Gross H: measured height from tapes.

C: correction factor of height.

Height: corrected global sand layer depth.

V_g : volume of the sand filling the open spaces of the bottom grid from the tank.

V_c: global sand volume without considering V_g.

P_s: density of Geba sand grains.

A_{liq}: main area of the liquefaction tank inner dimensions.

Mass: total mass of the considered sand inside the tank.

V: global volume of the sand layer.

P: density state of sand at initial testing conditions.

***e* liq**: initial void ratio at testing conditions.

***Note**.- See report from de Jager (2015) for a detailed description of the involved variables and overall procedure for D_r estimation.*

Appendix B: Sensitivity of ISHP parameters

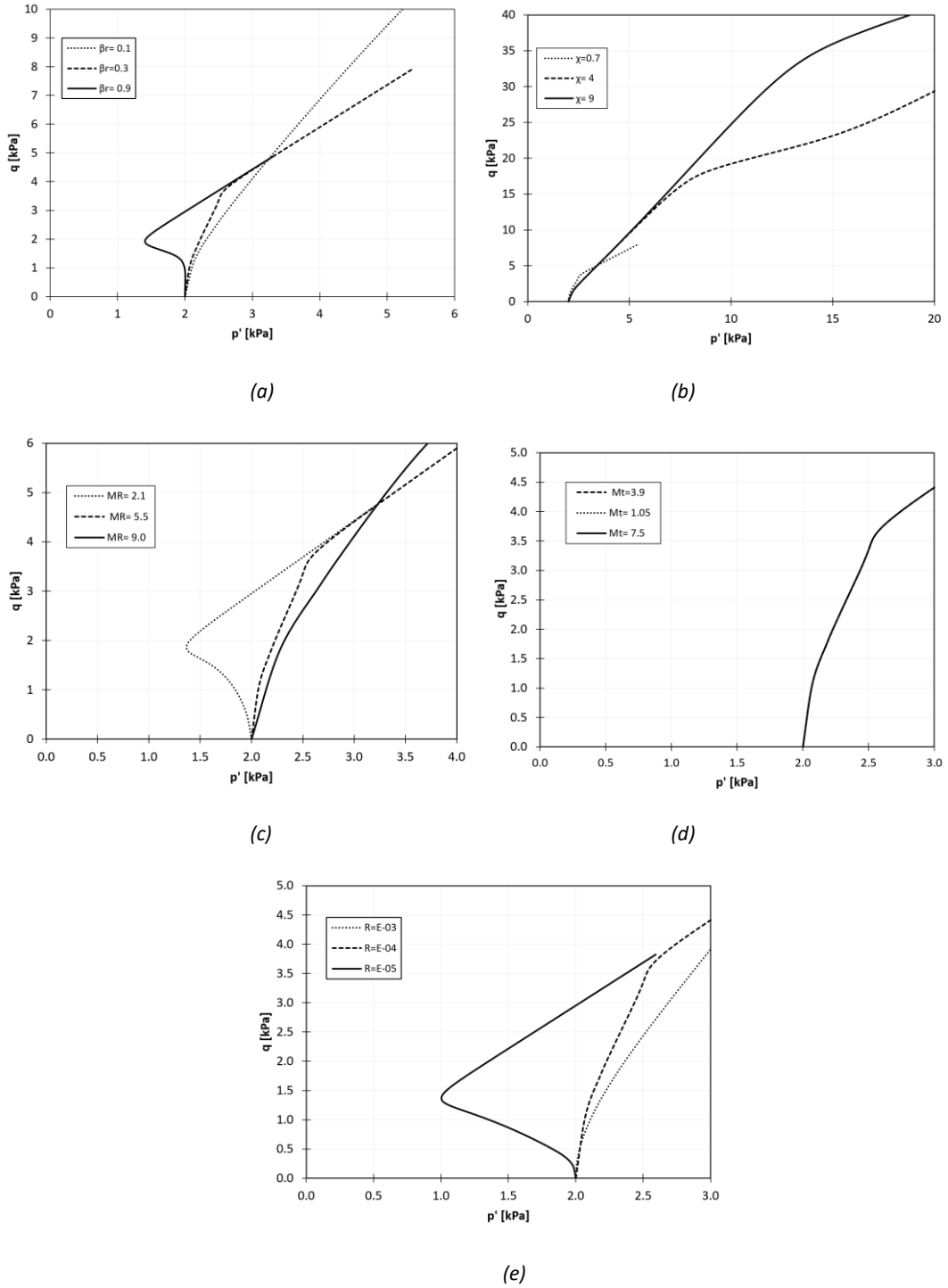

Figure B1.- Sensitivity of the 5 input parameters of the ISHP model, from CUTX simulations.

***Note**- The sensitivity curves of parameter M_t from Figure B1**(b)** are overlapped, i.e. no sensitivity was obtained from M_t.*

Appendix C: Deformation outputs of SL-tank model (HP)

Figure C1- Total vertical strains ε_y (- is extension) at phase 6.

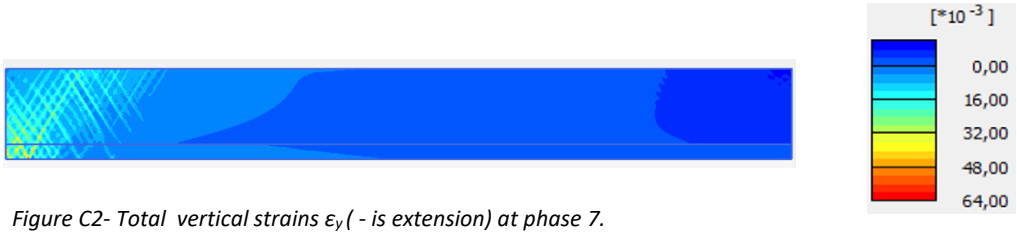

Figure C2- Total vertical strains ε_y (- is extension) at phase 7.

Figure C3- Total vertical strains ε_Y (- is extension) at phase 9.

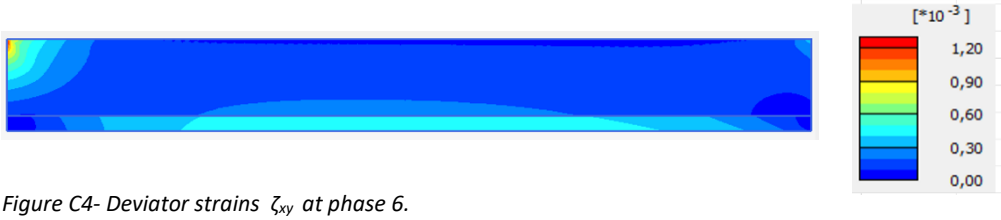

Figure C4- Deviator strains ζ_{xy} at phase 6.

Figure C5- Deviator strains ζ_{xy}) at phase 7.

Figure C6- Deviator strains ζ_{xy} at phase 9.

Appendix D: Sensitivity of void ratio from SL-tank model (HP)

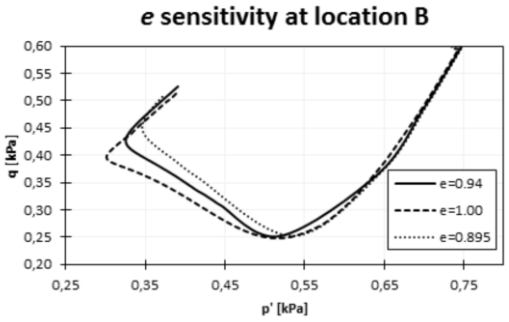

Figure D1- Sensitivity of void ratio at location B (HP model).

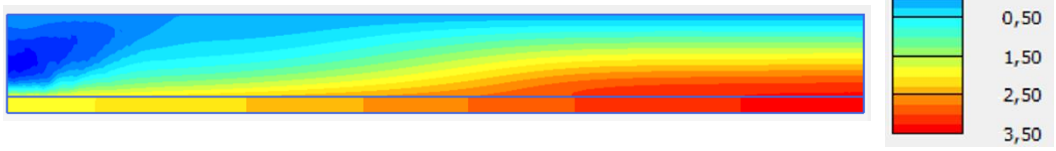

*Figure D2- Excess P_w (- is suction) at phase 7 with a D_r=0.40 (**e**=0.895).*

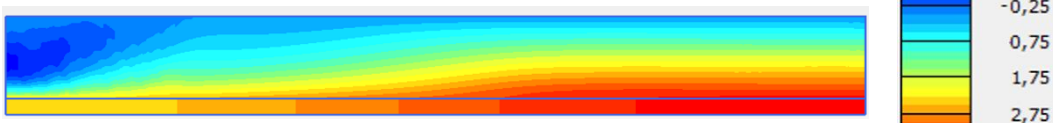

*Figure D3- Excess P_w (- is suction) at phase 7 with a D_r=0.30 (**e**=0.94).*

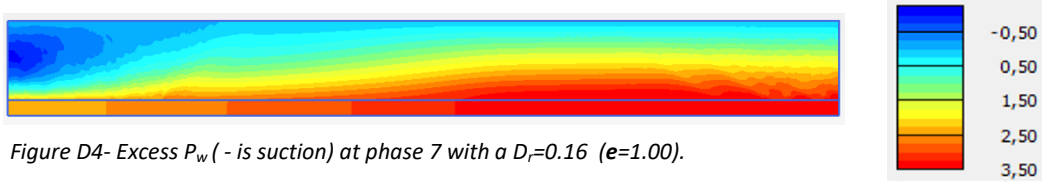

*Figure D4- Excess P_w (- is suction) at phase 7 with a D_r=0.16 (**e**=1.00).*

Appendix E: A simplified model representation (Analytical approach)

The failure mechanism observed at natural submerged slopes is complex and currently no numerical approach is able to accurately model it. Even physical models such as the liquefaction SL-tank, exhibit limitations that hinder accurate simulations of real soil behavior. Many rudimentary approaches, usually analytical, are used as a first insight for a particular case study.

Regarding slope failures, the most simple approach to analyze slope instability is through limit-equilibrium solutions. These analytical solutions are usually displayed in terms of factors of safety (FoS) by weighting resistant forces against driving forces. For a plane strain simplification of the Static liquefaction tank, an infinite slope analysis may serve as a first illustrative approach of this soil behavior.

An infinite slope analysis may quantify a FoS for a submerged slope by taken into consideration properties such as inclination angle δ, depth of layer H, soil unit weight Υ_{sat}. MC parameters of φ_p and **c** are used as well.

Pseudo-static accelerations α_v and α_h could be implemented in this models and they were used as a way to impose an instantaneous tilting effect of 1 degree. The modelled slope in this analytical model is taken initially as 9°, from which pseudo-static accelerations are used to generate a tilting condition to reach 10°.

This method was implemented for analyzing the Static liquefaction tank through an interactive software of infinite slope analysis named ''Infinite Slope v. 3.0'' (Muscolino, 2015). The results are expressed in terms of FoS.

The following set model conditions were used for this simple solution:

Table 6.1 Input values for software Infinite slope V. 3.0.

Infinite slope input parameters/conditions		
friction angle [°]	φ_p	47; 40; 34
Cohesion [kPa]	p_t	0
Slope inclination [°]	δ	9
Slope depth [m]	H	0.5
Saturated unit weight [kN/m3]	Υ_{sat}	18
Horizontal pseudo-acceleration [-]	α_v	0.174
Vertical pseudo-acceleration [-]	α_h	0.015

The Factor of safety was obtained for three cases, in which the only change was the peak friction angle.

Table 6.2 Output results from software Infinite slope V. 3.0.

φ_p [°]	47	40	34
FoS [-]	1.34	1.05	0.84

The results from this limit equilibrium approach were based in assuming a slope of 9 degrees , which suddenly perceived pseudo accelerations that are an equivalent to a tilting angle of 10 degrees. The imposing α_v and α_h values simulate a tilting mechanism from 9 to 10, in which this simulation is time-independent. A parallel water flow was adopted for this simple model, although a parallel diverges significantly from the real groundwater flow behavior perceived at a case such as the SL-tank.

The FoS was reported as ''safe'' for φ_p =47° but not by a sufficient margin of safety. By using φ_{cv}=34, the safety of the slope is already compromised and significantly lower than 1, meaning failure. Even for φ_p =40°, the safety of the slope is already affected. Nevertheless, this analytical solution is a mere simplification with several drawbacks, such as being based on MC, assuming parallel ground flow to the slope face or a non-planar failure mechanism.

A final comment from these results is that the intervention of high mobilized friction angles is a crucial factor for allowing quasi-stable conditions for such low inclination slopes at very low field stress conditions.

Appendix F: Deformation outputs of SL-tank model (1m layer) (HP)

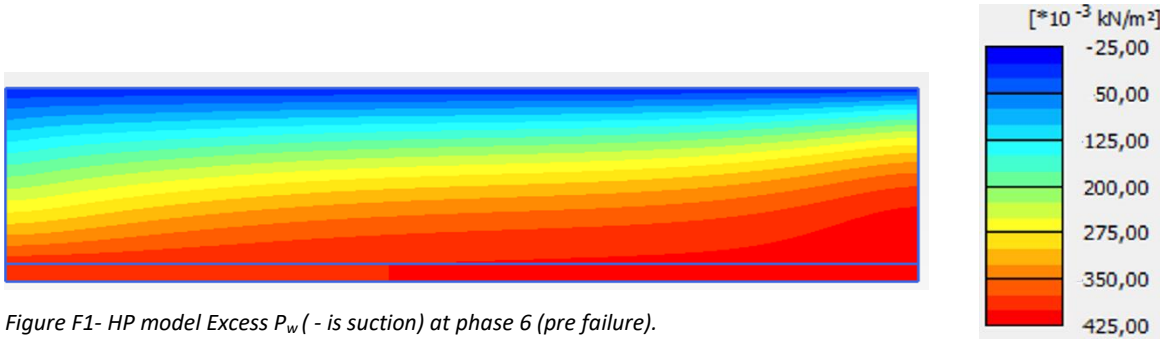

Figure F1- HP model Excess P_w (- is suction) at phase 6 (pre failure).

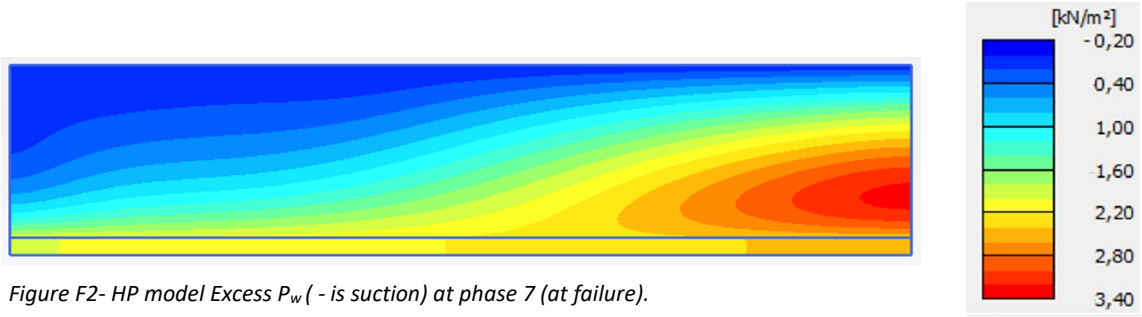

Figure F2- HP model Excess P_w (- is suction) at phase 7 (at failure).

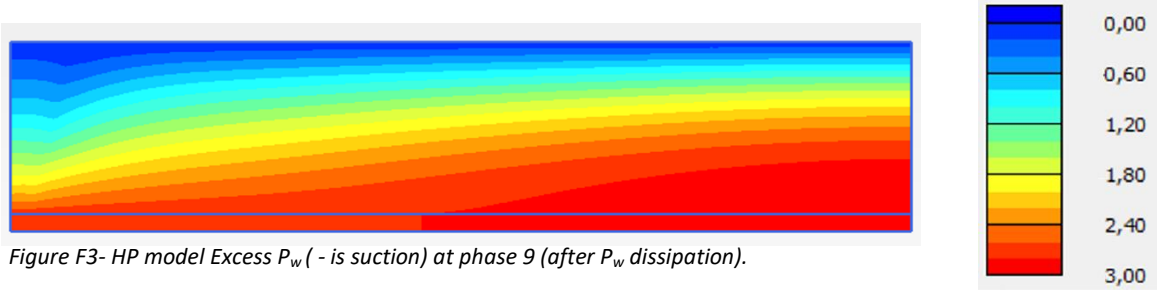

Figure F3- HP model Excess P_w (- is suction) at phase 9 (after P_w dissipation).

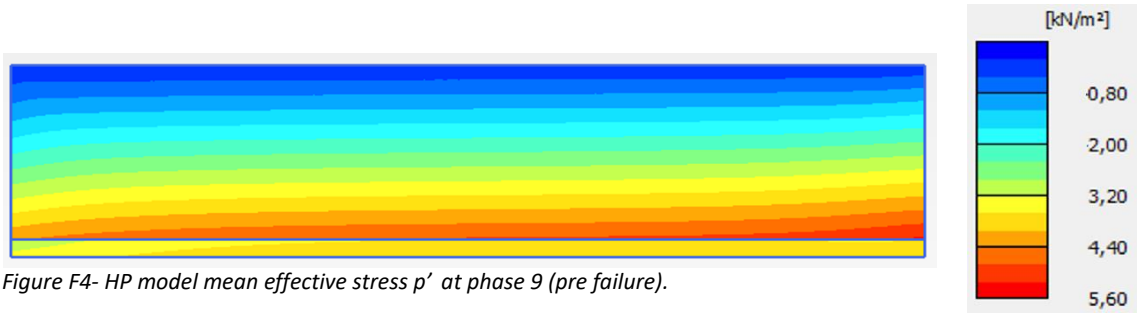

Figure F4- HP model mean effective stress p' at phase 9 (pre failure).

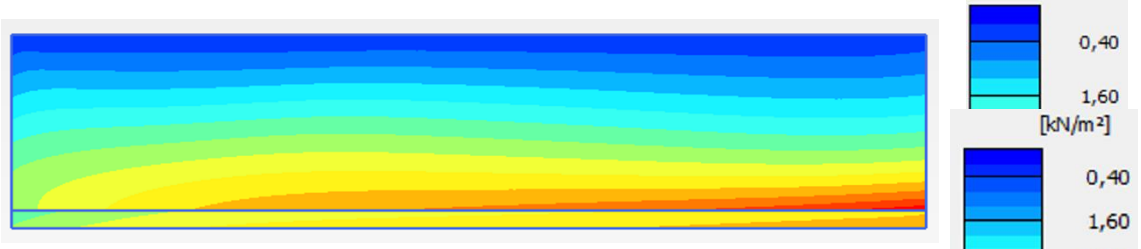

Figure F5- HP model mean effective stress p' at phase 9 (at failure).

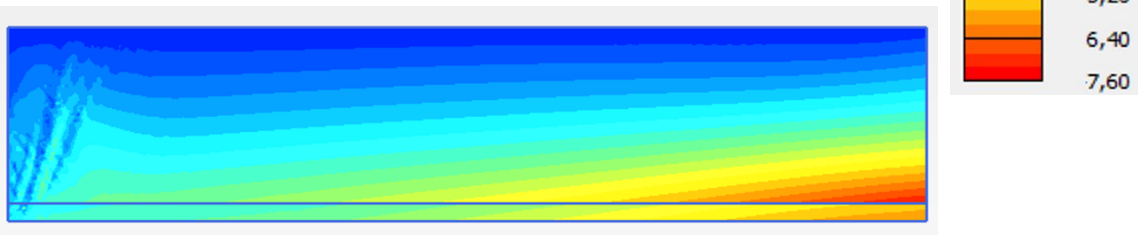

Figure F6- HP model mean effective stress p' at phase 9 (after P_w dissipation).